REGULATION OF CLATHRIN MEDIATED ENDOCYTOSIS AND ITS ROLE IN CANCER PROGRESSION

APPROVED BY SUPERVISORY COMMITTEE

Sandra Schmid, Ph.D., Advisor

John Minna, M.D., Chairman

Jerry Shay, Ph.D.

Gaudenz Danuser, Ph.D

DEDICATION

I would like to thank my husband, Mac, my parents, and my family for their love and support, which has allowed me to reach this milestone in my life. I would also like to thank my mentor and the members of my Graduate Committee for thoughtful discussion and helping me reach my true potential.

REGULATION OF CLATHRIN MEDIATED ENDOCYTOSIS AND ITS ROLE IN CANCER PROGRESSION

by

SARAH ELKIN CONNELLY

DISSERTATION

Presented to the Faculty of the Graduate School of Biomedical Sciences

The University of Texas Southwestern Medical Center at Dallas

In Partial Fulfillment of the Requirements

For the Degree of

DOCTOR OF PHILOSOPHY

The University of Texas Southwestern Medical Center at Dallas

Dallas, Texas

August 2017

REGULATION OF CLATHRIN MEDIATED ENDOCYTOSIS AND ITS ROLE IN CANCER PRGRESSION

Publication No. _____

Sarah Elkin Connelly, Ph.D

The University of Texas Southwestern Medical Center at Dallas, 2017

Supervising Professor: Sandra Schmid, Ph.D.

Metastasis is a multistep process requiring cancer cell signaling, invasion, migration, survival, and proliferation. These processes require dynamic modulation of cell surface proteins by endocytosis. Given this functional connection, it has been suggested that endocytosis is dysregulated in cancer. To test this, we developed In-Cell ELISA assays to measure three different endocytic pathways: clathrin-mediated endocytosis, caveolae-mediated endocytosis, and clathrin-independent endocytosis and compared these activities in 29 independently isolated non–small cell lung cancer (NSCLC) cell lines to determine whether there were systematic changes in the three different endocytic pathways. However

we observed significant heterogeneity. Nonetheless, using hierarchical clustering based on their combined endocytic properties we identified two phenotypically distinct clusters of NSCLCs. One co-clustered with mutations in KRAS, a mesenchymal phenotype, increased invasion through collagen and decreased growth in soft agar, whereas the second was enriched in cells with an epithelial phenotype.

We also used the In-Cell ELISA assay to characterize Ikarugamycin (IKA), a previously discovered antibiotic, which inhibits the uptake of oxidized low-density lipoproteins in macrophages, as well as clathrin-mediated endocytosis (CME) in plant cell lines. However, detailed characterization of IKA had yet been performed. Therefore, we performed biochemistry and microscopy experiments to further characterize the effects of IKA on CME. We showed that IKA acutely inhibits CME, but not other endocytic pathways with an IC50 of 2.7 μM. Although long-term incubation with IKA has cytotoxic effects, the short-term inhibitory effects on CME were reversible. Thus, IKA can be a useful tool for probing routes of endocytic trafficking.

Finally, we investigated possible mechanisms that lead to altered endocytosis in cancer cells. We discovered that dynamin 1 (Dyn1), previously thought to be neuron specific is frequently upregulated and postranslationally regulated in cancer cells. Dyn1 expression alters the proliferation rates, growth in soft agar, and tumor growth of cancer cells. We hypothesize that these changes are due to alteration in cell surface protein expression and downstream signaling pathways and have developed protocols to test these hypothesizes. Taken together, our results suggest that endocytic alterations in cancer cells can significantly influence cancer-relevant phenotypes.

TABLE OF CONTENTS

PRIOR PUBLICATIONS

Elkin SR, Kumar A, Price CW, Columbus L. *A broad specificity nucleoside kinase from Thermoplasma acidphilum.* Proteins. 2013; 81(4):568-82.

LIST OF FIGURES

CHAPTER ONE

CHAPTER TWO

CHAPTER THREE

LIST OF TABLES

CHAPTER THREE

CHAPTER FOUR

LIST OF ABBREVIATIONS

AP2 – adaptor protein 2

APPL1 – adaptor protein, phosphotyrosine interacting with PH domain and leucine zipper 1

Cav-1 – Caveolin-1

CavME – Caveolae-mediated endocytosis

CCP – Clathrin coated pit

CCV – clathrin coated vesicles

CHC – clathrin heavy chain

CIE – clathrin-independent endocytic

CLC – clathrin light chain

CLICs – clathrin-independent carriers

CME – clathrin-mediated endocytosis

Dyn – dynamin

EEA1 – early endosome antigen 1

EGFP – enhanced green fluorescent protein

EGFR – epidermal growth factor receptor

GEECs – GPI-AP enriched early endosomal compartments

GPCRs – G-protein coupled receptors

IKA – Ikarugamycin

LDL – low-density lipoprotein

LDLR – low-density lipoprotein receptor

NSCLC – non-small cell lung cancer

PM – plasma membrane

PRD – proline-rich domain

RPPA – Reverse Phase Protein Array

RTKs – receptor tyrosine kinases

SH3 – SH3SRC homology 3

SILAC – stable isotope labeling with amino acids in cell culture

Tfn – transferrin

TfnR – transferrin receptor

TIRF – Total internal reflection fluorescence

CHAPTER ONE
An Overview of Endocytic Pathways and their possible Role in Cancer Progression

ADAPTED FROM ELKIN, S. R., A. M. LAKODUK AND S. L. SCHMID (2016). "ENDOCYTIC PATHWAYS AND ENDOSOMAL TRAFFICKING: A PRIMER." WIEN MED WOCHENSCHR 166(7-8): 196-204.

Introduction

Endocytosis, the process by which cells internalize macromolecules and surface proteins, was first observed with the advancement of electron microscopy, allowing for the visualization of the specialized membrane domains responsible for two mechanistically and morphologically distinct pathways: clathrin-mediated endocytosis (CME) [1] and caveolae uptake [2]. Selective inhibition of these two pathways later led to the discovery of cholesterol-sensitive clathrin- and caveolae-independent pathways [3-5], and more recently, the large capacity CLIC/GEEC pathway [6].

After molecules have been internalized through one of these different endocytic pathways they traffic through and are sorted by a pleomorphic series of tubulovesicular compartments, collectively called endosomes [7]. Internalized macromolecules and surface proteins can have many different fates. They can be recycled back to the plasma membrane, delivered to the lysosomes for degradation, or sent across polarized cells through a process called transcytosis, which is important for transport across epithelia, endothelia and the blood brain barrier [8]. Endosomal compartments undergo maturation from early to late endosomes, which involves decreasing lumenal pH, altering key phosphatidylinositol lipids

through regulation by lipid kinases and phosphatases, and differential recruitment and activation of Rab-family GTPases.

Following the initial discovery of these pathways and their trafficking, it was then determined that each endocytic pathway fulfills multiple critical cellular functions. Cells communicate with each other and their environment through endocytosis. Consequently, endocytosis regulates the levels of many essential surface proteins and transporters in human health and disease, such as glucose transporters that maintain serum glucose levels, proton pumps that control stomach acidification, or sodium channels that control cell homeostasis [9]. Furthermore, endocytosis regulates signaling from surface receptors like G-protein coupled receptors (GPCRs) [10] and receptor tyrosine kinases (RTKs) [11]. Finally, endocytosis regulates cell-cell and cell-matrix interactions through uptake of integrins and adhesion molecules [12]. Since the discovery of endocytosis several decades ago, its complex and critical role in human physiology and pathology has become increasingly appreciated and better understood. This chapter briefly summarizes our current state of knowledge about cargo sorting and trafficking along the endocytic pathway.

Multiple Mechanisms for Uptake into Cells

Clathrin Mediated Endocytosis:

The most studied and hence, well-characterized endocytic mechanism is clathrin-mediated endocytosis (Figure 1), which occurs through coated pits and coated vesicles, first observed >50 years ago by thin section electron microscopy. CME was first found to play an

important role in low-density lipoprotein (LDL) [13] and transferrin (Tfn) uptake [14] upon binding to their respective receptors (hereafter referred to as 'cargo'). The principle components of the coated vesicles are the heavy and light chains of clathrin [15], from which the pathway acquires its name, and the four subunits of the heterotetrameric adaptor protein 2 (AP2) complex [16]. The AP2 complex links the clathrin coat to the membrane bilayer and is also the principle cargo-recognition molecule [17]. There are other specialized adaptor proteins, such as ARH, Dab2, CALM, and Numb [18], which each recognize distinct sorting motifs on their respective cargo receptors. These cargo-specific adaptor proteins often interact with both clathrin and the AP2 complex, increasing the repertoire of cargo that can be sorted.

Clathrin-coated vesicle formation proceeds through multiple stages: initiation, cargo-selection, growth and maturation, scission, and uncoating. Clathrin coated pit (CCP) assembly is initiated by AP2 complexes that are recruited to the plasma membrane-enriched phosphatidylinositiol (PI) phospholipid, $PI(4,5)P_2$ [19-21]. AP2 complexes then rapidly recruit clathrin (26). Other scaffolding molecules such as FCHo proteins, eps15, and/or intersectins also assemble early and may play a role in either nucleating CCPs and/or stabilizing nascent CCPs [22, 23]. Although clathrin has been shown to spontaneously assemble into closed cages *in vitro* [24], in cells, other curvature generating proteins must be recruited to nascent CCP's for efficient budding. Thus, the intrinsically curved, BAR (Bin-Amphiphysin-Rvs) domain-containing proteins can create increasingly deeper curvature and are thought to be required for progression of the clathrin-coated pit [25]. As the nascent CCPs grow, AP2 and other cargo-specific adaptor proteins recruit and concentrate cargo.

Polymerization of clathrin results in the stabilization of curvature of the pit; however other factors recruited to AP2 complexes are also required for efficient curvature generation and subsequent invagination of CCPs [26]. Budding of clathrin-coated vesicles from the plasma membrane depends on the large GTPase dynamin [27]. Dynamin is recruited to clathrin-coated pits by BAR domain-containing proteins [28] such as amphiphysin, endophilin, and sorting nexin 9 (SNX9), which also encode SRC homology 3 (SH3) domains that bind to dynamin's proline-rich domain (PRD). Dynamin assembles into collar-like structures encircling the necks of deeply invaginated pits and undergoes GTP hydrolysis to drive membrane fission [27]. Finally, once the vesicle is detached from the plasma membrane the clathrin coat is disassembled by the ATPase, heat shock cognate 70 (HSC70) and its cofactor auxilin [29, 30]. This allows the now uncoated vesicle to travel and fuse with its target endosome.

Caveolae Mediated endocytosis:

Caveolae-mediated endocytosis (CavME), which was also first discovered ~60 years ago by thin section electron microscopy, is the second most well-characterized and studied endocytic pathway (Figure 1). CavME has been found to be important in transcytic trafficking across endothelia as well as mechanosensing and lipid regulation [31]. Caveolae, the site of CavME, are flask or omega-shaped plasma membrane invaginations with a diameter of 50-100 nm and are abundantly present on many but not all eukaryotic plasma membranes [32]. Biochemical studies have revealed that caveolae are detergent resistant, highly hydrophobic membrane domains enriched in cholesterol and sphingolipids [33, 34]. In

addition to their role in endocytosis, caveolae have been implicated as signaling platforms, regulators of lipid metabolism and in cell surface tension sensing [35].

The main structural proteins of caveolae are members of the caveolin protein family, the most common being caveolin-1. Caveolin-1 is a small integral membrane protein that is inserted into the inner leaflet of the membrane bilayer. The cytosolic N-terminal region of caveolin-1 binds to cholesterol and functions as a scaffolding domain that binds to important signaling molecules [35]. Once thought to be sufficient for the formation of caveolae, it is now known that caveolins co-assemble with cytosolic coat proteins, called cavins to form these structures [36].

Live cell microscopy studies have revealed that caveolae are static structures and that CavMe is highly regulated and triggered by ligand binding to cargo receptors concentrated in caveolae. The steps involved in CavME are not as well understood as those involved in CME. However, caveolar budding from the plasma membrane is known to be regulated by kinases and phosphatases [37]. Numerous studies have shown that chemical inhibitors against Src kinase or phosphatases such as PP1 or PP2 alter CavME [38, 39]. Furthermore, like CME, dynamin is required to pinch off caveolae vesicles from the plasma membrane [40].

Clathrin Independent endocytosis:

More recently, it has become clear that other mechanistically distinct endocytic pathways mediate uptake of different subsets of signaling, adhesion and nutrient receptors, as well as regulate the surface expression of membrane transporters. These pathways have been

shown to be clathrin-independent endocytic (CIE) pathways, and as the name infers, the endocytic vesicles/tubules involved in CIE have no distinct coat and are not easily detected by EM. Thus, this pathway was first discovered by its resistance to inhibitors that block CME and CavME [41].

The term CIE encompasses several pathways, including an endophilin, dynamin and RhoA dependent pathway first identified for its role in IL-2 receptor endocytosis [5] and recently shown to mediate uptake of many other cytokine receptors and their constituents [42], a recently discovered clathrin- and dynamin -independent pathway, which involves the small GTPases Rac1, Cdc42 and leads to the formation of so-called clathrin-independent carriers (CLICs), and an Arf6-dependent pathway first shown to mediate MHCI uptake [43-46] (Figure 1). The role of these CIE pathways in the cell is still poorly understood. Furthermore, to what extent they contribute to the endocytic capacity of the cell remains unclear. Thus, whereas some studies suggest they are the major pathways for bulk uptake [6], other authors have suggested that CME can account for virtually all bulk uptake [47] and that CIE is induced only upon disruption of CME. However, a recent survey of endocytic activities in 29 different non-small cell lung cancer cells revealed that CIE pathways are differentially regulated relative to CME and CavME, providing strong evidence for their autonomy and functional importance [48].

Clathrin independent endocytosis can be further classified by their cargo and/or specific protein machinery. For example, lipid-anchored proteins such as GPI-APs are internalized through tubular structures, CLICs, that do not have any detectable protein coats and subsequently fuse to form a specialized early endosomal compartment called GPI-AP

enriched early endosomal compartments (GEECs). This process is therefore termed the CLIC/GEEC pathway. A second CIE pathway is the ARF6-associated pathway. Arf6 activation and inactivation modulates endocytic membrane trafficking by mediating the activation of phosphatidylinositol-4-phosphate 5-kinase (PIP5K) and production of $PI(4,5)P_2$ [49]. Flotillins also appear to play a role in a third dynamin- and clathrin-independent endocytic process, because previous studies have shown that cargo such as a GPI-anchored protein CD59 in HeLa cells is endocytosed in a flotillin-dependent manner [50]. Moreover, flotillin1 and -2 appear to induce membrane invaginations in a dose-dependent manner [51]. As each of these CIE pathways overlap in the cargo they take up, including GPI-APs and the transmembrane protein CD44 [52], it remains unclear as to whether they represent mechanistically distinct pathways or cell type and/or experimentally induced variations of the same pathway. Additional molecular machinery and mechanistic insights are needed to resolve these issues and better define these pathways.

Endocytosis in Human Disease:

The loss of function of any of the central components of CME such as: clathrin, AP2, and dynamin result in embryonic lethality [28, 53, 54]. Therefore, severe mutations of the key players are not seen in human disease. However, several perturbations of CME have been reported in numerous human diseases such as cancer, myopathies, neuropathies, metabolic genetic syndromes, and psychiatric and neurodegenerative diseases [18]. Likewise, core components of CavME have been shown to be altered in cancer [55-57] and CavME has

been suggested to play a role in a variety of diseases including diabetes, cardiovascular disease, and myopathies. Other cargos that are important for cell survival [50], signaling [58] and migration [59] traffic in a clathrin independent manner which is regulated by small GTPases, thus CIE pathways are also thought to be deregulated in human diseases, specifically cancer [60]. However, because so little is currently known about these pathways, more research is needed to fully understand their physiological importance.

Given the ubiquitous and critical nature of endocytosis, it has been usurped for both good and bad. Thus, viruses and toxins specifically target different endocytic pathways to invade the cell [61], and as more becomes known about the different pathways of endocytosis, researchers are developing methods to specifically target and deliver nanoparticles and therapeutics to diseased cells [62].

Mutations in Rabs [63-66], lipid phosphatases [67] and kinases [68, 69], and other components of the endosomal trafficking and sorting machinery are also linked to many human diseases [12, 70-72]. Though we have gained much insight into the molecular mechanisms of endosomal trafficking, there are still gaps in our knowledge of how cells have evolved specialized mechanisms for cargo detection, sorting, and trafficking. A deeper understanding of these mechanisms will lead to a better understanding of the link between endocytic membrane trafficking and human pathology.

Endocytosis and Cancer

Given its importance in controlling the internalization and expression of PM receptors, endocytosis and subsequent endosomal sorting and trafficking can regulate a

plethora of cancer-related cellular processes that are essential for efficient tumorigenesis including, cell proliferation and survival, polarity, signaling, adhesion, migration and nutrient acquisition. For example, previous studies have shown that RTKs such as EGFR, a known driver of cancer, can be trafficked differently depending on factors such as autophosphorylation, ligand affinity and its sensitivity to pH, ubiquitination, and several adaptor proteins. Activated RTKs are either trafficked to the late endosome and then the lysosome for degradation or recycled back to the PM from early endosomes allowing for sustained signaling [73]. Alterations in RTK trafficking factors have been found in many cancer cell lines [12].

Furthermore, it has been previously shown that altered endocytosis can change the trafficking of integrins and other cell adhesion molecules such as membrane matrix metelloproteases (MMPs) that are important for cell migration and adhesion. In order for a cell to sustain directed forward migration, integrins and RTKs such as EGFR must be constantly internalized by CME and recycled to the leading edge of the cell. A critical player is the rab coupling protein (RCP), a Rab11 effector, which binds to both integrins and RTKs. This enables co-trafficking of adhesion and signaling molecules to the leading edge of a migrating cell. RCP is down regulated by p63, a known tumor suppressor. Oncogenic mutants of p53 transcriptionally repress p63. Therefore, in cancer cells expressing mutant p53, both integrins and RTKs evade degradation in the lysosome and enhance cell migration by altering regulation of CME [74].

CavME, is important in membrane-type 1 matrix metalloproteinase (MT1-MMP) [75], fibronectin [76], and integrin [77] endocytosis and trafficking, is localized to both the

leading and trailing edge of a migrating cell, depending on 2D or 3D migration [78]. In order to migrate efficiently it is imperative that a cancer cell be able to remodel the ECM. This process requires both MMPs that help degrade the ECM at the leading edge of a cell and disassembly of FA, which occurs in part through internalization of integrins. As these events are regulated by CavME, it is thought that deregulation of the CavME pathway can lead to sustained cell migration.

Additionally, there are numerous examples of mutations in, or changes in the level of expression of components of the endocytic machinery in cancer cells. Furthermore, specific components of these pathways have previously been implicated in cancer metastasis. For example, Dyn2, a GTPase that catalyzes membrane fission and regulates clathrin-coated pit dynamics in CME, was found to regulate focal adhesion turnover. Knockdown of Dyn2 in prostate cancer cells prevented cell invasion in 3D and *in vivo* [79]. Caveolin-1 (Cav-1), an essential structural component of caveolae that functionally regulates the activity of many signaling molecules has been extensively studied in lung cancer [55-57]. Song et al. have shown in NCI-H460 lung cancer cells that siRNA knockdown of Cav1 causes an increased ability of these cells to migrate and invade *in vitro* [55].

More recently, it has become clear that other mechanistically distinct endocytic pathways mediate uptake of different subsets of signaling, adhesion and nutrient receptors, as well as regulate the surface expression of membrane transporters. CLIC-mediated endocytosis of key cargo adhesion proteins, CD44 and CD90/thy-1, is polarized to the leading edge of migrating cells, and inhibition of the CLIC pathway impairs the cell's ability to migrate in 2D [59].

Additionally, endocytosis plays a critical role in maintaining cell-to-cell junctions and polarity in epithelial cells, cellular features that cancer cells often lack. For example, clathrin knockdown experiments in epithelial cells caused mislocalization of basolateral proteins [80]. Furthermore, polarity-maintaining trafficking is highly regulated by Cdc42 and the Par group of proteins that are often altered in cancer [81, 82]. Cancer cells often undergo epithelial-mesenchymal transition or EMT, which represents a loss of cell-cell adhesions and apical-basal polarity and is a key step in progression towards metastatic disease [83]. Additionally, E-cadherins, an important component of adherens junctions are also tightly regulated by endocytosis mediated by Arf6, tyrosine kinases, and p120-catenin. It has been shown that differential activation of Arf6 can alter trafficking of E-cadherins [84-86] and alterations in expression or activation of components in these pathways have appeared in some cancers [87, 88]. Therefore, because of the important role endocytosis plays in maintaining cell-to-cell junctions and polarity in epithelial cells, alterations in these pathways could be one mechanism that leads to EMT in cancer cells.

The findings discussed above suggest that endocytosis, which dynamically controls the trafficking and PM levels of numerous molecules important for tumor progression plays a key role in altering cancer cell behaviors such as signaling, migration, and polarity. Despite this, a systematic evaluation of the role of the clathrin, caveolae, and CLIC/GEEC endocytic pathways in tumorigenesis in a single cancer model has never been done.

Therefore, the purpose of this work is to test the hypothesis that if specific endocytic pathways control different aspects of cancer cell behaviors that play critical roles in tumorigenesis, then particular endocytic pathways may be systematically altered in cancer

cells to gain a pathological advantage. To test our hypothesis, we screened a panel of NSCLC cell lines looking for differences in endocytic pathway efficiencies. We also looked for correlations between changes in specific endocytic pathways and changes in specific cellular behavior such as proliferation, migration, and growth in soft agar to determine if these differences are responsible for the ability of a cancer cell to be more aggressive. Subsequently, we tried to decipher and identify the important molecular players for these pathways and their specific role in cancer progression.

This research provides insight into the possible plasticity of endocytosis in a panel of NSCLC cell lines that can contribute to the evolution of aggressive cancers. Results from these studies might also identify possible biomarkers of highly aggressive cancers, and ultimately could lead to the discovery of potential new therapeutic targets that could decrease the devastating effects of lung cancer. Finally, these studies will advance the cell biology field through better understanding of the role of endocytosis in important cellular behaviors such as cell migration, proliferation, and signaling all of which are important processes in development and wound healing.

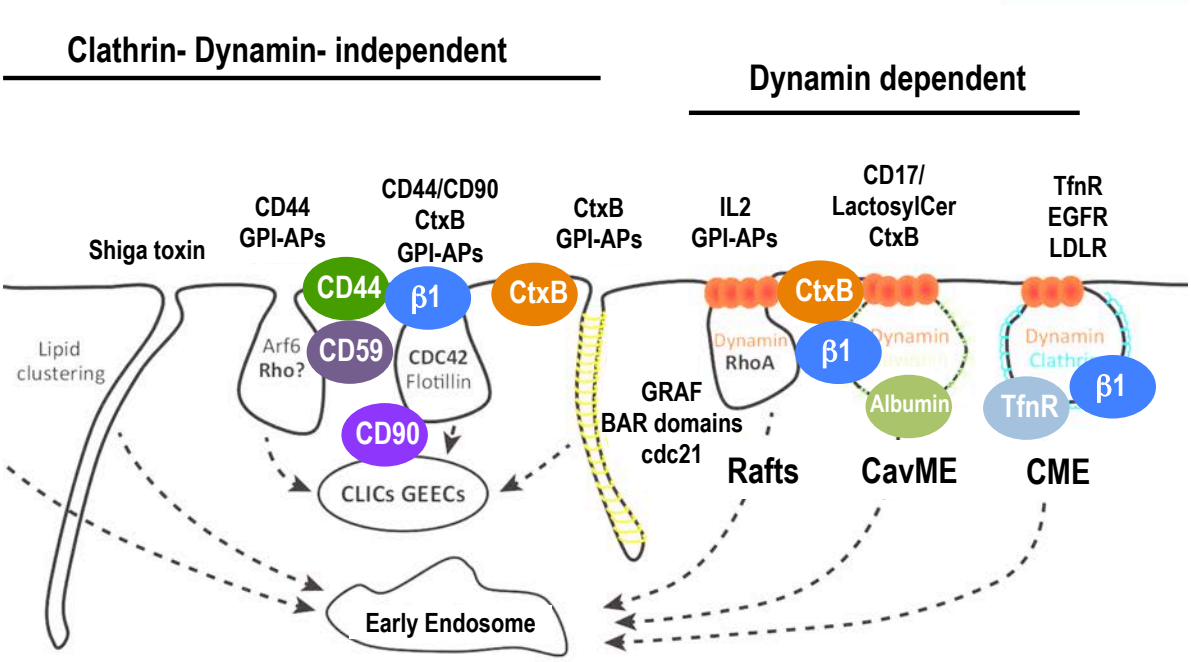

Figure 1: Schematic representation of the different endocytic pathways described in mammalian cells. The pathways can be broken into two main groups, dynamin-dependent and clathrin- and dynamin-independent pathways. Ligands known to traffic through each pathway, some of which have disease implications, are labeled along with the important molecular players of each pathway. The representation was inspired by [89].

CHAPTER TWO
Ikarugamycin: A Natural Product Inhibitor of Clathrin-Mediated Endocytosis

ADAPTED FROM ELKIN, S. R., N. W. OSWALD, D. K. REED, M. METTLEN, J. B. MACMILLAN AND S. L. SCHMID (2016). "IKARUGAMYCIN: A NATURAL PRODUCT INHIBITOR OF CLATHRIN-MEDIATED ENDOCYTOSIS." TRAFFIC 17(10): 1139-1149.

Abstract

Ikarugamycin (IKA) is a previously discovered antibiotic, which has been shown to inhibit the uptake of oxidized low-density lipoproteins in macrophages. Furthermore, several groups have previously used IKA to inhibit clathrin-mediated endocytosis (CME) in plant cell lines. However, detailed characterization of IKA has yet to be performed. Consequently, we performed biochemistry and microscopy experiments to further characterize the effects of IKA on CME. We show that IKA has an IC50 of 2.7 μM in H1299 cells and acutely inhibits CME, but not other endocytic pathways, in a panel of cell lines. Although long-term incubation with IKA has cytotoxic effects, the short-term inhibitory effects on CME are reversible. Thus, IKA can be a useful tool for probing routes of endocytic trafficking.

Introduction

Cell surface receptors and their bound ligands (i.e. cargo) can be internalized by one of several mechanistically distinct endocytic pathways [44]. These include, clathrin-mediated endocytosis (CME), caveolae-mediated endocytosis (CavME) and less well-defined clathrin

and caveolae-independent mechanisms (CIE). While CME is likely to be the major pathway in mammalian cells for concentrative uptake, specialized cargo molecules, viruses and toxins utilize other pathways for their selective uptake [60, 61]. Given this complexity, there remains a need for acute and specific chemical inhibitors to discern how different cargos utilize the different pathway(s).

CME can be inhibited in a number of ways, each with their limitations. For example, long-term knockdown or knockout of key components of the endocytic machinery can have complex indirect effects on cellular functions and/or can induce possible compensatory mechanisms, as can the overexpression of dominant-negative constructs. Other methods such as cytosolic acidification [90], hypertonic shock [91] and potassium depletion [92], have acute, but potentially pleiotropic effects. Several chemical inhibitors such as monodansylcadaverine (MDC) [93], chlorpromazine [94], and phenylarside oxide (PAO) [95] have unknown mechanisms of action and therefore uncertain specificity. More recently, small molecule inhibitors of dynamin, such as Dynasore [96], Dynole-34-2 and Dyngo [97], or of clathrin-coated pit (CCP) maturation, such as Pitstop [98] have been identified in chemical screens as inhibitors of CME. However, these chemicals exhibit low potency and their specificity and mechanism of action have been questioned. For example, Dynasore and its derivative Dyngo continue to inhibit endocytosis in triple dynamin-null mouse embryo fibroblasts [99], and may also affect plasma membrane (PM) cholesterol independently of

their role in endocytosis [100]. Similarly, Pitstop has been shown to also potently inhibit CIE [101] and its mechanism of action has been brought into question [102].

The natural product, ikarugamycin (IKA) was first isolated from cultures of *Streptomyces phaeochromogenes* and shown to have antiprotozoal activity [103]. IKA has been reported to reduce the rate of oxidized LDL uptake in J774 macrophages [104], as well as to inhibit Nef-dependent downregulation of CD4 in U937 monocytic cells [105]. IKA has been used to inhibit CME in plant cells [106, 107]. However, neither its potency, the nature of its inhibitory effects, nor its specificity towards CME have been examined. Thus, given the need for a more potent, selective and acute inhibitor of CME, we have further characterized IKA as a potentially useful tool to selectively inhibit this endocytic pathway.

Materials and Methods

Cell lines and culture

HBEC3KT were kindly provided by J. Shay (UT Southwestern) and cultivated in complete KSF medium. All NSCLC lines used in this study (H1299, HCC366, H1437) were obtained from the Hamon Cancer Center Collection (University of Texas Southwestern Medical Center) and maintained in RPMI-1640 (Life Technologies) supplemented with 5% fetal calf serum. HeLa and human retinal epithelia ARPE-19 cell lines were obtained from American Type Culture Collection (ATTC) and cultivated in DMEM-5% FBS (Sigma) or in

DMEM/F12-10% FBS, respectively. All cell lines were cultured at 37∘C in a humidified atmosphere containing 5% CO2 and 95% air. All cell lines have been DNA fingerprinted using the PowerPlex 1.2 kit (Promega) and are mycoplasma free using the e-Myco kit (Boca Scientific). Culture media were purchased from Life Technologies.

*Antibodies and reagent***s**

Anti-TfnR (HTR-D65) monoclonal antibody was produced in hybridoma as in [108]. Anti-CHC (sc-12734) and anti-Dyn-2 (sc-64000) antibodies were purchased from Santa Cruz Biotechnology. Anti-ERp72 (5033) and Anti-GM130 (ab52649) antibodies were purchased from Cell Signaling Technology and Abcam, respectively. Anti-γ-adaptin (610385), anti-EEA1 antibody (#610457), anti-LAMP2 (555803), FITC-conjugated-anti-CD44 (G44-26) and anti-CD59 (p282-H19) monoclonal antibodies were obtained from BD Pharmingen™. Horseradish peroxidase (HRP)- and AlexaFluor®-conjugated antibodies were purchased from Life Technologies. Biotinylated albumin (#A8549), OPD (#P1536), IKA (#SML0188), anti-β-actin (#A5441) and anti-CD8 (#C7423) were obtained from Sigma-Aldrich. Anti-EGFR (MS-396-P) and anti-α-adaptin (MA3-061) antibodies were purchased from Thermo Scientific. Streptavidin-POD was purchased from Roche. Fluoromount G and PFA were purchased from Electron Microscopy Sciences.

TfnR, albumin, CD44, CD59, LDLR/CD8 and EGFR internalization

Assays were performed in PBS4+ (PBS supplemented with 1 mmol/LMgCl2, 1 mmol/L CaCl2, 5 mmol/L glucose, and 0.2% BSA) using receptor-specific monoclonal antibodies as ligands for TfnR, CD44, CD59, and CD8 or biotinylated albumin to measure CavME exactly as described in (24). Briefly, 2.8×10^4 cells/well on collagen coated 96-well plates and cultured overnight. For assays, cells were washed with PBS^{4+}, and then incubated for the indicated times at 37◦C in $PBS4^+$ containing 4 μg/mL of the indicated ligand before being rapidly cooled on ice, washed with cold PBS4+ and then stripped of remaining surface-bound mAbs by an acid wash (5 × 2 min 0.2 M acetic acid, 0.2 M NaCl, pH 2.5). Cells were then fixed in 4% PFA, permeabilized with 0.1% Triton-X100 and internalized mAbs detected and quantified using an HRP-conjugated secondary antibody and OPD detection. The absorbance was read at 490 nm using a Biotek Synergy H1 Hybrid Reader. Well-to-well variability in cell number was accounted for by normalizing the reading at 490 nm with a bicinchoninic acid (BCA) readout at 560 nm (Biotek Synergy H1 Hybrid Reader). The fraction of internalized ligand was calculated relative to the initial total surface bound ligand at 4◦C (without the acid wash step) measured in parallel for all the assays.

EGFR internalization was performed similar to the assays above, except cells were stimulated with 20 ng/mL EGF in the presence of Ab-11, a non-perturbing monoclonal antibody towards EGFR.

ARPE-19 cells were plated on 96-well plates at a density of 2.0×10^4 cell/well and co-infected with adenoviruses coding for the CD8/LDLR chimera and adenoviruses coding

for a tet-repressible transcription activator [109]. After overnight incubation in the presence of 75 ng tet/mL (low overexpression, control cells), cells were washed three times in PBS and internalization assays were performed as described above using an anti-CD8 antibody.

IKA inhibition

For inhibition by IKA, cells were preincubated in the absence (control) or presence of defined concentrations of IKA for varied time points at 37°C before internalization assays were performed as described above except the $PBS4^{+}$ contained IKA. IKA was stored in 1000× stock solutions in 100% dimethyl sulphoxide (DMSO) at −20°C for up to 2 months per the manufactures instructions. All experiments were preformed with equal DMSO concentrations per condition and a DMSO control.

Immunofluorescence

ARPE-19 cells expressing enhanced green fluorescent protein, fused of the N-terminus of clathrin light chain a (eGFP-CLCa) grown overnight on glass cover slips, were preincubated in the absence (control) or presence of 4 μM of IKA for 3 h at 37∘C, washed with PBS and fixed in 4% PFA in PBS for 10 min at room temperature, permeabilized with 0.1% Triton X-100 for 2 min and further blocked with Q-PBS (0.01% saponin, 2% BSA, 0.1% lysine, pH 7.4) for 1 h. After three washes with PBS, cells were incubated with the indicated primary antibody in Q-PBS for 1 h using the recommended dilution. Cells were

washed three times with PBS and further incubated with suitable AlexaFluor®-labeled secondary antibodies for 1 h. After three additional washes with PBS, samples were mounted on Fluoromount G on glass slides and examined using either 60× or 100× 1.49 NA objectives (Nikon) mounted on an epifluorescence Ti-Eclipse inverted microscope.

Fractionation

Cells grown in 150 mM dishes were washed twice with PBS and harvested in PBS containing 5 mM ethylenediaminetetraacetic acid (EDTA). Protein concentration was determined and low-speed cell pellets were gently resuspended in fractionation buffer (25 mM sucrose, 1 mM MgCl2, 2 mM EGTA, 25 mM HEPES, pH 7.4) to equal protein concentration – the lowest protein condition being resuspended in 300 µL. Cells were lysed by three cycles of freezing/thawing in liquid N_2 and equal volumes of whole cell lysates were centrifuged at 110 000× ***g*** in a TLA100.2 Beckman rotor (Beckman Coulter Inc.) for 30 min. The soluble fraction (cytosolic fraction 'C') was collected and pellets (membrane fraction 'M') were resuspended in 150 µL fractionation buffer and sonicated. The 'C' fraction was further diluted 2× and equal volumes of each fraction were loaded onto an SDS gel. After transferring to a nitro-cellulose membrane, membranes were probed with antibodies against the following proteins: AP1, AP2, CHC, GAPDH, Na^+/K^+ ATPase and Actin.

Cell viability and caspase 3/8/9 activation

Measurement of cell viability/cytotoxicity was performed by using the CCK-8 Counting Kit (Dojindo), which measures dehydrogenase activity in viable cells. Briefly, 1×10^5 cells/well cells were treated with either 4 or 32 μM of IKA in 96-well plates for increasing time periods at 37°C, and analyzed according to the manufacturer's instructions. To measure viability in parallel to uptake assays cells were plated at the same density under the same conditions as the uptake conditions.

Caspase-3, -8 and -9 activations were assessed using western blotting. Briefly, ARPE-19 cells were treated with 4 μM IKA for either 2, 4, or 8 h, or no treatment (control), washed three times with PBS and harvested/resuspended in 200 μL of reducing Laemmli sample buffer. The cell lysate was boiled for 10 min and loaded onto an SDS gel. After transferring to a nitrocellulose membrane, membranes were probed with antibodies against the following proteins: caspase-3, -8 and -9.

TIRF microscopy

Total internal reflection fluorescence (TIRF) microscopy was per- formed using ARPE-19 cells stably expressing eGFP-CLCa and imaged using a 100 × 1.49 NA Apo TIRF objective (Nikon) mounted on a Ti-Eclipse inverted microscope equipped with the Perfect Focus System (Nikon). During imaging, cells were maintained in medium lacking phenol red containing 4 μM IKA or not (control). Time-lapse image sequences from different cells were acquired at a frame rate of 1 frame/second and exposure time of 150 ms using a pco-edge 5.5

sCMOS camera with 6.5 μm pixel size. Cells were either treated with 4 μM of IKA for 3 h before imaging or not (control) and then immediately imaged.

Image and data analyses of CCP dynamics were carried out in Matlab (MathWorks), using custom-written software. Up-to-date versions of the software will be made available at http://lccb.hms.harvard.edu/software.html.

Electron microscopy

Rip-off

Cells were applied to EM grids (carbon film 200 mesh gold – Electron Microscopy Sciences) coated with collagen and allowed to adhere overnight under normal culture conditions. IKA was added to the cells at the desired concentration and incubated for 3 h, after which the grids with adhered cells were washed and processed for 'rip-off' images. After washing with cold PBS (20 mM sodium phosphate pH 7.4, 150 mM sodium chloride), grids with adhered cells were fixed lightly with 0.5% (v/v) paraformaldehyde (PFA) in PBS for 2′. Grids were then washed with PBS and hypotonic buffer (25 mM HEPES, pH7.2 with 25 mM potassium chloride and 2.5 mM magnesium acetate). The last wash of hypotonic buffer was left n the cells to swell slightly for 10′ –15′. The grids were then quickly placed, cell side down, onto cover slips previously coated with poly-L-lysine. A small piece of filter paper (GE Osmonics Inc., cat. # A02SP02500) was used to wick off the moisture as the grid was pulled quickly and laterally away from the cover slip. The grids were then fixed in 2%

(v/v) PFA in PBS for 10′; 3 × 5′ washes in H2O; 10′ fixation in 2% (v/v) glutaraldehyde in H2O; 2 × 5 washes in H2O; 1 in 1% tannic acid (w/v) in H2O; 3 × 5′ washes in H2O; 1′ in 1% (w/v) uranyl acetate; 2 × 5′ washes in H2O. Droplets were wicked away from the grids with filter paper pieces and finally the grids were laid out on filter paper to air dry until imaged.

Thin-sectioning

Cells were applied to collagen-coated glass-bottomed dishes (MatTek) and allowed to adhere overnight under normal culture conditions. IKA was added to the cells at the desired concentrations and incubated for 3 h. Cells were then washed with cold PBS and fixed in 2.5% (v/v) glutaraldehyde in 1.1M sodium cacodylate buffer. Processing for embedding and sectioning continued as follows: after three rinses in 0.1 M sodium cacodylate buffer, they were post-fixed in 1% osmium in 0.1 M sodium cacodylate buffer for 1 h. Cells were rinsed in 0.1 M sodium cacodylate buffer and *en bloc* stained with 0.5% tannic acid in 0.05 M sodium cacodylate buffer for 30 min. After two rinses in 1% sodium sulfate in 0.1 M sodium cacodylate buffer, samples were rinsed three times in 0.1 M sodium cacodylate buffer and five times in water. Samples were then dehydrated through a series of increasing concentrations of ethanol, and infiltrated and embedded in Embed-812 resin. Enough resin was added into the MatTek dishes to just fill the well and polymerized at 60∘C. Polymerized samples were dropped into liquid nitrogen to pop out the resin disks from center of the

MatTek dish. Two resin disks containing the same sample were sandwiched together with fresh Embed-812, monolayers were facing each other. Resin disks were polymerized at 60∘C over-night and sectioned along the longitudinal axis of the two monolayers of cells with a diamond knife (Diatome) on a Leica Ultracut UCT 6 ultramicrotome (Leica Microsystems). Sections were post-stained with 2% (w/v) uranyl acetate in water and lead citrate.

Imaging

All EM images were acquired ona Tecnai G2 Spirit transmission electron microscope (FEI) equipped with a LaB6 source at 120 kV using a Gatan ultrascan CCD camera.

Results

IKA inhibits CME of multiple receptors in several cell lines

To determine the potential of IKA as an inhibitor of CME, we first examined the effect of increasing concentrations of IKA on the clathrin-mediated uptake of the transferrin receptor (TfnR) in H1299 cells pretreated with IKA for 1 h. We observed a dose-dependent decrease in TfnR uptake with increasing IKA concentrations and determined an IC_{50} of 2.7 ± 0.3 μM (Figure 1A).

We next asked if IKA could inhibit CME in multiple cell lines, including H1299, HCC366 and H1437 cells (non-small cell lung cancer (NSCLC) cell lines), ARPE-19 (retinal pigment epithelial cells) and HBEC3KT (bronchial epithelial cells). We measured TfnR uptake at 5 min after preincubating cells for 3 h in the presence 4 μM IKA (Figure 1B). TfnR uptake was inhibited by ~80% in H1299, HCC366, and ARPE-19 cells, and by ~50% in H1437 and HBEC3KT. These results suggest that IKA is able to inhibit TfnR uptake in a variety of human cell lines.

To determine if IKA inhibited CME broadly or was receptor specific, we tested other receptors known to traffic in a CME-selective manner. TfnR, low-density lipoprotein (LDL) receptor (LDLR), and the epidermal growth factor receptor (EGFR) all traffic through CME but require different adaptor molecules [110]. Because most cells only express low levels of LDLR, we used a tetracycline-regulatable adenoviral expression system to express CD8-chimeras encoding the LDLR FxNPxY internalization motif [111] in ARPE-19 cells, whereas TfnR and EGFR uptake experiments were performed in H1299 cells. CME of each of these receptors was inhibited in cells pretreated with 4 μM of IKA for 3 h (Figure 1C). While there was apparently less inhibition of LDLR uptake, we believe this reflects the slight overexpression of CD8-LDLR chimeras obtained with tet-regulatable expression resulting in partially satu- rated CME [111], rather than a reduced affect on receptors that utilized adaptors other than AP2. Indeed, IKA was originally shown to inhibit oxidized LDL uptake [104].

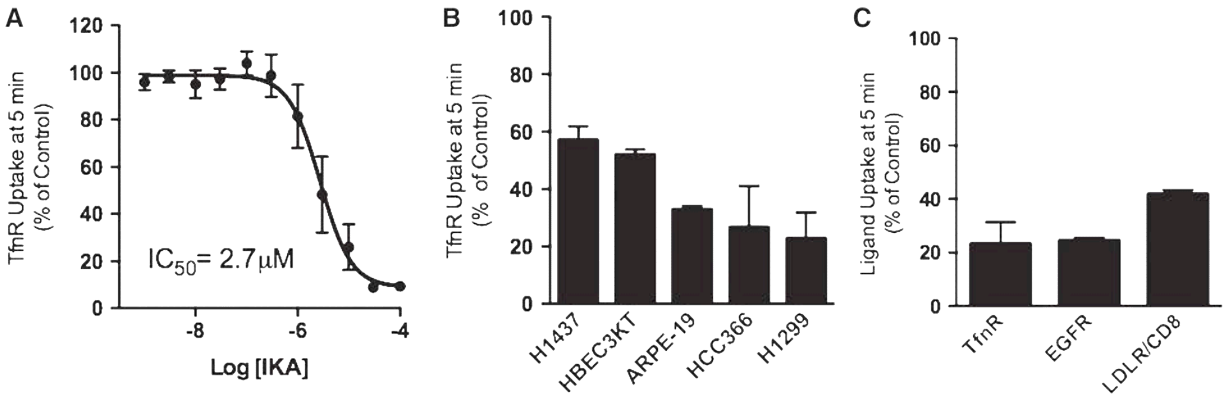

Figure 1: Ikarugamycin inhibits clathrin-mediated endocytosis. A) A semi-log plot of the effect of increasing concentrations of IKA on TfnR uptake in H1299 cells. IKA has an IC_{50} value of 2.7 μM ± 0.3. B) Effect of IKA on Tfn uptake in several different cell lines. The indicated cells were preincubated with 4 μM IKA before uptake of TfnR was measured. Results are reported as amount of TfnR internalized after 5 min at 37°C as a % of untreated control cells. C) Under the same conditions as (B) IKA inhibits uptake of several CME specific receptors: TfnR (H1299), EGFR (H1299) and LDLR (ARPE-19). All experiments represent (n=3, avg. ±SD).

Finally, we tested the specificity of IKA inhibition by measuring its effects on other endocytic pathways. To do this, we used endocytic assays previously developed in our lab to follow CavME, measured by uptake of albumin, and multiple CIE pathways, measured by uptake of CD44 and CD59 [48]. IKA showed no inhibition of CavME and CIE over a range of 1 – 4 μM, whereas TfnR uptake was significantly inhibited over this concentration range (Figure 2). These results show that IKA selectively inhibits CME over other modes of endocytosis.

IKA inhibition is rapid and reversible

To further characterize IKA, we next explored the rate of onset and reversibility of its inhibitory effects on CME. Acute treatment with 4 μM IKA decreased TfnR uptake in H1299 cells by 40%, which increased to 80% inhibition after 3 h preincubation (Figure 3A). In the absence of preincubation, the dose–response curve for IKA inhibition was shifted to higher concentrations and complete inhibition of TfnR uptake required >30 μM IKA (Figure 3B).

We next asked if IKA treatment was reversible. H1299 cells were pretreated with 4 μM IKA for 10, 30 or 180 min. IKA was then washed out for 0, 30 or 180 min to assess if CME could recover after removal of IKA. CME in cells pretreated with IKA for 10 or 30 min to achieve ~55 and ~65% inhibition, respectively, completely recovered by 180 min after washout. However, CME in cells pretreated with IKA for 180 min to achieve full inhibition,

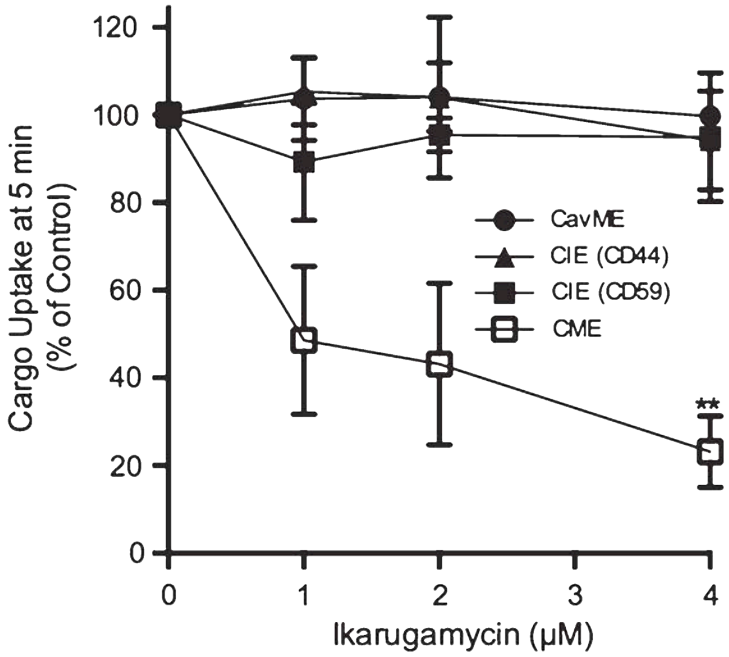

Figure 2: Ikarugamycin is selective for CME. The effect of increasing concentrations of IKA on caveolae-mediated endocytosis (•), using albumin as ligand, clathrin-independent endocytosis using either CD44 (Δ) or CD59 (■) as markers, or clathrin-mediated endocytosis using TfnR (□) as marker in H1299 cells pretreated for 3 h. Data are normalized to the extent of internalization after 5 min in control cells, which was 69 ± 24% for albumin, 23 ± 13% for CD44, 27 ± 16% for CD59 and 109 ± 28% for TfnR control. Two-tailed Student's t-test were used to assess statistical significance. **$p < 0.005$; ($n = 3$, avg. ± SD).

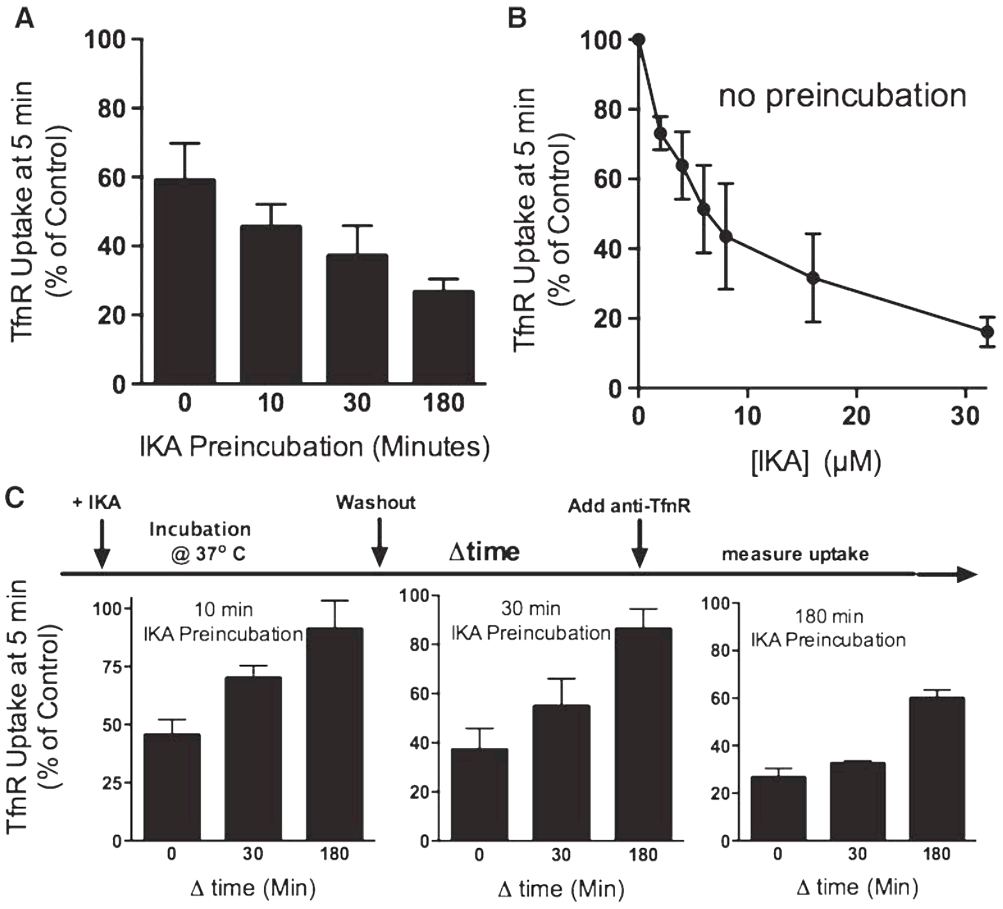

Figure 3: Ikarugamycin inhibition of CME is rapid and partially reversible. A) H1299 cells were pretreated with 4 μM IKA for increasing time and inhibition of TfnR uptake in the continuous presence of IKA was compared with control. B) Increasing concentrations of IKA were added without preincubation and TfnR uptake was measured after 5 min H1299 cells after 5 min in the continuous presence of IKA. C) H1299 cells were pretreated with 4 μM IKA for increasing time periods then IKA was washed out for either 30 or 180 min. TfnR uptake was then measured and compared with control (no IKA treatment). All experiments represent (n = 3, avg. ± SD).

only partially recovered to ~60% TfnR uptake relative to controls after 180 min (Figure 3C). These results show that IKA can act quickly at high concentrations and is partially reversible.

IKA affects CCP morphology and dynamics

To better understand how IKA might be disrupting CME, we next examined the distribution of CCPs in control and 4 μM IKA-treated ARPE-19 cells by immunofluorescence labeling of clathrin light chain (CLC) and adaptor protein 2 (AP2), the major coat proteins. Interestingly, the uniformly distributed CCPs in untreated ARPE-19 cells appeared to cluster and align along tracks in treated cells (Figure 4A). This was also seen in electron microscopy (EM) images of 'ripped off' PMs from IKA-treated cells in which grape-like clusters of CCPs were frequently observed adjacent to filamentous material (Figure S1, Supporting Information).

A previous study of endocytosis in plant cells demonstrated that IKA treatment caused a redistribution of clathrin from cytosolic pools to the PM [106]. We observed a similar redistribution of clathrin and AP2 using western blotting of membrane and cytosolic faction of ARPE-19 cells treated or not treated with IKA (Figure 4B). Quantification showed a significant difference between the amounts of CHC at the PM compared with control cells (Figure 4C). This was even more apparent with AP2, which is a specific marker of PM-associated CCPs (Figure 4B and D). Because clathrin is associated with both Golgi and PM, we tested whether IKA treatment also altered the subcellular distribution of adaptor protein 1

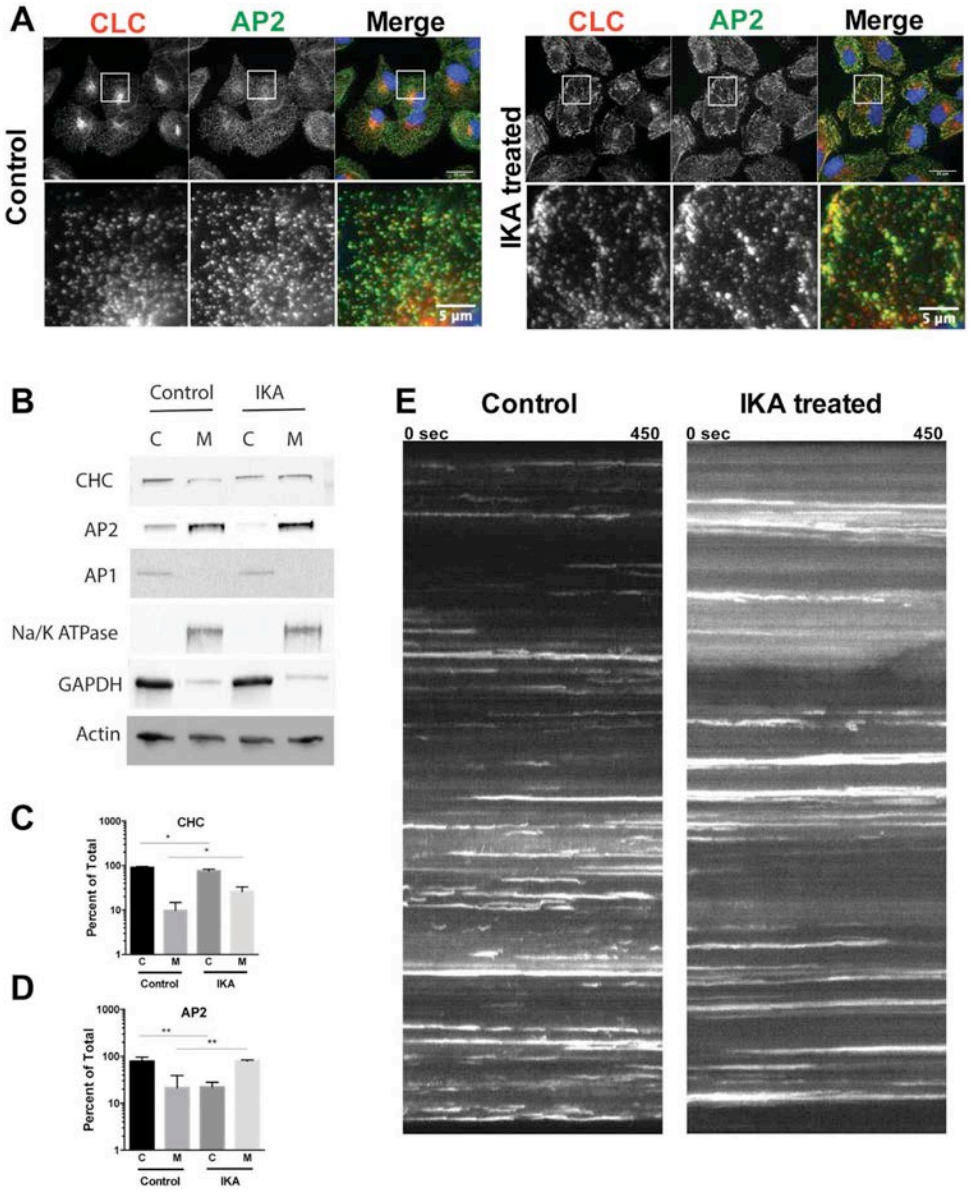

Figure 4: Ikarugamycin disrupts clathrin coated pit distributions. A) Immunofluorescence of control/untreated ARPE-19 cells or cells pretreated with 4 µM IKA for 3 h probed with antibodies to CLC and AP2. B) Fractionation of ARPE-19 cells pretreated with 4 µM IKA for 3 h or no pretreatment (control) probed for clathrin heavy chain (CHC) and AP1 and AP2, respectively. The cytosolic (C) fraction was diluted 4× compared with the membrane (M) fraction for western blotting. Na+/K+ ATPase and GAPDH were used as positive and negative controls respectively. C and D) Quantification of

CHC and AP2 in membrane versus cytosolic fractions, respectively, plotted on a log scale as percent of total. Two-tailed Student's t-test were used to assess statistical significance. *$p < 0.05$; **$p < 0.005$; ***$p < 0.0005$. All experiments represent ($n = 3$, avg. ± SD). E) Kymographs from time-lapse images of CLC in either ARPE-19 cells pretreated with 4 μM IKA for 3 h or no pretreatment (control). Kymographs are 450 seconds and span 130 μm.

(AP1), the Golgi-specific clathrin adaptor. Unlike AP2, IKA treatment did not alter the cellular distribution of AP1 (Figure 4B), suggesting that its effects were selective to PM-associated CCPs.

Finally, we tested the effect of IKA treatment of CCP dynamics using live cell total internal reflection fluorescence microscopy (TIRFM) of APRE cells stably expressing eGFP-CLCa. In untreated control cells, CCPs are dynamic structures, most of which assemble and pinch-off during a 7.5 min movie, illustrated by the kymograph in Figure 4E. In contrast, most of the CCPs in IKA-treated cells remain static throughout the entire movie (Figure 4E). Thus, IKA appears to block the maturation and/or pinching off of CCPs.

IKA alters Golgi morphology

Despite the lack of effect of IKA treatment on the subcellular distribution of AP1, immunofluorescence images revealed subtle alterations in Golgi morphology (Figure 5A). The Golgi markers AP1 and GM130 appeared slightly more disperse and disorganized in IKA-treated cells relative to control. This was confirmed in EM studies in which the Golgi appeared to be more disorganized and vesiculated in IKA-treated cells (Figure 5B). We examined other organelles by immunofluorescence including endosomes (by EEA1 staining), lysosomes/late endosomes (by LAMP2 staining) and the endoplasmic reticulum (by ERp72 staining) and observed no apparent differences between control and IKA-treated cells (Figure S2A, B and C, respectively).

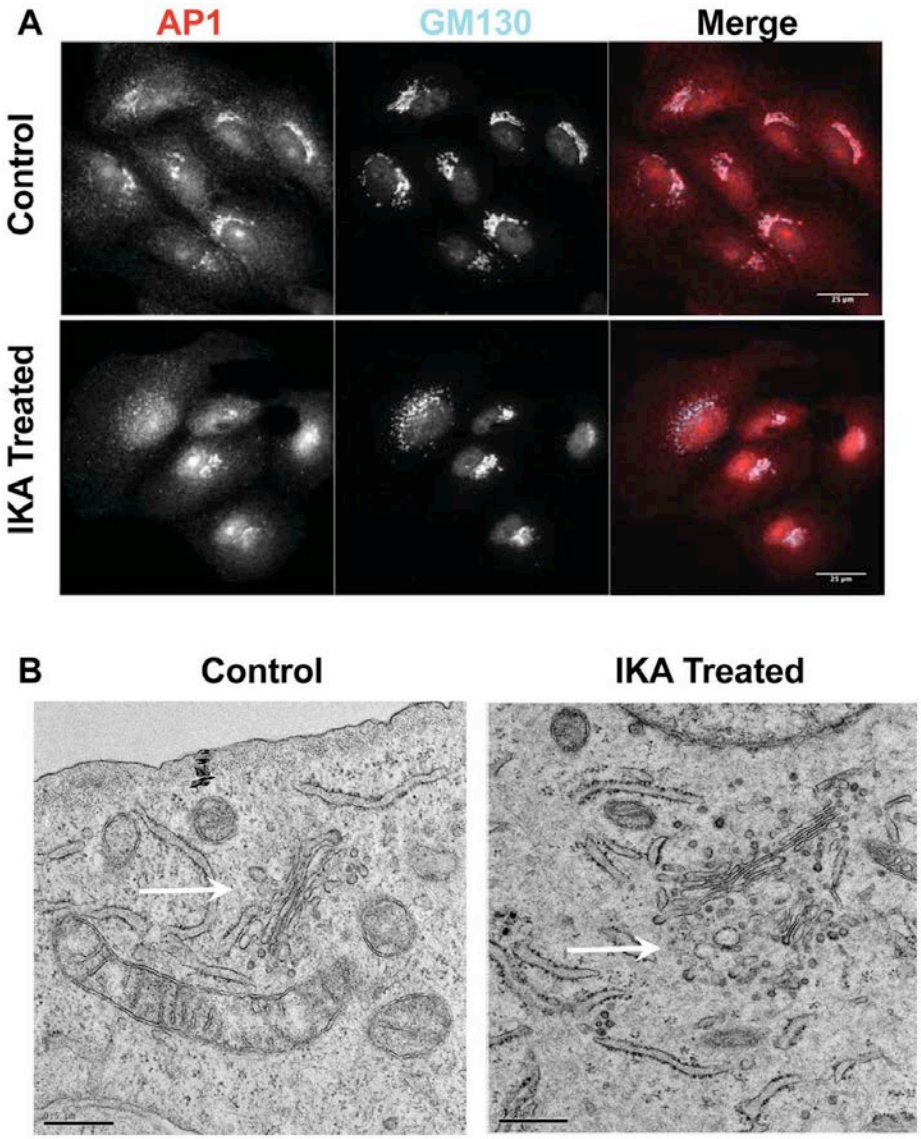

Figure 5: Ikarugamycin alters Golgi morphology. A) Immunofluorescence of ARPE-19 stably expressing eGFP-CLC either pretreated or not (control) with 4 μM IKA for 3 h and probed with anti- bodies to adaptor protein 1 (AP1) and GM130. Scale bar = 25 μm. B) Electron microscopy (EM) images of either con- trol or IKA treated cells. White arrows point to the Golgi in each condition. Scale bar = 0.5 μm.

IKA and cell viability

Previous studies had shown that IKA can induce apoptosis in HL-60 leukemia cells, with corresponding cleavage of caspases-9, -8 and -3 starting ~4 h after treatment with 400 nM IKA [112]. The reported IC_{50} for cytotoxicity in HL-60 leukemia cells was ~220 nM, much lower than the IC_{50} for inhibition of TfnR uptake we report in H1299 cells after 1 h preincubation. We therefore closely examined the effects of IKA treatment on induction of cell death in three different cell lines commonly used for studies on endocytosis: ARPE-19, HeLa and H1299. Cells were incubated with 4 μM of IKA for increasing times up to 48 h. At early time points (0 – 8 h treatment), when endocytosis was severely inhibited, cells showed no significant decrease in cell viability, consistent with the reversibility of IKA after short incubation times (Figure 2C). Consistent with this, we were unable to detect cleaved caspase -9, -8 and -3 using western blotting even after8h of incubation with 4 μM IKA (Figure S3). However, starting at 12 h, significant effects on cell viability were observed, and by 48 h, only 20% of cells were still viable (Figure 6A). We have shown that 32 μM IKA acutely and completely inhibits CME (Figure 3B). At this concentration, decreases in cell viability could be detected within 1 h, and only 20% of cells remained viable aft r 8 h of incubation (Figure 6B).

Putting these experiments together, we measured the effects of IKA treatment (10 μM aft r 15 min preincubation) on TfnR uptake in APRE cells and H1299 cells (Figure 7A and B, respectively). TfnR uptake was strongly inhibited under these conditions, while cell viability

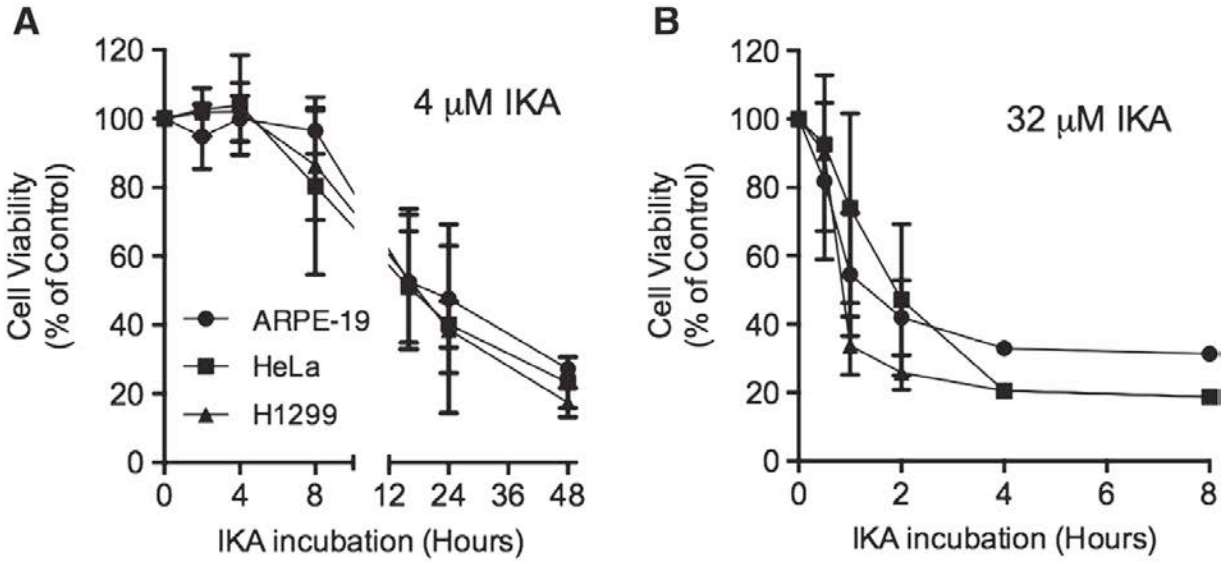

Figure 6: The effect of ikarugamycin on cell viability. ARPE-19, HeLa and H1299 cells were treated with A) 4 μM or B) 32 μM IKA for increasing periods of time followed by measuring cell viability. All experiments represent (n = 3, avg. ± SD).

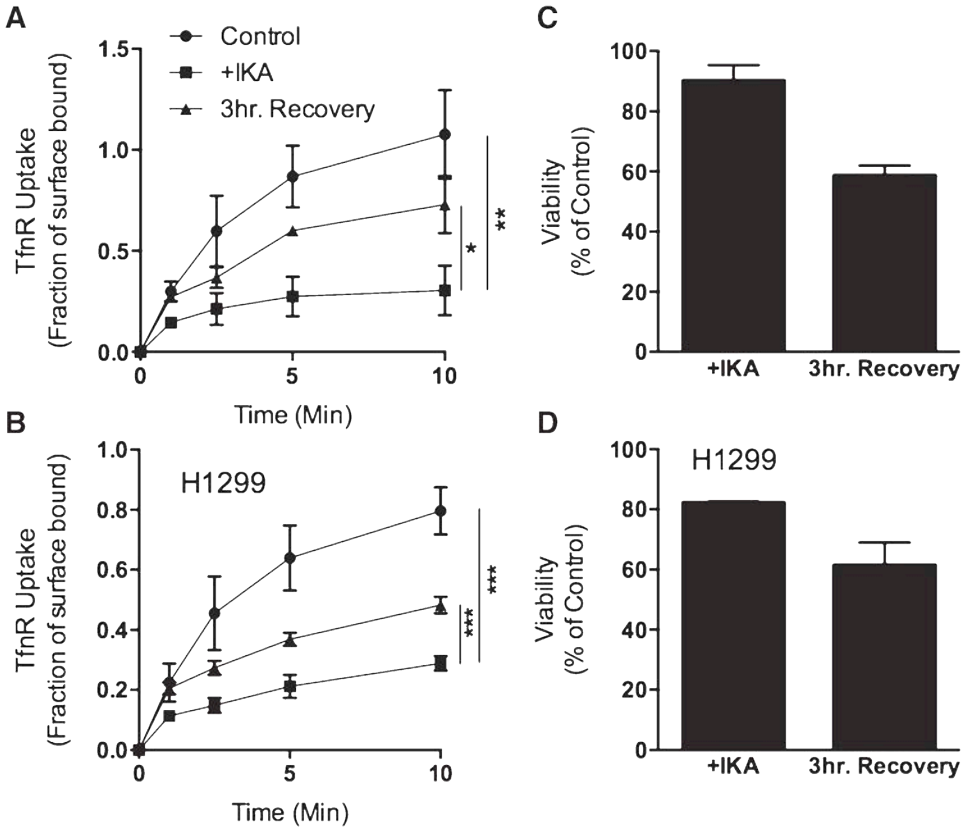

Figure 7: Ikarugamycin inhibition of CME is rapid and partially reversible at high concentrations. A) ARPE-19 cells or B) H1299 cells were pretreated with 10 μM IKA for 15 min then IKA was either washed out for 3 h or not. TfnR uptake was then measured and compared with control (no IKA treatment). C) ARPE-19 or D) H1299 cells were treated with 10 μM IKA for 15 min then IKA was washed out for 3 h or not followed by measuring cell viability. Two-tailed Student's t-tests were used to assess statistical significance. *$p < 0.05$; **$p < 0.005$; ***$p < 0.0005$. All experiments represent ($n = 3$, avg. ± SD).

was unaffected during the experimental time course (Figure 7C and D). However, we detected a decrease in cell viability during a subsequent 3 h washout (Figure 7C and D) and consistent with this only a partial recovery of complete CME activity (Figure 7A and B).

Together our data confirm and extend previous reports, primarily in plant cells, that, if judiciously used (we recommend 4 μM IKA with preincubations of ≤30 min), IKA can provide a useful tool to acutely and specifically inhibit CME over other endocytic trafficking pathways in mammalian cells.

Discussion

We have characterized IKA, a naturally occurring and commercially available antibiotic, previously shown to inhibit CME in macrophages and plant cells, to determine whether it might be a useful general tool to study and distinguish endocytic pathways in mammalian cells. We show that IKA selectively inhibits CME over other modes of endocytosis with an IC_{50} of 2.7 μM after 1 h preincubation. IKA disrupts CCP morphology causing a redistribution of AP2 and CHC to the PM. IKA can act quickly at high concentrations and is partially reversible. Based on these characterizations, we believe that IKA can be a useful tool for the endocytosis field as an acute and selective inhibitor of CME.

However, similar to MDC, chlorpromazine, Dynasore and Dyngo4a, we do not know the specific target of IKA responsible for these effects on CME. Moreover, at high, and

potentially variable and cell-type specific concentrations, and/or after longer incubation times, IKA can affect cell viability. Therefore, as for all chemical inhibitors, conditions must be optimized and control experiments (such as concentration curves and reversibility) need to be performed to ensure its judicious use. Nonetheless, because IKA can acutely and reversibly inhibit CME selectively over other endocytic pathways it may prove a useful tool under specific conditions to inhibit CME.

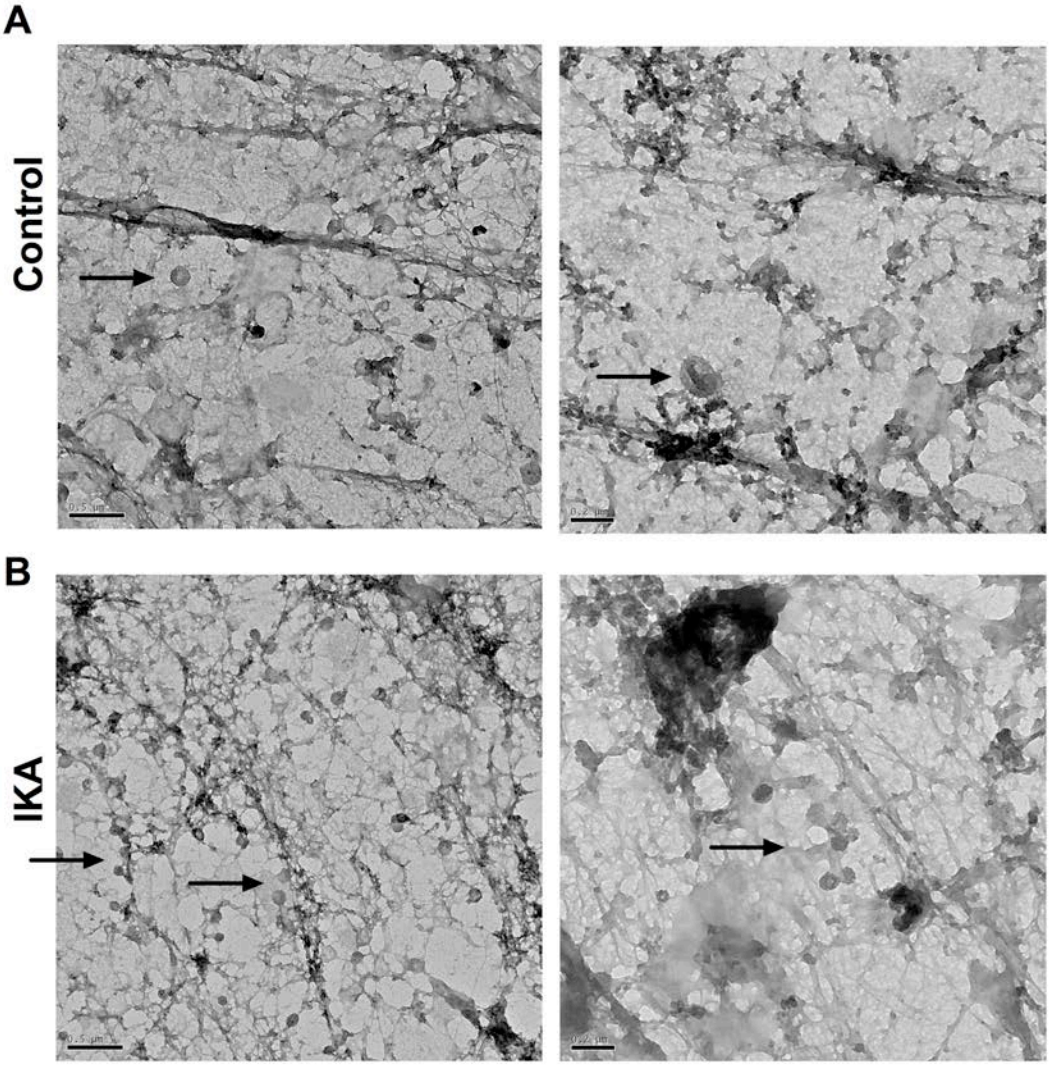

Supplemental Figure 1: Ikarugamycin affects clathrin coated pit morphology. EM images of A) control ARPE-19 cells and at B) IKA treated ARPE-19 cells at different magnifications. Arrows indicate examples of normal (control) and altered (IKA-treated) clathrin coated pits respectively.

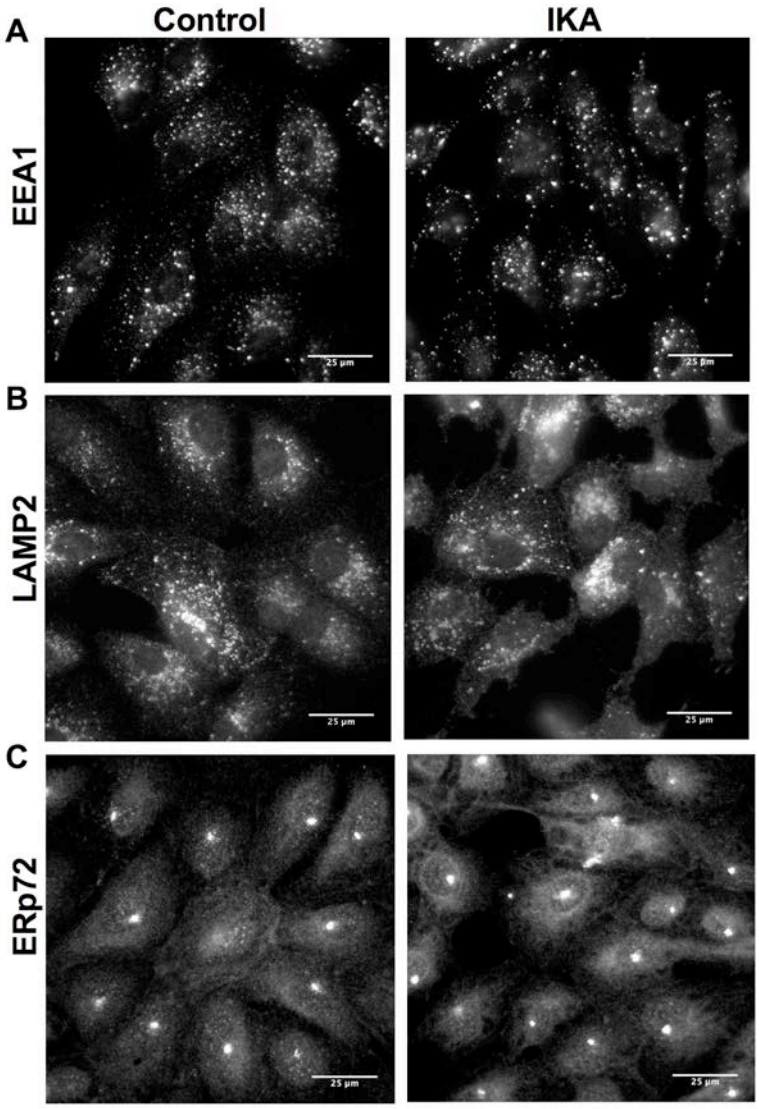

Supplemental Figure 2: Ikarugamycin does not affect the morphology of other cellular organelles. Immunofluorescence of ARPE-19 stably expressing eGFP CLC either pretreated or not (control) with 4 µM IKA for 3 hours and probed with an antibody against A) early endosome antigen 1 (EEA1) B) lysosome-associated membrane protein 2 (LAMP2) or C) endoplasmic reticulum (ER) p72. Scale bar = 25 µm

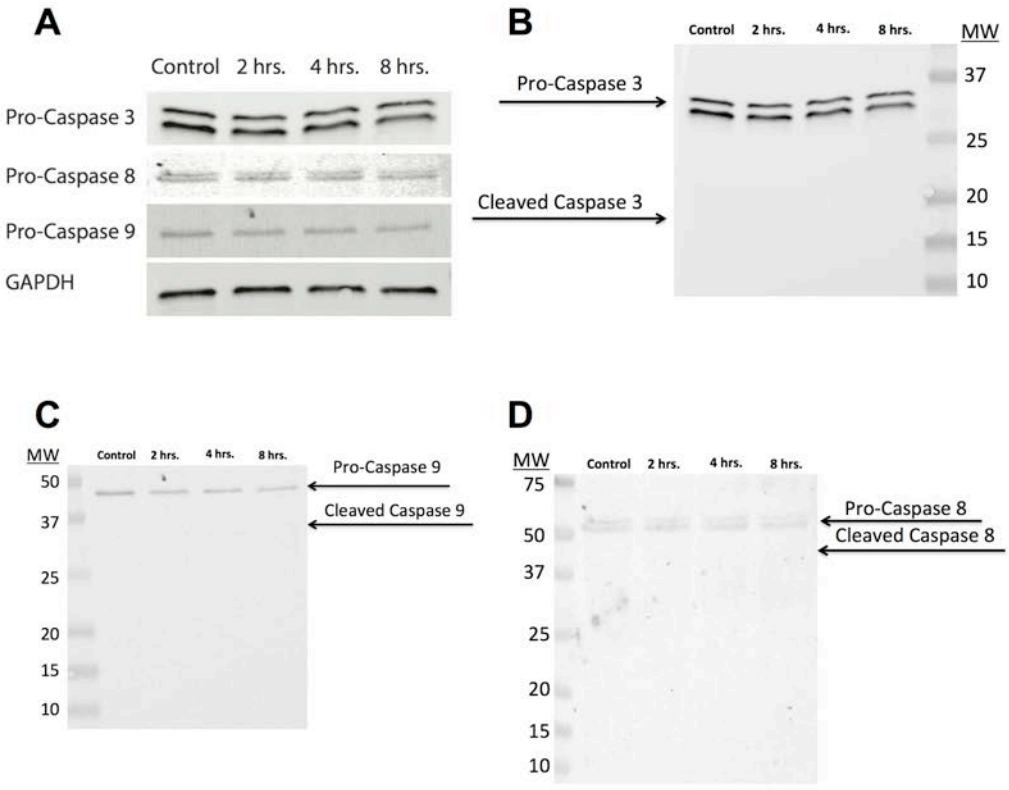

Supplemental Figure 3: Ikarugamycin does not activate Caspase cleavage in cells. A) A representative western blot of pro-caspase 3, 8, and 9 after 2, 4, or 8 hour treatment with 4 μM IKA in ARPE-19 cells. Representative images indicating no cleavage of B) Caspase 3, C) Caspase 9, and D) Caspase 8. Arrows indicate the molecular weight of the cleaved caspase product. All experiments represent (n=3, Avg ± SD).

CHAPTER THREE
A Systematic Analysis Reveals Heterogeneous Changes in the Endocytic Activities of Cancer Cells.

ADAPTED FROM ELKIN, S. R., N. BENDRIS, C. R. REIS, Y. ZHOU, Y. XIE, K. E. HUFFMAN, J. D. MINNA AND S. L. SCHMID (2015). "A SYSTEMATIC ANALYSIS REVEALS HETEROGENEOUS CHANGES IN THE ENDOCYTIC ACTIVITIES OF CANCER CELLS." CANCER RES 75(21): 4640-4650.

Abstract

Metastasis is a multistep process requiring cancer cell signaling, invasion, migration, survival, and proliferation. These processes require dynamic modulation of cell surface proteins by endocytosis. Given this functional connection, it has been suggested that endocytosis is dysregulated in cancer. To test this, we developed In-Cell ELISA assays to measure three different endocytic pathways: clathrin-mediated endocytosis, caveolae-mediated endocytosis, and clathrin-independent endocytosis and compared these activities using two different syngeneic models for normal and oncogene-transformed human lung epithelial cells. We found that all endocytic activities were reduced in the transformed versus normal counterparts. However, when we screened 29 independently isolated non–small cell lung cancer (NSCLC) cell lines to determine whether these changes were systematic, we observed significant heterogeneity. Nonetheless, using hierarchical clustering based on their combined endocytic properties, we identified two phenotypically distinct clusters of NSCLCs. One co-clustered with mutations in KRAS, a mesenchymal phenotype, increased

invasion through collagen and decreased growth in soft agar, whereas the second was enriched in cells with an epithelial phenotype. Interestingly, the two clusters also differed significantly in clathrin-independent internalization and surface expression of CD44 and CD59. Taken together, our results suggest that endocytotic alterations in cancer cells that affect cell surface expression of critical molecules have a significant influence on cancer-relevant phenotypes, with potential implications for interventions to control cancer by modulating endocytic dynamics.

Introduction

Tumor cell growth and metastasis involve changes in cell–cell and cell–matrix interactions, survival and proliferative signaling, and nutrient uptake, all of which depend on plasma membrane receptors and transporters [113, 114]. Signaling from the cell surface and the interactions of cells with each other and their environment are dynamically regulated by the endocytosis of signaling, adhesion, and nutrient receptors. Consequently, it has been suggested that endocytosis is dysregulated in cancer cells [12, 115, 116]. Indeed, there are numerous examples of cancer-specific mutations in components of the endocytic machinery and/or changes in their levels of expression [55-57, 59, 79]. It has also been reported that endocytic trafficking can be perturbed downstream of oncogenes such as p53 and Ras [117, 118].

Clathrin-mediated endocytosis (CME) and caveolae-mediated endocytosis (CavME) remain the best-characterized endocytic pathways, although other more recently discovered and mechanistically distinct pathways have been shown to mediate the uptake of different subsets of signaling, adhesion, and nutrient receptors, as well as regulate the surface expression of membrane transporters [18, 44, 60]. These alternate pathways, generally referred to as clathrin-independent endocytosis (CIE), include the recently discovered clathrin- and dynamin-2 (Dyn2)-independent uptake into so-called clathrin-independent carriers (CLIC), which involve the small GTPases Rac1, Cdc42, and Arf6 [6, 18, 45, 60, 119]. To what extent these CIE pathways contribute to the endocytic capacity of the cell remains unclear, as some studies suggest they are the major pathway for bulk uptake [6], whereas a more recent study suggests that CME can account for virtually all bulk uptake [47].

Past studies of endocytosis in cancer cells have focused primarily on CME and CavME, and these have been studied, individually, in only a few cancer cell lines. Hence, it is unknown whether endocytic activities are selectively or randomly altered in cancers. Moreover, few studies have correlated the activities of specific endocytic pathways with changes in cellular behavior such as migration, adhesiveness, or proliferation. To address these issues, we have systematically and quantitatively analyzed multiple endocytic activities across a clinically diverse and molecularly characterized panel of non–small cell lung cancer (NSCLC) cell lines [120, 121]. Our studies reveal significant heterogeneity across cell lines

and endocytic pathways, which we utilize to test for correlations between specific endocytic activities and alterations in cellular processes related to cancer, including proliferation, adhesion, and migration.

Materials and Methods

Cell lines and culture

HBEC30KT and the NSCLC cancer cell lines were generated as previously described [121]. HBEC3KT and their oncogene-transformed derivatives were developed by the Minna lab [122]. All NSCLC lines used in this study were obtained from the Hamon Cancer Center Collection (UT Southwestern Medical Center) and maintained in RPMI-1640 (Life Technologies) supplemented with 5% FCS at 37°C in a humidified atmosphere containing 5% CO2 and 95% air. All cell lines have been DNA fingerprinted using the PowerPlex 1.2 Kit (Promega) and are mycoplasma free using the e-Myco Kit (Boca Scientific). Culture media were purchased from Life Technologies. Human bronchial epithelial cell (HBEC), NSCLC, and Human retinal epithelia ARPE-19 cell lines were obtained from the ATCC and cultivated in complete KSF medium, RPMI-5% FBS (Sigma), or in DMEM/F12-10% FBS, respectively.

Antibodies and reagents

Anti-TfnR (HTR-D65) monoclonal antibody was produced in hybridoma as in [108]. Anti-CHC (sc-12734) and anti–Dyn-2 (sc-64000) antibodies were purchased from Santa Cruz Biotechnology. FITC-conjugated anti-CD44 (G44-26) and anti-CD59 (p282-H19) monoclonal antibodies were obtained from BD Pharmingen. Horseradish peroxidase (HRP)– and AlexaFluor-conjugated antibodies were purchased from Life Technologies. Biotinylated albumin (#A8549), OPD (#P1536), nystatin (#N6261), poly-l-Lysine (#P1536), fibronectin (#F1141), laminin (#L2020), and hyaluronic acid (#H5388) were obtained from Sigma-Aldrich. Rat-tail collagen (#354236) and streptavidin-POD were purchased from BD Biosciences and from Roche, respectively. Fluoromount G and paraformaldehyde (PFA) were purchased from Electron Microscopy Sciences.

Transferrin receptor, albumin, CD44, and CD59 internalization

TfnR, CD44, or CD59 internalizations were performed using receptor-specific mAbs. We used biotinylated albumin to measure Cav-ME. Cells were seeded at a density of 2.8×10^4 cells/well on collagen-coated 96-well plates and grown overnight. For assays, cells were washed (3× PBS) and incubated with 40 μL PBS^{4+} (PBS supplemented with 1 mmol/L $MgCl_2$, 1 mmol/L $CaCl_2$, 5 mmol/L glucose, and 0.2% BSA) containing 4 μg/mL mAb or 30 μg/mL biotinylated albumin at 37°C for the indicated time points before being immediately cooled to 4°C to arrest internalization and washed to remove unbound ligand (3× PBS). The remaining surface-bound ligand was removed by acid washes (4× 1 minute 0.2 mol/L acetic

acid, 0.2 mol/L NaCl, pH 2). Cells were washed with PBS and then fixed in 4% PFA (Electron Microscopy Sciences) in PBS for 10 minutes at 4°C and 10 minutes at room temperature. Cells were then permeabilized with 0.1% Triton-X100/PBS for 5 minutes, washed, and then blocked with 5% BSA/casein for 1 hour. Internalized albumin was assessed using streptavidin-POD (Roche). Internalized D65, CD44, and CD59 mAbs were assessed using a goat anti-mouse HRP-conjugated antibody and further developed with 200 μL OPD. The reaction was stopped by addition of 50 μL 5 mol/L H_2SO_4. The absorbance was read at 490 nm (Biotek Synergy H1 Hybrid Reader). Well-to-well variability in cell number was accounted for by normalizing the reading at 490 nm with a BCA readout at 560 nm (Biotek Synergy H1 Hybrid Reader). The fraction of internalized ligand was calculated relative to the initial total surface-bound ligand at 4°C (without the acid wash step) measured in parallel for all the assays. Data represent mean ± SD from four independent experiments, each performed in triplicate.

To visualize internalization by fluorescence microscopy, HBEC30KT and HCC4017 cells were seeded in 8-well chambers. The same procedure as for the In Cell ELISA was used to generate "Surface-bound" and "Internalized" ligands except that after permeabilization the cells were incubated with suitable Alexa-Fluor-labeled secondary antibodies and then mounted with Fluoromount G. Images were captured using a 60× objective mounted on a Ti-Eclipse inverted microscope equipped with a CoolSNAP HQ2 monochrome CCD camera (Photometrics).

For siRNA-mediated inhibition of endocytosis, RNAiMAX transfection reagent (Life Technologies) was used to deliver siRNA targeting Dyn2 (1:1 mixture of Dyn2_1: 5′-CCGAAUCAAUCG-CAUCUUCUU-3′ and Dyn2_2: 5′-GACAUGAUCCUGCAGUU-CAUU-3′) or clathrin heavy chain (CHC; [123]) to H1299 cells, following the manufacturer's instructions. We used All Star Negative siRNA as a control. Cells were used 72 hours after siRNA transfection. For inhibition by nystatin, H1299 cells were preincubated in the absence (control) or presence of 25 μg/mL nystatin for 30 minutes at 37°C before internalization assays were performed as described above except the PBS^{4+} contained nystatin.

Proliferation, adhesion assays, and 3D migration assays

The following microscopy-based assays were performed in 96-well black plates with clear bottom (PerkinElmer #600525).

Proliferation

A total of 2,000 cells/well of each cell line were dispensed, in triplicate. Five hours after plating, cells from the first plate—"Day 0" plate—were fixed with 4% PFA and stored at 4°C. The same operation was repeated on days 1 through 5. Cell nuclei were stained for 30 minutes with 10 μg/mL Hoechst/PBS solution. Cell proliferation was expressed as the ratio of cell counts on "Day 5"/"Day 0" plates.

Adhesion

96-well plates were incubated with 40 µL/well for 1 hour containing 10 µg/mL BSA, 0.01% poly-l-Lysine, 50 µg/mL rat tail collagen, 10 µg/mL fibronectin, 50 µg/mL laminin or incubated overnight with 1 µg/mL hyaluronic acid. After plates were washed with PBS, 15,000 cells/well were plated and allowed to adhere for 30 minutes at 37°C. Floating cells were then removed by three washes with PBS. Cells were fixed with 4% PFA and nuclei were stained for 30 minutes with 10 µg/mL Hoechst/PBS solution. Cell adhesion represents the number of cells per condition.

3D migration assay

Assays were performed using 1 µg/mL bovine collagen and 2.5% FBS as chemoattractant, following the experimental procedure described in [124]. Microscopy images of nuclear staining were taken at 50 µm steps from 0 to 150 µm into the collagen plug. Invasion index was calculated as the sum of cell counts at 50, 100, and 150 µm over cell counts at 0 µm.

Cell nuclei were visualized using a 20× (migration assays) or 10× (proliferation and adhesion assays) air objective mounted on a Ti-Eclipse inverted microscope (Nikon) driven by NIS Elements V4.13 software and quantified using the "Object Count" feature of NIS Elements software.

Growth in soft agar

Anchorage-independent growth in soft agar was performed by seeding cells in 0.4% noble agar on top of a 1% layer. After 3 weeks, cell foci were stained with a Crystal Violet solution and extensively washed with water to remove excess stain. Foci were then counted manually using the Cell Counter tool on ImageJ software.

Statistical analysis and hierarchical clustering

A hierarchical clustering algorithm [125] was used to group the 29 NSCLC cell lines based on their collective endocytic activities. For this purpose, we took the averaged endocytic activity across replicates for each cell line and each pathway (Supplementary Table S1), and then used these values to calculate Pearson correlation distance metrics, average linkages [125], and then generated the hierarchical clustering results using GENE-E software from GenePattern [126] with default settings. The hierarchical tree identified two clusters. We tested the significance of the clustering result using the R package sigclust by using the 2-means clustering index as a statistic to test the null hypothesis that a group of samples is from a single Gaussian distribution (28). Migration and growth in soft-agar enrichment analysis for two clusters were measured by the Fisher exact test to examine whether the two kinds of classification from categorical data are associated, which is best suited for small sample sizes and a 2×2 contingency table. We tested association of the two clusters with endocytic activities and the total surface protein expression using a Wilcoxon rank sum test, which compares the sums of ranks and is more robust to the presence of outliers. The

statistical correlations between each endocytic activity and cell proliferation were calculated by the Spearman rank correlation test, which is less sensitive to outliers and queries the extent of dependence of one ranked variable on another. Correlations between KRAS mutations and endocytic activities were also measured by the Wilcoxon rank sum test.

Results

Choice of pathway-specific and lung cancer–related endocytic markers

CME and CavME have been extensively studied, and specific markers allowing the quantification of these endocytic routes are well described. We chose transferrin receptor (TfnR) for CME [127] and albumin, which binds to gp60 and is internalized by CavME [128]. Although markers for clathrin- and caveolae-independent endocytotic pathways are less well characterized, glycophosphatidylinositol-anchored proteins (GPI-AP) are reportedly internalized by these routes [6, 60, 119]. For our studies, we chose complement lysis restricting factor/CD59 [129], a GPI-AP that is involved in cellular processes critical to lung cancer cell survival and internalized via CIE [130, 131]. Recent studies have identified the transmembrane glycoprotein, CD44, which is a hyaluronic acid receptor, as a cargo molecule specifically internalized by CLICs and recycled via GPI-enriched endocytic compartments (GEEC; [60, 132]). CD44 becomes more concentrated in flotillin-low or non-raft fractions, presumably corresponding to CLICs, in migrating breast cancer cells [133]. Interestingly,

CD44 is expressed in NSCLC, but not in small cell lung cancer [134]. Elevated expression levels of CD44 combined with low expression of CD24 ($CD44^{high}/CD24^{low}$) is an emergent prognosis tool in the clinic as it is associated with "stemness" features of cancer cells in vivo and in vitro [134-136]. Together, these markers allowed us to directly measure the CME, CavME, and CIE activities in NSCLC cells.

Development of pathway-specific 96-well endocytosis assays

To efficiently and systematically measure multiple endocytic pathways using several NSCLC cell lines in parallel, we developed a new sensitive and quantitative method using 96-well plates, referred to as an In-Cell ELISA (see Materials and Methods). As ARPE-19 cells have been routinely used to study CME, we used this cell line to set up and validate the highthroughput assay. Upon incubation of ARPE-19 cells at 37°C with the anti-transferrin receptor antibody HTR.D65 (D65; [137]), we could detect the time and temperature-dependent accumulation (expressed as the fraction internalized at 37°C over the total surface bound at 4°C) of intracellular D65 (Supplementary Fig. S1A, left, quantification in B). The use of the bivalent anti-TfnR mAb, rather than transferrin, as ligand reduces rapid recycling [138] and enables us to focus our measurements on initial rates of internalization. As a negative control for internalization of surface-bound versus soluble mAb, we incubated these cells with a specific antibody against the T-cell marker CD8, which is not expressed on

epithelial cells. As expected, we did not detect surface binding or any internalization of anti-CD8 in APRE-19 cells (Supplementary Fig. S1A, right, quantification in B).

This assay was adapted to measure CavME using biotinylated-albumin as ligand, and CIE using anti-CD59 or anti-CD44 mAbs as markers, and validated in the NSCLC line, H1299. We first confirmed that these different surface receptors utilized different pathways by siRNA knockdown of CHC, which is specifically required for CME and dynamin 2 (Dyn2), which is required for both CME and CavME (Fig. 1A). We also treated cells with the antifungal drug nystatin that disrupts the plasma membrane cholesterol and selectively inhibits CavME, but not CME. As expected, CME of TfnR was inhibited upon RNAi-mediated knockdown of either Dyn2 or CHC (Fig. 1B), whereas nystatin showed no effect. Also, as expected, uptake of albumin by CavME was inhibited upon RNAi knockdown of Dyn2 and treatment with nystatin (Fig. 1C), but was unaffected by CHC knockdown. Finally, uptake of CD44 and CD59 was not affected by either of these perturbations (Fig. 1D and E), confirming that these markers are internalized by a clathrin-, Dyn2-, and caveolae-independent mechanism. These data establish our ability to independently and selectively measure at least three distinct endocytic pathways.

Altered endocytic activity across pathways in isogenic normal and cancer cell lines

We next compared the endocytic activities in an NSCLC cell line (HCC4017) with those in a normal, nontumorigenic HBEC line, HBEC30KT, derived from the same patient.

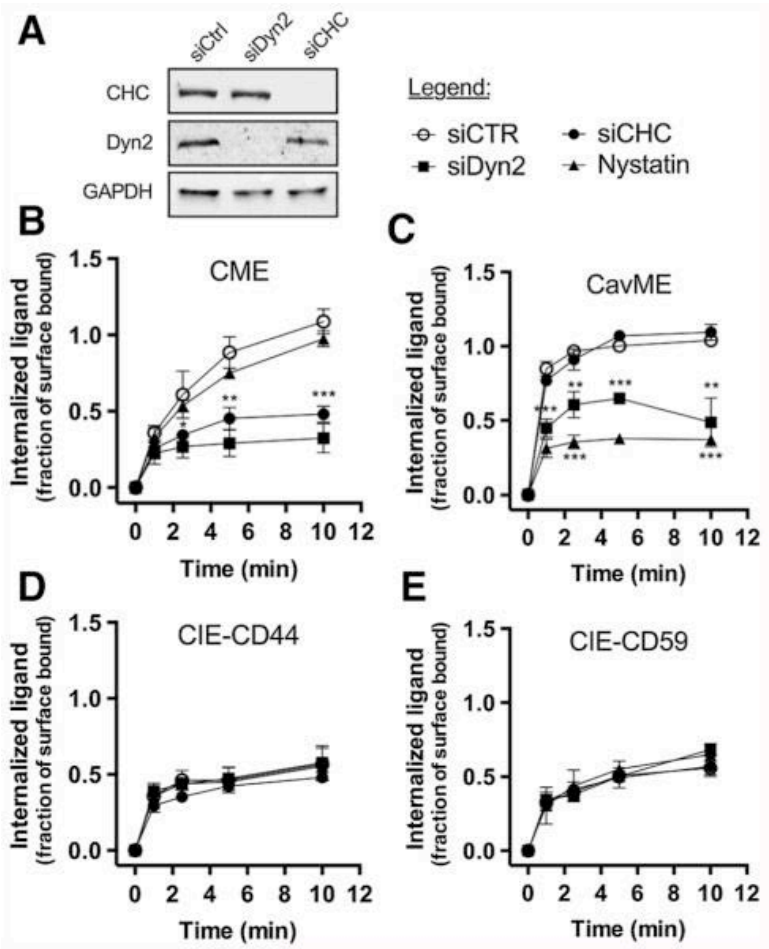

Figure 1: Measuring mechanistically distinct endocytic pathways in NSCLC H1299 cells. H1299 NSCLC cells grown in 96-well plates were incubated with the indicated antibodies or ligands, and the mechanistically distinct endocytic activities were measured using an In-Cell Elisa assay (see Materials and Methods). A, representative Western blot showing efficiency of siRNA-mediated knockdown of CHC or dynamin 2 (Dyn2) measured 72 hours after transfection of H1299 cells. GAPDH was used as a loading control. CME of D65 anti-TfnR mAb (B), CavME of biotinylated albumin (C), CIE of anti-CD44 mAb (D), or anti-CD59 mAb (E) were measured 72 hours after transfection with control (open circle), CHC (closed circle), or Dyn2 (closed square) siRNAs, or 30 minutes after incubation with nystatin (closed triangle). Data are expressed as the fraction of total surface-bound ligand internalized after incubation for the indicated time at 37°C (n = 3 independent experiments, each performed in triplicate ± SD). Two-tailed Student t tests were used to assess statistical significance. * , $P < 0.05$; ** , $P < 0.005$; *** , $P < 0.0005$.

The HBEC30KT cells were immortalized by serial introduction of retroviral expression vectors encoding cyclin-dependent kinase 4 (Cdk4), which prevents premature growth arrest, and human telomerase reverse transcriptase (hTERT), which bypasses telomere-dependent senescence [139]. The internalization rates of all four receptors, expressed as the fraction internalized after 5 minutes at 37°C over the total surface bound at 4°C, were reduced in the NSCLC cells as compared with their normal HBEC30KT counterpart (Fig. 2A). This was confirmed by fluorescence microscopy (Fig. 2B–E), which also illustrates the uniformity in uptake among the cells within each line. These results suggest that endocytosis may indeed be altered in cancer cells.

Malignant transformation of HBEC alters endocytosis

To determine when changes in endocytosis might occur during the transformation process, we obtained normal HBEC3KT cell lines along with their derivatives with the following oncogenetic modifications common to lung cancer: (i) p53 deficiency triggered by stable shRNA-mediated knockdown of p53 (sh-p53), (ii) overexpression of activated KRAS ($KRAS^{V12}$), (iii) both sh-p53 and $KRAS^{V12}$, or (iv) sh-p53, $KRAS^{V12}$, and c-myc overexpression. It had been previously shown that all three oncogenic changes were necessary and sufficient for full oncogenic transformation of HBEC3KT cells as assessed by in vitro anchorage-independent growth and in vivo tumor formation after subcutaneous

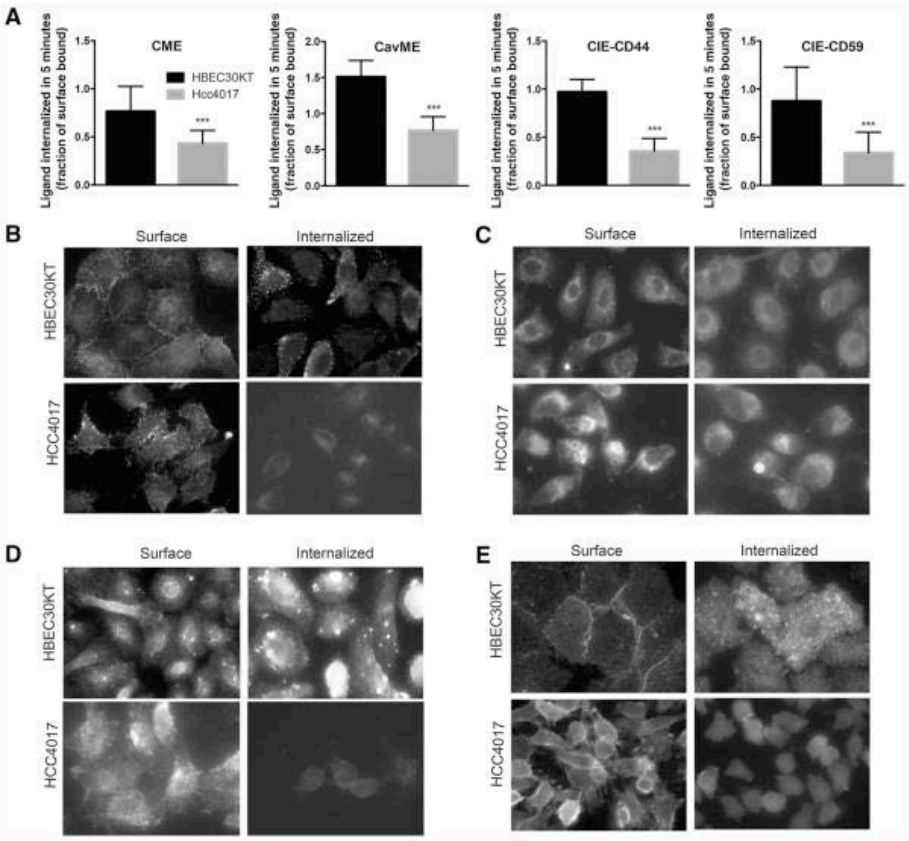

Figure 2: Differential internalization of endocytic markers in matched patient-derived normal HBEC30KT and NSCLC (HCC4017) cells. A, comparison of the extent of internalization after 5 minutes at 37° C via the indicated endocytic pathways in nontumorigenic-HBEC30KT (black bars) and the NSCLC line (HCC4017, gray bars) derived from the same patient. Two-tailed Student t tests were used to assess statistical significance. ***, $P < 0.0005$. B–E, representative fluorescence images of total surface-bound and internalized (after 5 minutes at 37° C) ligands in HBEC30KT and HCC4017 cell lines assayed for CME of D65 anti-TfnR mAb (B), CavME of biotinylated-albumin (C), CIE of anti-CD44 mAb (D), or CIE of anti-CD59 mAb (E).

injection into NOD/SCID mice [122]. Consistent with this, the transfected cells were morphologically indistinguishable from the parent HBEC3KT cells until all three oncogenic mutations were present (Fig. 3A), at which point they adopted a more elongated and irregularly shaped mesenchymal morphology similar to some NSCLC cell lines.

We measured the various endocytic activities in these cells, and consistent with the need for all three changes to induce tumor formation in mice, only the HBEC3KT$^{sh\text{-}p53/KRASV12/c\text{-}myc}$ cell line exhibited decreased rates of uptake of all four markers (Fig. 3B). Interestingly, the different endocytic pathways were differentially affected during the transformation process. For example, whereas the rate of CavME did not significantly decrease until all three oncogenic changes were introduced, CME decreased linearly with each oncogenic modification. CD44 and CD59 uptake, both thought to report CIE, also respond differently to the oncogenic changes. Introduction of the KRAS^{V12} mutant was sufficient to decrease CD59-CIE activity to its lowest levels, whereas CD44-CIE activity was unaffected by expression of KRAS^{V12} alone, but was progressively reduced with the addition of sh-p53 and myc. Together, these data provide additional support that our assays measure distinct endocytic processes and establish that the different endocytic pathways can be differentially sensitive to oncogenic changes. Importantly, as we had observed in comparing patient-matched normal HBEK30KT cells with HCC4017 NSCLC tumor-derived cells (Fig. 2), we again found that full oncogenic transformation of otherwise syngeneic HBEK3KT cells resulted in decreased rates of all endocytic activities measured.

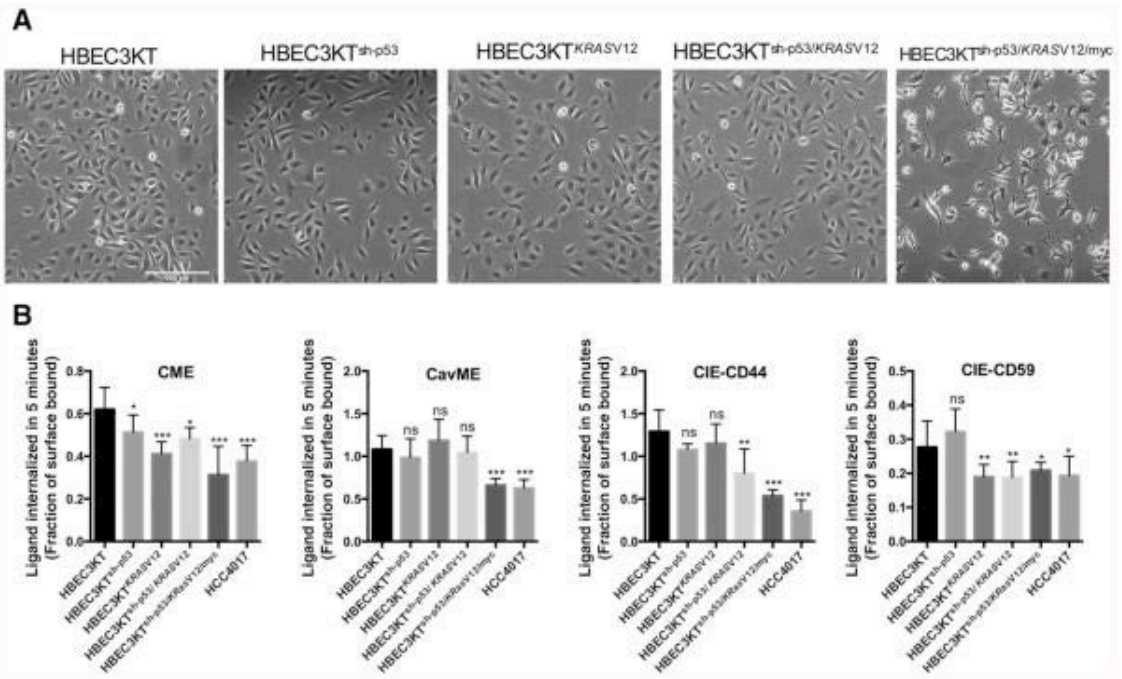

Figure 3: Changes in endocytic activity accompany progressive oncogenic transformation of HBEC3KT cells. A, phase contrast images of nontumorigenic HBEC3KT cells and the same cells transformed by sh-p53 knockdown and/or mutant $KRAS^{V12}$ and c-myc overexpression, as indicated. Morphologic changes relative to the parent HBEC3KT cells are only apparent when all three oncogenic transformations have been introduced. B, comparison of internalization via CME, CavME, and CIE in nontumorigenic HBEC3KT, $HBEC3KT^{sh\text{-}p53}$, $HBEC3KT^{KRASV12}$, $HBEC3KT^{sh\text{-}p53/KRASV12}$, and $HBECK3KT^{sh\text{-}p53/KRASV12/c\text{-}myc}$ cells. Rates of internalization in HCC4017 NSCLC cells, from , are also shown for comparison. Data shown are average values for the fraction of surface-bound ligand internalized after 5 minutes at 37° C for three independent experiments, each performed in triplicate. Two-tailed Student t tests were used to assess statistical significance compared with the parent HBEC3KT (ns, not significant; * , $P < 0.05$; ** , $P < 0.005$; *** , $P < 0.0005$).

Systematic analysis of CME, CavME, and CIE in 29 NSCLC cell lines

To determine whether there are indeed systematic changes in endocytic activities associated with NSCLC, we measured the rates of uptake for all four endocytic pathways in NSCLC cell lines derived from 29 patients. These cell lines were chosen for their diverse molecular and clinical status (e.g., isolated from the primary tumor vs. metastases). All assays were performed in quadruplicate over multiple days with H1299 used as an internal control for each experiment (see Materials and Methods). The data, which are summarized in Supplementary Table S1 (avg. ± SD, n = 4 for each pathway in each cell line) and presented in Fig. 4A, show that the four endocytic activities varied significantly across all NSCLC lines. This variability cannot be attributed to differences in surface expression of the four molecular markers, as the rates of uptake did not correlate with changes in surface expression of receptors (Supplementary Fig. S2). For comparison, the rates of uptake determined in normal HBEC30KT and HBEC3KT cells were plotted as solid squares and triangles, respectively (Fig. 4). As shown with the isogenic pairs (Figs. 2 and 3), the majority of NSCLC cell lines have lower rates of uptake across all four pathways compared with the nontransformed HBEC lines; however, several NSCLC cell lines had equal or higher rates of endocytosis especially in the CD44-CIE pathway, which exhibited the greatest cell-to-cell variability. Thus, although our analyses of isogenic normal and NSCLC lines showed a consistent and significant decrease in activity across all endocytic pathways, we find considerable heterogeneity in endocytic activities across a diverse panel of NSCLC cell lines.

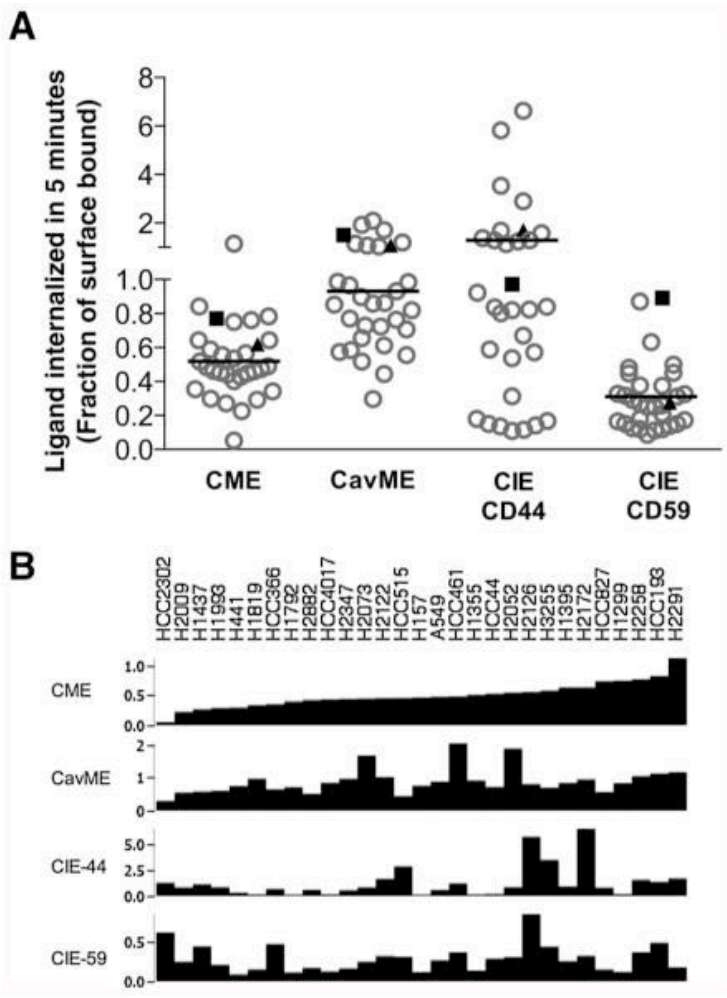

Figure 4: Summary of data for the activities of four distinct endocytic pathways in 29 NSCLC cell lines. A, mechanistically distinct endocytic activities were measured in 29 NSCLC cell lines, as described in . Each data point represents the average endocytic activity (n = 4 independent experiments, each performed in triplicate) for a different cell line. The closed square and triangle represent the internalization rate of normal, HBEC30KT, and HBEK3KT cells, respectively. B, the 29 cell lines were ordered from low to high CME of Tfn (top), and the other endocytic activities for each cell line are shown in the three bottom plots. Although the extent of CIE of CD44 and CD59 was related, neither CIE nor CavME covaried with CME activity.

Given this heterogeneity, we asked whether changes in internalization rates occurred randomly across the different endocytic routes, or if they positively or negatively correlated with one or more pathways. For this comparison, we ordered the 29 NSCLC cell lines from low to high, based on their rates of TfnR uptake and compared these rates to those measured for other pathways (Fig. 4B). We were unable to detect any correlation between CME or CavME and the other endocytic pathways. As expected, a similar pattern emerged when comparing the rate of uptake of the two CIE markers, CD44 and CD59. However, consistent with their differential response to the introduction of oncogenic changes (Fig. 3B), clear, quantitative differences were also detected. Thus, these four pathways appear to be differentially regulated in cancer cells.

Correlation of endocytic activities with cancer-related properties of NSCLC cell lines

Given the differential effects of loss of p53 in combination with overexpression of $KRAS^{V12}$ and/or c-myc on endocytosis in HBEC3KT cells and their derivatives (Fig. 3B), we next extracted information regarding the status of these three oncogenes for the 29 NSCLC cell lines from existing databases (Fig. 5A; [140-142]). We wondered whether these oncogenic changes might correlate with their measured endocytic activities. The majority of the cell lines had functional mutations in p53, whereas only about half had functional mutations in KRAS, and only 5 had increased expression of c-myc. In contrast with the results obtained with syngeneic cell lines, the three NSCLC lines exhibiting all three

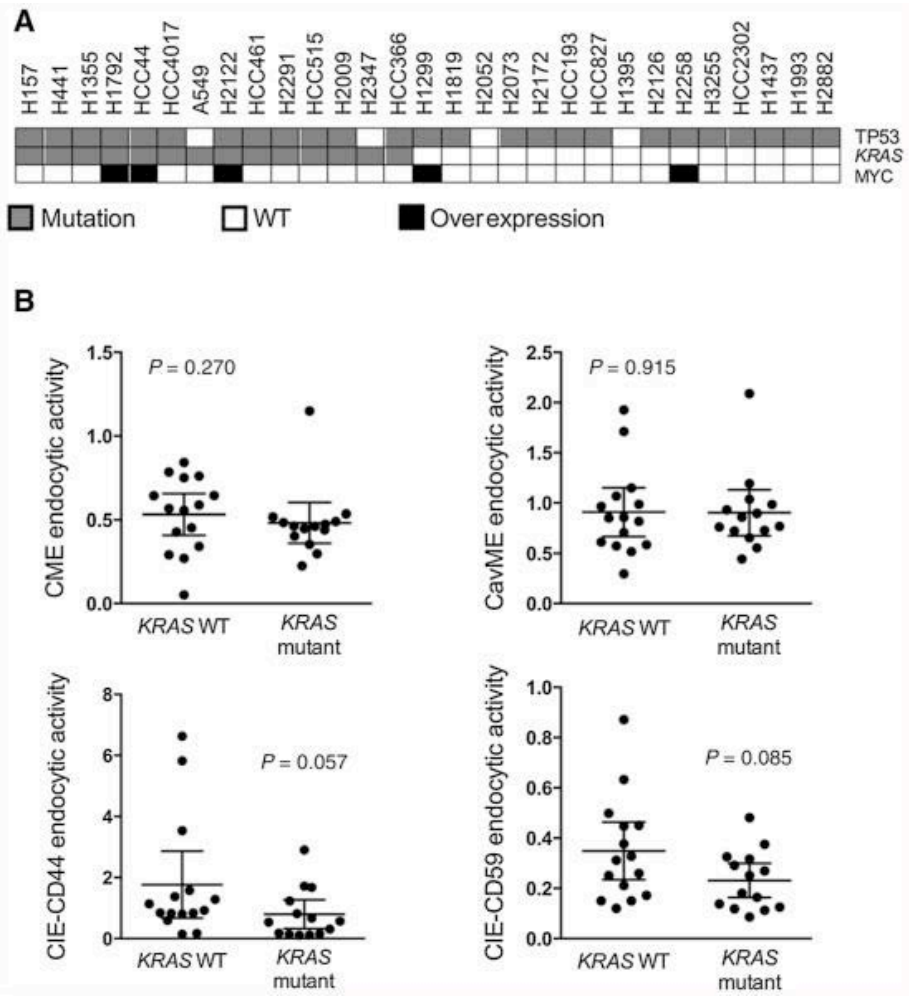

Figure 5: Relationship between endocytic activity and genetic alteration associated with cancer cell oncogenic transformation. A) the mutation status of p53 and KRAS and overexpression status of MYC in the 29 NSCLC cell lines, as derived from [140]. B) correlation between KRAS mutation status and endocytic activity in all four pathways. Wilcoxon rank sum tests were used to assess statistical significance, as indicated.

oncogenic changes (H1792, Hcc44, and H2122) did not exhibit the lowest levels of endocytic activity for any of the pathways (see Supplementary Table S1). Indeed, there was no correlation between changes in activity of any of the endocytic pathways with p53 mutations or c-myc overexpression (Supplementary Fig. S3A and S3B). We could detect a small, but significant ($P < 0.1$, Wilcoxon rank sum test) correlation between KRAS mutations and a decrease in endocytic activity of both CIE pathways (Fig. 5B); however, there was no significant correlation between KRAS mutations and CME or CavME. Thus, we were unable to detect systematic changes in endocytic activity corresponding to specific oncogenic changes in our panel of NSCLC cell lines.

Several studies on individual cell lines have suggested roles for CME, CavME, and CIE in cancer progression [12, 55, 57, 59, 79, 143, 144]. Therefore, we next asked whether the heterogeneity observed in pathway-specific internalization rates might relate to differential activities of the 29 cell lines assessed in a panel of in vitro cancer-relevant assays. For this purpose, we established 96-well assays to measure the following cellular processes (see Materials and Methods): (i) 3D migration through a collagen matrix; (ii) adhesion to different substrates (collagen, fibronectin, laminin, and hyaluronic acid); (iii) proliferation; and (iv) growth in soft agar. Once again we observed significant heterogeneity in these activities across the different NSCLC lines (Supplementary Table S2). We applied the Spearman rank correlation test to determine whether differences in individual endocytic activities correlated with changes in any of the above properties. We detected a significant

negative correlation between proliferation and CIE pathway activity that was not seen for CME or CavME (Supplementary Fig. S4). However, we saw no significant correlations between 3D migration, adhesion or growth in soft agar, and changes in any of the four individual endocytic activities (Supplementary Figs. S5 and S6A). However, adhesion on one substrate was correlated with adhesion on another by Pairwise Pearson correlation comparison (Supplementary Fig. S6B), providing evidence for the validity of our measurements and demonstrating that the adhesion properties of these cells are not substrate specific.

Hierarchical clustering based on endocytic activities reflects cancer-related properties

Previous studies have used hierarchical clustering analyses to classify NSCLCs based on histologic [145], transcriptional [146], and genetic differences [147]. To gain more insight into cancer cell properties that might be linked to their endocytic activities, we took a similar approach and conducted unsupervised hierarchical clustering analysis [125] of all 29 cell lines based on Pearson correlation distance metrics and average linkage of their measured endocytic activities using the raw data presented in Supplementary Table S1 (see Materials and Methods). Hierarchical clustering based on the functional criteria of their collective endocytic behaviors identified two clusters (Fig. 6A). The significance of the clustering result ($P = 0.0037$) was tested using the R package sigclust [123]. Whereas individual endocytic

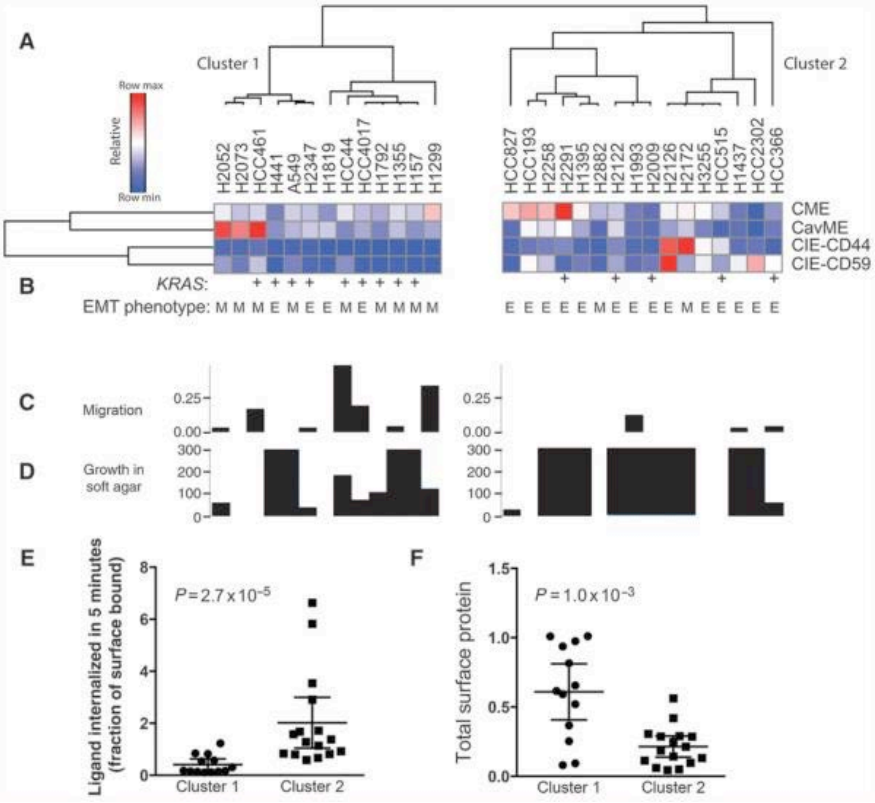

Figure 6: Endocytic activities identify two phenotypically distinct clusters of NSCLC cell lines. A) the 29 NSCLC cell lines clustered into two distinct groups after unsupervised learning based on endocytic activity in all four pathways. B) NSCLC cell lines in cluster 1 were enriched in those bearing KRAS mutations (+) and exhibiting a mesenchymal phenotype (M), whereas cells in cluster 2 were enriched in those exhibiting an epithelial phenotype (E). C) invasion ratio for each cell line was measured as the fraction of cells migrating up through a collagen matrix toward serum (see Materials and Methods). D) rate of growth in soft agar reported as colonies/well (see Materials and Methods). Each bar represents the average activity (n = 3 independent experiments, each performed in triplicate) for each cell line indicated and clustered in A. E) and F) comparison of the extent of internalization of CD44 through CIE after 5 minutes at 37° C (E) and total surface binding of CD44 measured at 4° C in cluster 1 and cluster 2 (F). Wilcoxon rank sum tests were used to assess statistical significance, as indicated. clusters. Together, these data suggest that selective changes in endocytic activities, in particular clathrin-independent endocytosis, can dynamically alter surface expression of cancer-related molecules and affect cellular processes that contribute to cancer aggressiveness. However, such changes do not appear to occur systematically across endocytic pathways or in all NSCLC cells. Further studies will be needed to determine whether these changes affect clinical outcomes.

activities did not appear to correlate with other cancer cell properties, we were able to detect significant differences in cancer cell properties between the two clusters derived from analysis of their collective endocytic activities. Cluster 1 was enriched in NSCLC cell lines that expressed mutant KRAS (Fig. 6B) and mesenchymal cell lines based on a published 76 gene signature [148], whereas cluster 2 was enriched in NSCLC cell lines classified, based on their gene signature, as epithelial ($P = 0.02$, Fisher exact test).

NSCLC cells in the two clusters also differed in their ability to migrate through collagen and their growth in soft agar. Cluster 1 exhibited a greater ability to migrate through collagen as compared with cluster 2 (Fig. 6C, $P = 0.0641$, Fisher exact test as assessed by categorical correlation for migratory or nonmigratory behavior of the two clusters). However, the majority of NSCLC cell lines (54% of cluster 1 and 81% of cluster 2) failed to migrate under these conditions; thus, it is possible that other assays for cell migration might reveal more significant differences. Cluster 1 also appeared to less effectively grow in soft agar as compared with cluster 2 (Fig. 6D, $P = 0.117$). That this apparent difference did not reach statistical significance may be due to the qualitative nature of the assay and its saturation at ≥300 colonies/well. Consistent with this, only 31% of cluster 1 cell lines compared with 62% of cluster 2 cell lines exhibited high growth (i.e., at >300 colonies/well) in soft agar ($P = .079$, two-sided Student t test). Together, these studies suggest that clustering of NSCLC cells based on functional criteria may be informative as to cancer cell properties. Clearly higher numbers of cell lines will need to be examined to confirm these associations.

A recent study has suggested a link between CD44 expression and KRAS-driven lung adenocarcinomas [149]. Given our finding of the small but significant correlation between CD44 endocytosis and KRAS mutations (Fig. 5), the negative correlation between CD44 endocytosis and proliferation in 2D (Supplementary Fig. S4), and the apparent differences in proliferation on soft agar between clusters 1 and 2, we more closely examined uptake and surface expression of CD44 in the two clusters. We found that cluster 1 had significantly lower clathrin-independent endocytic activity and correspondingly higher surface expression of both CD44 (Fig. 6E and F) and CD59 (Supplementary Fig. S7A). In contrast, we did not detect systematic or significant differences in the other endocytic activities or changes in surface expression of their markers (Supplementary Fig. S7B and S7C) between the two clusters. Together, these data suggest that selective changes in endocytic activities, in particular clathrin-independent endocytosis, can dynamically alter surface expression of cancer-related molecules and affect cellular processes that contribute to cancer aggressiveness. However, such changes do not appear to occur systematically across endocytic pathways or in all NSCLC cells. Further studies will be needed to determine whether these changes affect clinical outcomes.

Discussion

Endocytosis of cell surface receptors can potentially control many activities related to cancer cell proliferation and migration, including nutrient acquisition, cell–cell and cell–matrix adhesion, receptor tyrosine kinase, and G-protein–coupled receptor signaling. Moreover, many components of the endocytic machinery are mutated or have altered expression in a number of cancers [12, 116, 150]. Thus, it is generally assumed that endocytosis is somehow altered in cancer cells to enhance their proliferative and metastatic potential. Evidence in support of this concept derives primarily from analysis of the effects of perturbing specific endocytic pathways on signaling, proliferation, and/or migration in cancer cells [55, 59, 79, 143]. Here, we sought additional support for this hypothesis through a more systematic and quantitative analysis of the endocytic activities of a large panel of NSCLC cell lines to determine whether there were consistent alterations in one or more endocytic pathway that might be linked to changes in cancer cell proliferation, including anchorage-independency, adhesion, or migration through a collagen matrix. We measured the uptake of four ligands via mechanistically distinct endocytic pathways in 29 independently isolated NSCLC cell lines and discovered a large degree of heterogeneity in these activities. Our results emphasize the inherent complexity and heterogeneity in cancer cell biology that can preclude drawing general conclusions from acute perturbation studies in single cell lines. Nonetheless, based on their overall endocytic properties, we could identify two phenotypically distinct clusters of NSCLC cell lines, which differed in their preponderance of KRAS mutations, epithelial or mesenchymal gene signatures, 3D migration, and

anchorage-independent growth. These data suggest that changes in overall endocytic capacity might indeed influence cancer cell behavior and/or vice versa.

Heterogeneity in NSCLC cell lines confirms diversity of endocytic pathways

The functions and activities of different endocytic pathways are frequently measured after selective perturbation of one or other pathway. However, the effects of these perturbations can partially overlap making it difficult to distinguish endocytic pathways, especially in the case of the less well-defined clathrin-independent mechanisms. Indeed, the relationship between CLIC-mediated uptake of CD44 and GPI-anchored proteins and the arf6-dependent uptake of similar markers remains somewhat controversial [52, 59, 60, 130, 151]. Adding to this complexity, it has been suggested that there might be cross-talk between endocytic pathways, such that inhibition of one might lead to upregulation of another. Such a reciprocal relationship has been recently suggested for CavME and CD44 uptake [152]. Finally, a recent study suggested that CME accounts for >95% of all bulk endocytosis, including that of the GPI-AP, CD59 [47], and brought into question the physiologic relevance of alternate endocytic pathways. Our finding that at least three distinct endocytic pathways can be differentially up- or downregulated in an otherwise non-perturbed panel of NSCLC lines confirms that these pathways, including two poorly defined clathrin-independent pathways mediating the uptake of CD59 and CD44, respectively, can be differentially regulated and hence must be, at least in part, mechanistically independent.

Endocytosis and cancer

Unexpectedly, we observed a decrease in all endocytic pathways measured when we compared syngeneic normal HBEC cell lines with their tumorigenic counterparts. Having lower rates of endocytosis might benefit the NSCLC cell lines by maintaining higher surface levels of important plasma membrane molecules, including those for signaling and adhesion. However, this pattern did not hold across all NSCLC lines, highlighting the genetic and mechanistic diversity of cancer. Moreover, it is likely that endocytic activities of cancer cells will be influenced by different signaling environments in vitro and in vivo.

Previous work using siRNA knockdown of components of the endocytic machinery had suggested a link between CME and CavME and the ability of cancer cells to proliferate, adhere, and migrate. CME has been implicated in integrin [143] and receptor tyrosine kinases [153] endocytosis. In order for a cell to sustain directed forward migration, integrins and receptor tyrosine kinases, such as the EGFR, must be constantly internalized by CME and recycled to the leading edge of the cell. CavME has also been found to be important for the internalization of membrane-type 1 matrix metalloproteinase, which helps to degrade the ECM at the leading edge of a cell [75], as well as integrins [77] contributing to the disassembly of focal adhesions. Correspondingly, knockdown of Dyn2 in prostate cancer cells prevented cell invasion in 3D and in vivo [79], and siRNA knockdown of Cav1 in NCI-H460 lung cancer cells causes an increased ability of these cells to migrate and invade in

vitro [55]. Thus, we were surprised to see no correlation between CME or CavME endocytic activity and these cancer cell processes. This difference likely reflects the effects of strong perturbation of these pathways as compared with the more subtle regulation and variations we observe in our panel of NSCLC cell lines. It is also possible that rather than global changes in CME and CavME, changes in the endocytosis of specific cargo molecules not used here to measure these pathways could be selectively altered to affect migration, proliferation, and/or adhesion. For example, we detected an inverse relationship between CIE of CD44 and proliferation in 2D that was less evident when measuring CIE of CD59.

Better classification of NSCLCs would facilitate the diagnosis and treatment plans for individual patients. Numerous studies have applied unsupervised clustering methods to classify NSCLC cell lines based on their diverse patterns of mRNA or protein expression, epigenetic modifications, etc. [145-147]. Here, for the first time, we apply this analysis to their measured diversity in a cell biological activity, endocytosis. Interestingly, despite our inability to correlate differences in individual endocytic activities with other cancer-related cellular properties (e.g., migration, adhesion, proliferation), hierarchical clustering based on the diversity of their collective endocytic activities identified two distinct NSCLC cell line clusters that co-cluster with other cancer-related properties. Cluster 1 appeared enriched in cell lines bearing KRAS mutations, a mesenchymal phenotype, an enhanced ability to migrate in collagen, reduced ability to grow in soft agar, and reduced CIE, in particular of CD44, leading its increased expression on the cell surface. Consistent with these findings,

recent studies reported a role for CD44 in mediating NSCLC proliferation downstream of KRAS [149]. It will be important to extend these analyses to other NCSLC cells to test the validity of these linkages and also to determine their functional and/or clinical relevance. Moreover, applying this approach to other NCSLC lines will enhance our statistical power and allow us to assess the functional significance of the "outliers" we detect among this initial sampling of 29 cell lines.

Further work is necessary to directly explore the role and regulation of endocytosis in cancer progression. That many components of the endocytic machinery are dysregulated or mutated in cancer suggests a functional link. Our results suggest that dynamic regulation of the surface expression of important cancer molecules through endocytosis may, in some cases, contribute to the malignant properties of cancer cells. However, they also highlight cancer cell heterogeneity and reveal that the functional relationship between endocytic activities and cell migration, adhesion, and proliferation may be more complex than suggested by perturbation analyses of single cell lines.

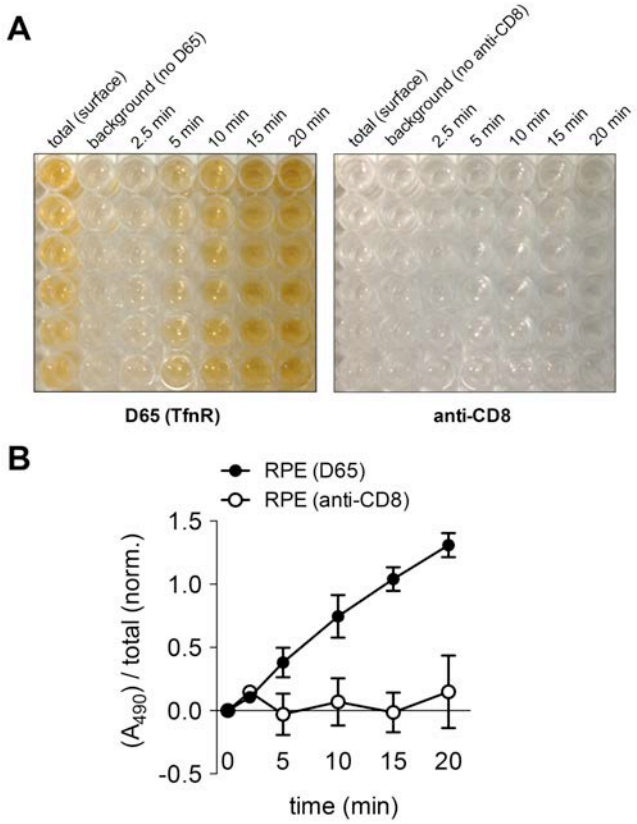

Supplemental Figure 1: TfnR and CD8 internalization as measured by In-Cell ELISA. **A**) Representative images of D65 and anti-CD8 treated ARPE-19 cells, incubated for different time points (0-20 min), after adding the respective secondary-HRP conjugated antibodies and developing and stopping reagents. Total surface bound D65 (total) and background (acid washed cells) was used to calculate the relative percentage of TfnR and CD8 internalization. **B**) Continuous internalization of TfnR and CD8 in ARPE-19 cells. The rate of uptake of TfnR and CD8 was measured using the anti-transferrin receptor antibody HTR.D65 and a specific anti-CD8 antibody, respectively. Percentage of TfnR and CD8 uptake was calculated relative to the initial total surface bound ligand at 4^{o}C (n=3). Data represents mean +/- SD.

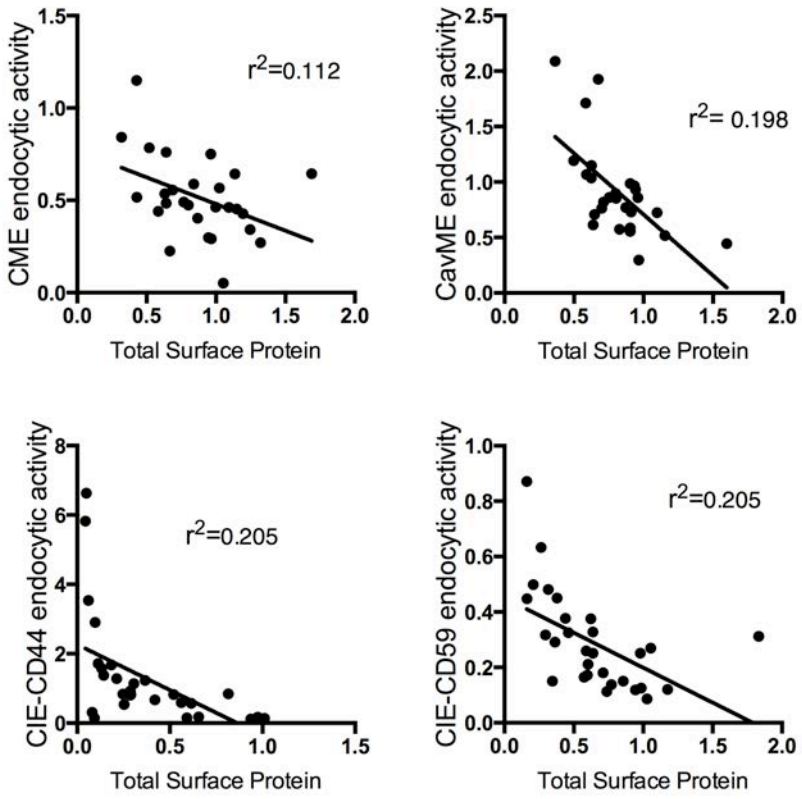

Supplemental Figure 2: Relationship between endocytic activity and total surface expression of receptors. Linear regression analysis comparing endocytic activity and total surface expression of markers used for CME, CavME, CIE-CD44, and CIE-CD59. Correlation was assessed by r^2 values, as indicated.

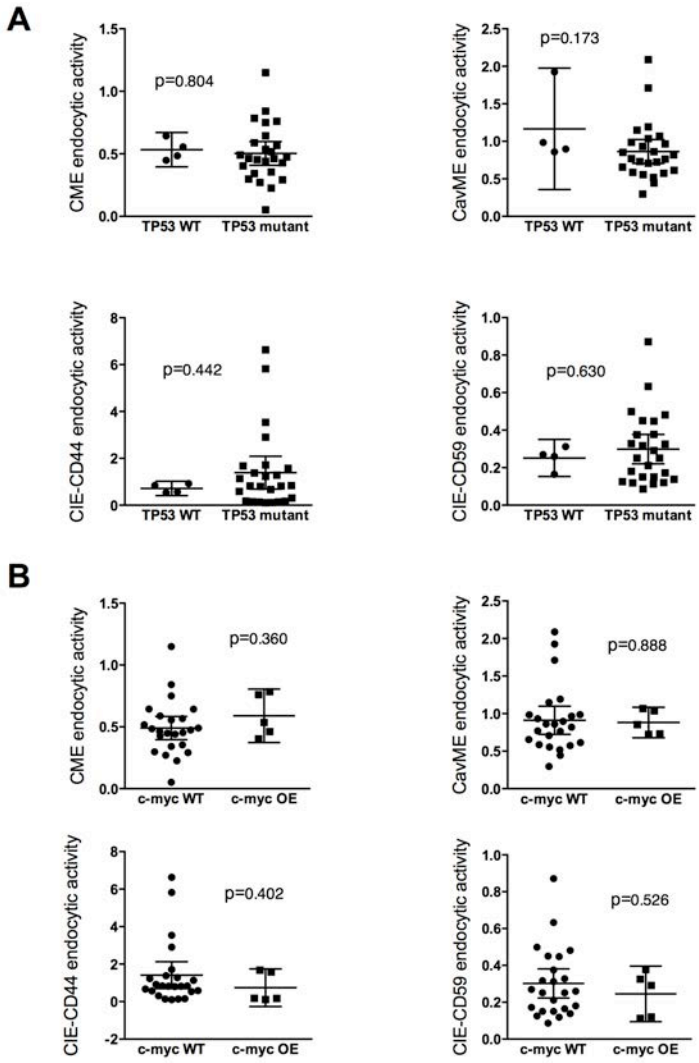

Supplemental Figure 3: Relationship between endocytic activity and genetic alteration associated with cancer cell oncogenic transformation. A) Correlation between p53 mutation status and endocytic activity in all four endocytic pathways. **B**) Correlation between overexpression (OE) status of MYC and endocytic activity in all four pathways. Wilcoxon rank sum tests were used to assess statistical significance, as indicated.

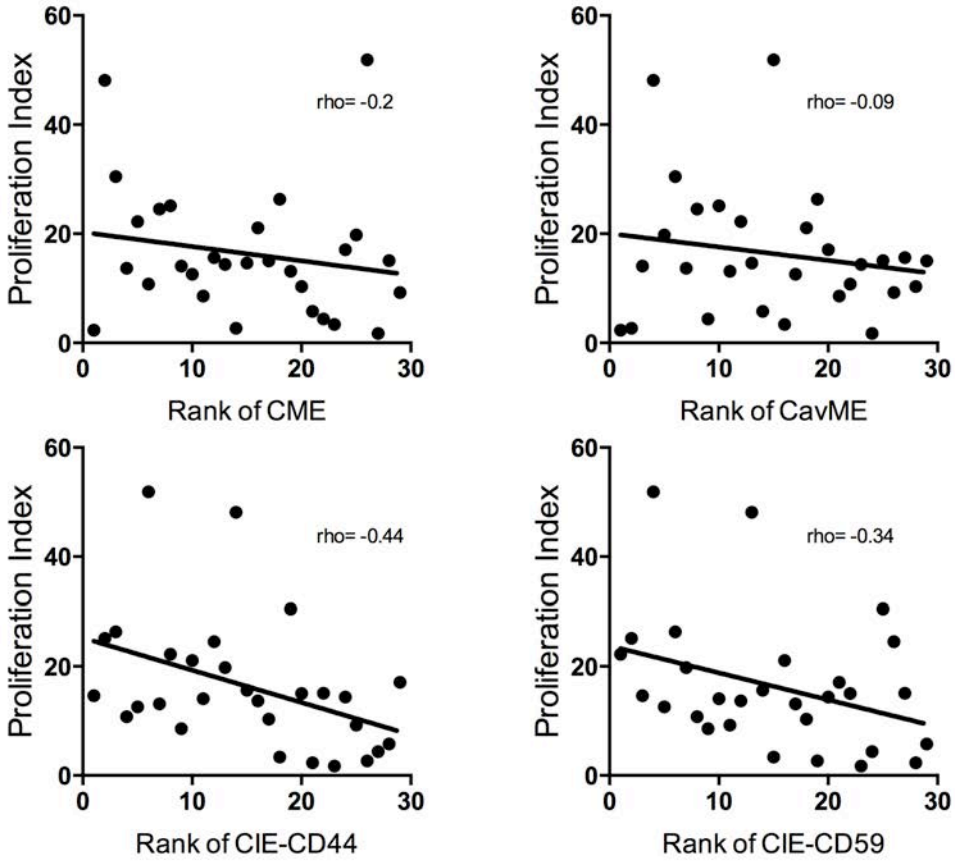

Supplemental Figure 4: Relationship between endocytic activity and proliferation. Spearman correlation of proliferation compared to endocytic activity of CME (not significant), CavME (not significant), CIE-CD44 ($p<.05$), CIE-CD59 ($p=0.07$).

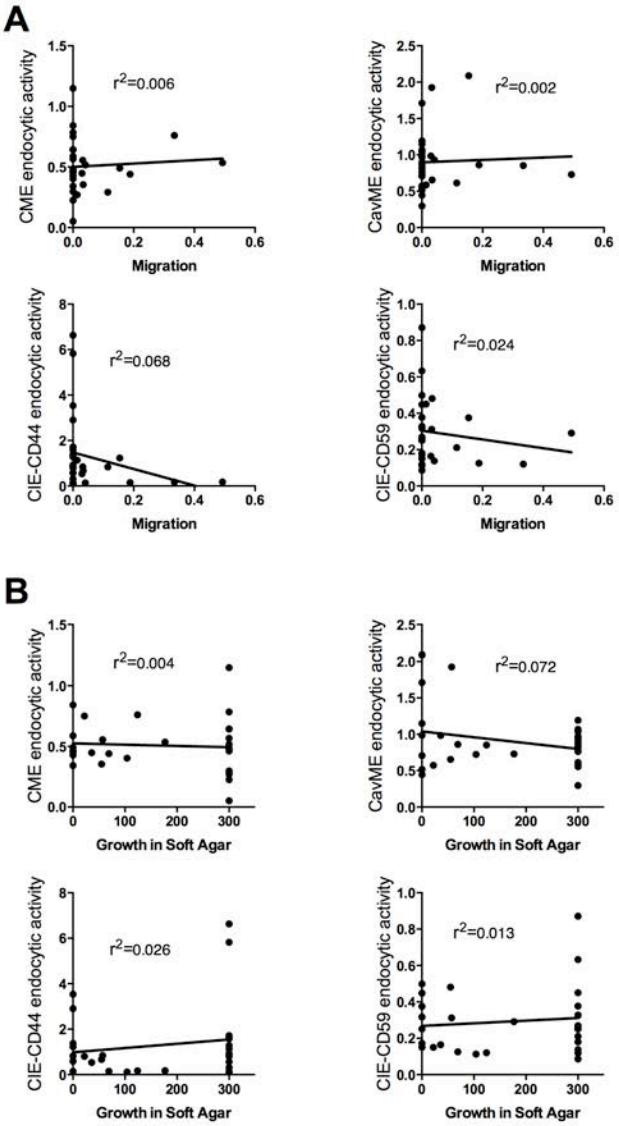

Supplemental Figure 5: Relationship between endocytic activity and cancer cell properties. Linear regression analysis was used to compare endocytic activities with **A)** 3D migration and **B)** growth in soft agar. Correlation was assessed by r^2 values, as indicated.

A

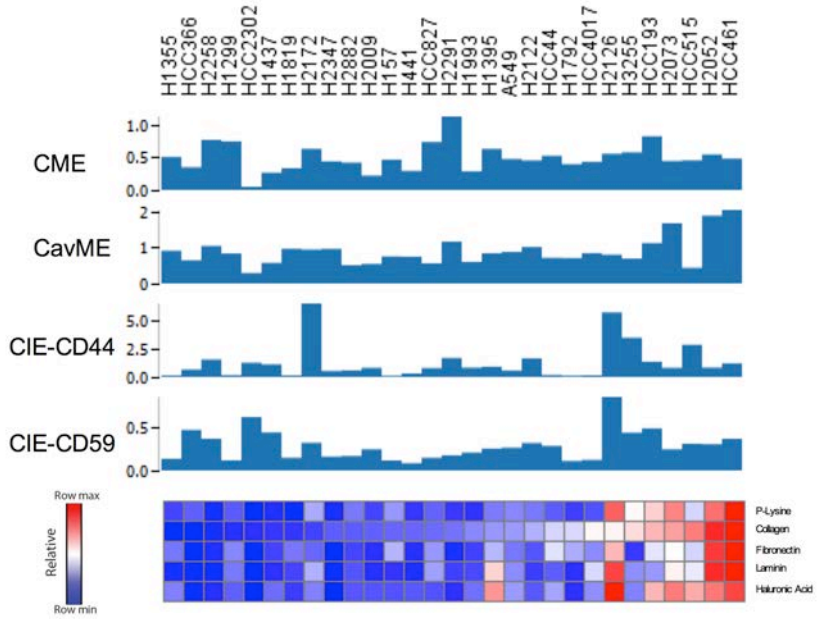

B

	Collagen	Fibronectin	Haluronic Acid	Laminin	P Lysine
Collagen	1	0.81	0.78	0.8	0.83
Fibronectin	0.81	1	0.85	0.89	0.84
Haluronic Acid	0.78	0.85	1	0.9	0.87
Laminin	0.8	0.89	0.9	1	0.87
P Lysine	0.83	0.84	0.87	0.87	1
Pearson correlation coefficient					

Supplemental Figure 6: Relationship between endocytic activity and adhesion. A) Cells were ordered by increasing adhesive properties on different substrates (See Methods). While there were significant differences in measure activities, these differences did not directly correlate with changes in endocytic activities. **B)** Adhesion on one substrate correlated with adhesion on the other substrates tested using a Pearson Correlation. Each histogram displays averages of three independent experiments each performed in triplicate.

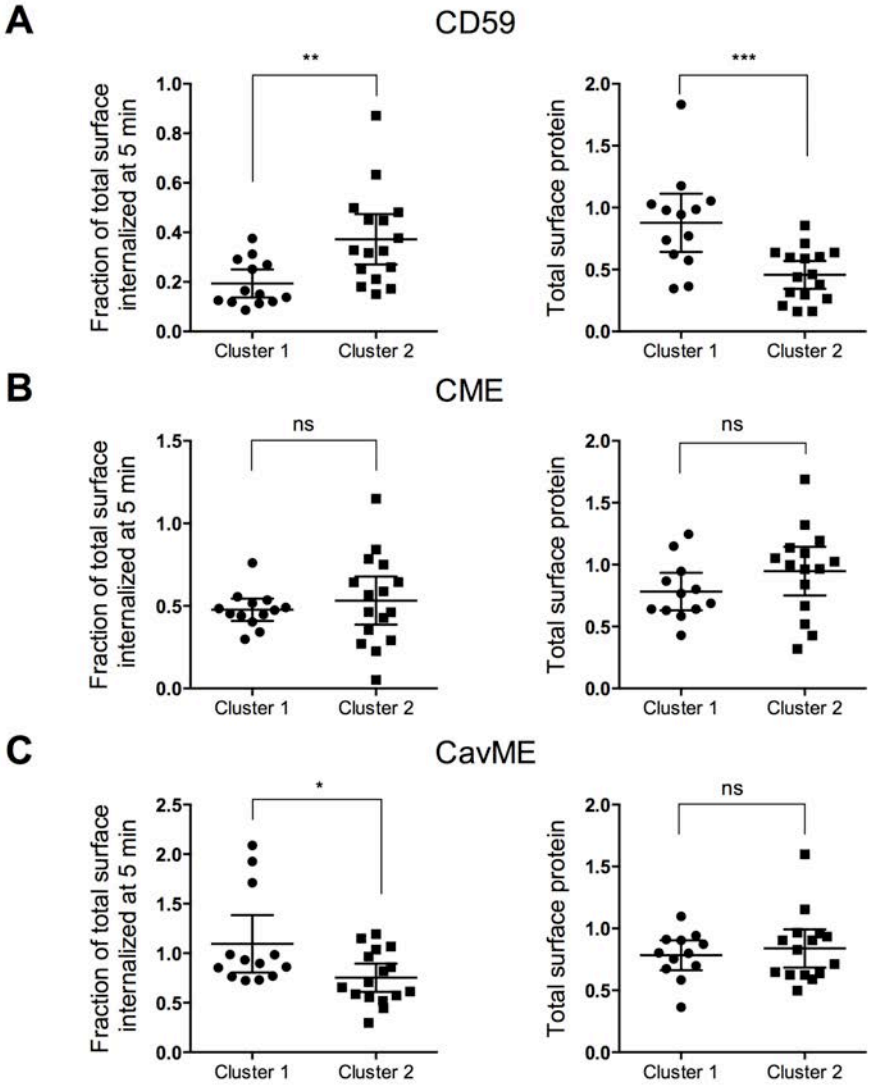

Supplemental Figure 7: Comparison of internalization and total surface binding of endocytic markers between cluster 1 and cluster 2. Comparison of the extent of internalization after 5 min at 37°C and total surface binding, measured at 4°C, of **A)** CIE-CD595 **B)** CavME, **C)** CME. Significance, as indicated, was tested using the Wilcoxon rank sum test.

	CME-TfnR Uptake	STDEV	CavME-Albumin Uptake	STDEV	CIE-CD44 Uptake	STDEV	CIE-CD59 Uptake	STDEV
H157	0.474	±0.176	0.770	±0.249	0.108	±0.027	0.119	±0.090
H441	0.298	±0.107	0.764	±0.296	0.313	±0.159	0.087	±0.065
H1299	0.761	±0.175	0.852	±0.207	0.167	±0.121	0.120	±0.083
H1355	0.517	±0.078	0.932	±0.354	0.135	±0.065	0.138	±0.141
H1792	0.403	±0.145	0.723	±0.138	0.116	±0.084	0.113	±0.031
H1819	0.342	±0.133	0.987	±0.484	0.141	±0.088	0.151	±0.137
Hcc44	0.535	±0.267	0.729	±0.193	0.180	±0.116	0.291	±0.225
Hcc4017	0.440	±0.183	0.861	±0.350	0.151	±0.093	0.126	±0.025
A549	0.484	±0.164	0.897	±0.258	0.572	±0.333	0.270	±0.180
H2052	0.556	±0.205	1.144	±0.300	0.840	±0.309	0.312	±0.096
H2073	0.453	±0.087	1.239	±0.279	0.823	±0.184	0.251	±0.042
H2122	0.461	±0.109	1.037	±0.312	1.679	±0.397	0.326	±0.067
H2172	0.644	±0.189	0.967	±0.156	6.627	±1.185	0.328	±0.189
Hcc193	0.841	±0.356	1.149	±0.430	1.375	±0.318	0.499	±0.244
Hcc461	0.490	±0.101	2.089	±0.965	1.231	±0.256	0.376	±0.145
Hcc827	0.751	±0.288	0.574	±0.273	0.801	±0.327	0.150	±0.045
H1395	0.643	±0.071	0.859	±0.380	0.922	±0.346	0.260	±0.048
H2126	0.566	±0.061	0.821	±0.287	2.964	±0.104	0.677	±0.034
H2258	0.784	±0.112	1.067	±0.312	1.576	±0.553	0.377	±0.197
H2291	1.149	±0.136	1.192	±0.386	1.714	±1.006	0.180	±0.054
H3255	0.589	±0.196	0.707	±0.142	2.014	±1.470	0.448	±0.043
Hcc515	0.463	±0.145	0.445	±0.207	1.506	±0.667	0.317	±0.107
Hcc2302	0.051	±0.029	0.297	±0.057	1.282	±0.515	0.633	±0.021
H1437	0.270	±0.135	0.585	±0.135	1.135	±0.309	0.451	±0.085
H1993	0.292	±0.108	0.613	±0.183	0.837	±0.318	0.211	±0.078
H2009	0.225	±0.056	0.555	±0.115	0.820	±0.365	0.251	±0.093
H2347	0.449	±0.117	0.984	±0.525	0.538	±0.027	0.165	±0.051
H2882	0.533	±0.313	0.518	±0.061	0.589	±0.326	0.172	±0.036
Hcc366	0.355	±0.068	0.656	±0.201	0.670	±0.270	0.481	±0.184

Supplemental Table 1: Rates of uptake at 5 minutes for each endocytic pathway with standard deviation (STDV) in 29 NSCLC cell lines

	Migration	**Growth in Soft Agar**	**Adhesion**				
	Invasion ratio (50/0uM)	Colony number	P-Lysine	Collagen	Fibronectin	Laminin	Haluronic Acid
H157	None	>300	15511	11207	14651	4266	4712
H441	None	>300	8351	11306	4345	3028	4939
H1299	0.334	124	10985	5550	11330	8430	5243
H1355	0.041	>300	9295	1679	10088	2421	6542
H1792	None	104	8923	21276	14047	3995	3295
H1819	None	None	4850	7052	10207	5264	3803
Hcc44	0.493	177	11126	21130	17969	6712	8045
Hcc4017	0.188	69	10404	25481	11606	14160	7163
A549	None	>300	14381	15922	10097	9648	7610
H2052	0.032	57	33884	43994	34475	29104	17073
H2073	None	None	32463	33233	20168	17099	16912
H2122	None	>300	13275	17926	7613	4838	4922
H2172	None	>300	16988	8053	9022	11713	6585
Hcc193	None	None	26744	31145	18193	10315	14606
Hcc461	0.154	None	42328	47412	38560	31549	19122
Hcc827	None	22	11693	11555	12673	10745	4677
H1395	None	>300	13392	15647	14812	18896	15902
H2126	None	>300	35086	25598	25113	27468	21952
H2258	None	>300	5639	4016	3920	1972	3027
H2291	None	>300	8388	12374	3091	5049	3331
H3255	None	None	23719	27771	5579	9718	6669
Hcc515	None	None	20212	36116	16978	15271	14937
Hcc2302	None	>300	3860	6151	1641	882	1401
H1437	0.014	>300	6822	6973	6320	3964	5781
H1993	0.115	>300	7962	14363	6106	5546	5962
H2009	None	>300	9367	10776	4865	3426	4814
H2347	0.030	36	6169	10347	1110	1740	1151
H2882	None	None	13352	10412	6413	6181	4872
Hcc366	0.034	55	11354	1909	1692	1781	1761

Supplemental Table 2: Cancerous properties of 29 NSCLC cell lines

	Proliferation				
	Day 0	Day 1	Day 3	Day 4	Day 5
H157	1	1.82	8.07	11.46	14.65
H441	1	2.29	6.11	12.08	22.22
H1299	1	2.61	15.69	37.73	51.86
H1355	1	4.28	13.06	18.05	26.34
H1792	1	1.76	7.62	15.15	25.13
H1819	1	1.09	4.43	7.11	10.76
Hcc44	1	1.66	6.50	11.25	13.10
Hcc4017	1	1.69	5.94	8.73	12.57
A549	1	1.53	8.58	15.35	21.08
H2052	1	1.18	5.42	8.40	10.33
H2073	1	1.49	2.14	9.49	15.65
H2122	1	0.75	4.46	11.72	14.39
H2172	1	3.09	9.20	14.19	17.08
Hcc193	1	1.37	4.88	8.93	15.05
Hcc461	1	1.02	3.56	8.96	15.04
Hcc827	1	0.949	6.00	10.09	19.79
H1395	1	1.07	2.19	2.55	3.38
H2126	1	1.73	3.97	5.44	5.78
H2258	1	0.993	0.97	2.07	1.72
H2291	1	1.07	3.32	5.03	9.22
H3255	1	2.04	2.68	3.49	4.39
Hcc515	1	0.900	1.11	1.93	2.66
Hcc2302	1	1.02	1.47	2.19	2.34
H1437	1	1.84	15.77	20.33	30.47
H1993	1	1.41	8.11	9.31	13.70
H2009	1	3.04	12.14	30.62	48.11
H2347	1	1.24	3.65	5.85	8.57
H2882	1	1.81	7.24	11.42	14.06
Hcc366	1	2.23	12.77	16.68	24.54

Supplemental Table 2 cont.: Cancerous properties of 29 NSCLC cell lines

CHAPTER FOUR
The Role of Dynamin 1 in Cancer Cell Aggression

Abstract

Metastasis is a multistep process requiring cancer cell signaling, invasion, migration, survival, and proliferation. These processes require dynamic modulation of cell surface proteins by endocytosis. Given this functional connection, we investigated possible mechanisms that lead to altered endocytosis in cancer cells. We discovered that Dyn1, previously thought to be neuron specific is actually ubiquitously expressed and regulated in cancer cells by multiple posttranslational regulation mechanisms. Moreover, Dyn1 expression alters the proliferation rates, growth in soft agar, and tumor growth of cancer cells. We hypothesize that these changes are due to alteration in cell surface proteins and signaling molecule expression and have optimized protocols to test these hypothesizes. Taken together, our results suggest that endocytic alterations in cancer cells that affect cell surface expression of critical molecules have a significant influence on cancer-relevant phenotypes.

Introduction

Cancer metastasis is a multi-step process that requires changes in many cellular behaviors such as a cell's ability to adhere, proliferate, and migrate. These cellular adaptations require alterations in cell-cell interactions, cell-matrix interactions, survival and proliferative signaling, as well as appropriate and sufficient nutrient uptake [113, 114]. All are mediated by cell surface receptors. Endocytosis, the process by which cells take up macromolecules and receptors through plasma membrane (PM) invagination and edocytic vesicle formation, in turn regulates the expression and activity of cell surface receptors.

The most studied and well-characterized endocytic mechanism is clathrin-mediated endocytosis (CME), which occurs through clathrin coated pits (CCPs) and clathrin coated vesicles (CCVs), The principle components of the coated vesicles are the heavy and light chains of clathrin [15], and the four subunits of the heterotetrameric adaptor protein 2 (AP2) complex [16]. The AP2 complex links the clathrin coat to the membrane bilayer and is also the principle cargo-recognition molecule [17]. CCV formation proceeds through multiple stages: initiation, cargo-selection, growth and maturation, scission, and uncoating. CCP assembly is initiated by AP2 complexes that then rapidly recruit clathrin [23]. As the nascent CCPs grow, AP2 and other cargo-specific adaptor proteins recruit and concentrate cargo. Budding of CCVs from the plasma membrane depends on the large GTPase dynamin (Dyn) [27]. Dyn assembles into collar-like structures encircling the necks of deeply invaginated pits and undergoes GTP hydrolysis to drive membrane fission [27].

Although CME was once considered a constitutive process, it has become increasingly clear that CME can be dynamically-regulated in response to changes in the extracellular and intracellular environment. Our lab has previously shown that in addition to its well-understood function in catalyzing membrane fission [27], Dyn also regulates early stages of CCP assembly and maturation [26, 154, 155].

Vertebrates encode three differentially expressed isoforms of Dyn. Dynamin 1 (Dyn1) is highly expressed in brain [156], while dynamin 2 (Dyn2) is ubiquitously expressed, and dynamin 3 (Dyn3) is enriched in the brain, lung, and testes. Dyn3 is thought to play a redundant function with Dyn1 because Dyn3 KO mice have no phenotype [157].

Dyn1 and Dyn2 are closely related, sharing 75% overall identity. The greatest divergence occurs in the C-terminal Proline/Arginine Rich Domain or PRD that binds to many SH3 domain-containing partners and is the site for regulatory phosphorylation. Furthermore, Dyn1 and Dyn2 have strikingly different biochemical properties that might reflect different roles for the two isoforms in regulating CME [158]. Dyn1 is a strong curvature generator, while Dyn2 is a curvature sensor that only assembles on highly curved membranes. Additionally, Dyn1 previously assumed to be a neuron specific isoform, is in fact ubiquitously expressed [159]. Furthermore, Dyn1 is regulated in non-neuronal cells by phosphorylation/dephosporylation downstream of the cancer driving kinase Akt [160]. Activation of Dyn1 leads to enhanced rates of CME, enhanced rates of CCP initiation and

rapid and dysregulated CCP maturation as measured by total internal reflection fluorescence microscope (TIRFM).

The findings discussed above suggest that crosstalk between signaling molecules such as Akt, a known oncogene, and components of CME could allow a pathological advantage to cancer cells. Indeed, previous work has shown that in the non-small cell lung cancer (NSCLC) cell line, H1299, inhibition of Akt decreases the rate of CME as measured by the uptake of transferrin receptor (TfnR) [160]. Thus, the overexpression and/or activation of Dyn1 in cancer cells and resulting changes in CME might be an adaption that leads to an enhanced ability to proliferate, survive, and/or migrate through alterations in the composition and activity of surface receptors that control essential cellular behaviors, which contribute to cancer cell aggressiveness.

Results:

Diverse mechanisms underlie adaptive CME in cancer cells.

It has been previously shown that the expression levels of several important components of CME are altered in cancer. Furthermore, specific components of CME have previously been implicated in tumorigenesis [116]. However, changes in Dyn1 expression levels in cancer have yet to be reported and the possible role of Dyn1 in tumorigenesis has never been explored. Therefore, we examined mRNA levels of Dyn1 in NSCLC and normal

lung epithelial cell lines. We found elevated levels of Dyn1 mRNA amongst 108 NSCLC lines compared to 50 normal lung epithelial cell lines although both express similar levels of Dyn2 (Figure 1A). In addition, lower survival rates in lung cancer patients were linked to high levels of Dyn1 expression, especially amongst smokers [161]. These results suggest that Dyn1 is another component of CME that is altered in cancer and that changes in Dyn1 expression might play an important role in turmorigenesis.

One drawback of measuring mRNA expression is that it does not necessarily correlate with protein expression [162]. Therefore, in order to confirm whether protein expression levels of Dyn1 matched mRNA expression levels, five NSCLC cell lines with a range of Dyn1 mRNA levels were selected and Dyn1 and Dyn2 protein expression was determined by western blot. Indeed there were quantitative differences between Dyn1 mRNA and protein levels (Figure 1B). These data suggest that Dyn1 expression is regulated by both transcriptional and posttranscriptional mechanisms. By contrast, Dyn2 levels were uniform across all cell lines.

To determine the relative roles of Dyn1 and Dyn2 in CME, the uptake of the transferrin receptor (TfnR), a marker for CME, was measured in the presence or absence of siRNA knockdown (KD) of Dyn1 or Dyn2 in the five NSCLC cell lines. Interestingly, Dyn1 expression levels did not appear to correlate with an increased dependence of Dyn1 in these cells (Figure 1C). Although, with the exception of H2073 cells, increased Dyn1 expression correlated with reduced dependence of CME on Dyn2. High Dyn1 protein expression did not

sensitize cells to siRNA knockdown of Dyn1. These results establish that neither mRNA nor protein expression determines the activity of Dyn1 in regulating CME in cancer cells and suggests that posttranslational modifications might be important.

Previous work has suggested that Dyn1 is regulated by phosphorylation/dephosphorylation downstream of Akt and GSK3β [160]. Dyn1 is phosphorylated at S774 and inactivated by GSK3β, which can be phosphorylated and inactivated by Akt (Figure 1D). Therefore, we hypothesized that activation of Dyn1 by dephosphorylation might be more important than expression levels in cancer cells. To test this, Dyn1 phosphorylation at S774 was compared in the five NSCLC cell lines. Indeed the levels of Dyn1 phosphorylation were inversely correlated with Dyn1 expression in that cell lines expressing high levels of Dyn1 (H2073 and A549) also exhibited high levels of phosphorylated, and thus inactive Dyn1 (Figure 1D).

We next tested whether a GSK3β inhibitor, which should reduce Dyn1 phosphorylation, might activate Dyn1 in the five cell lines. Indeed, Dyn1 activation correlated with increased rates of CME as measured by TfnR uptake. Cell lines expressing high levels of phosphorylated Dyn1 (e.g. H2073 and A549) had a significant increase in uptake (Figure 1E). Interestingly, H1299, which expresses the lowest amount of Dyn1 and also had no detectable levels of Dyn1 phosphorylation, also showed a significant increase in uptake in the presence of the GSK3β inhibitor. From these results we can conclude that Dyn1 activity in NSCLC cells can be regulated transcriptionally post transcriptionally and by

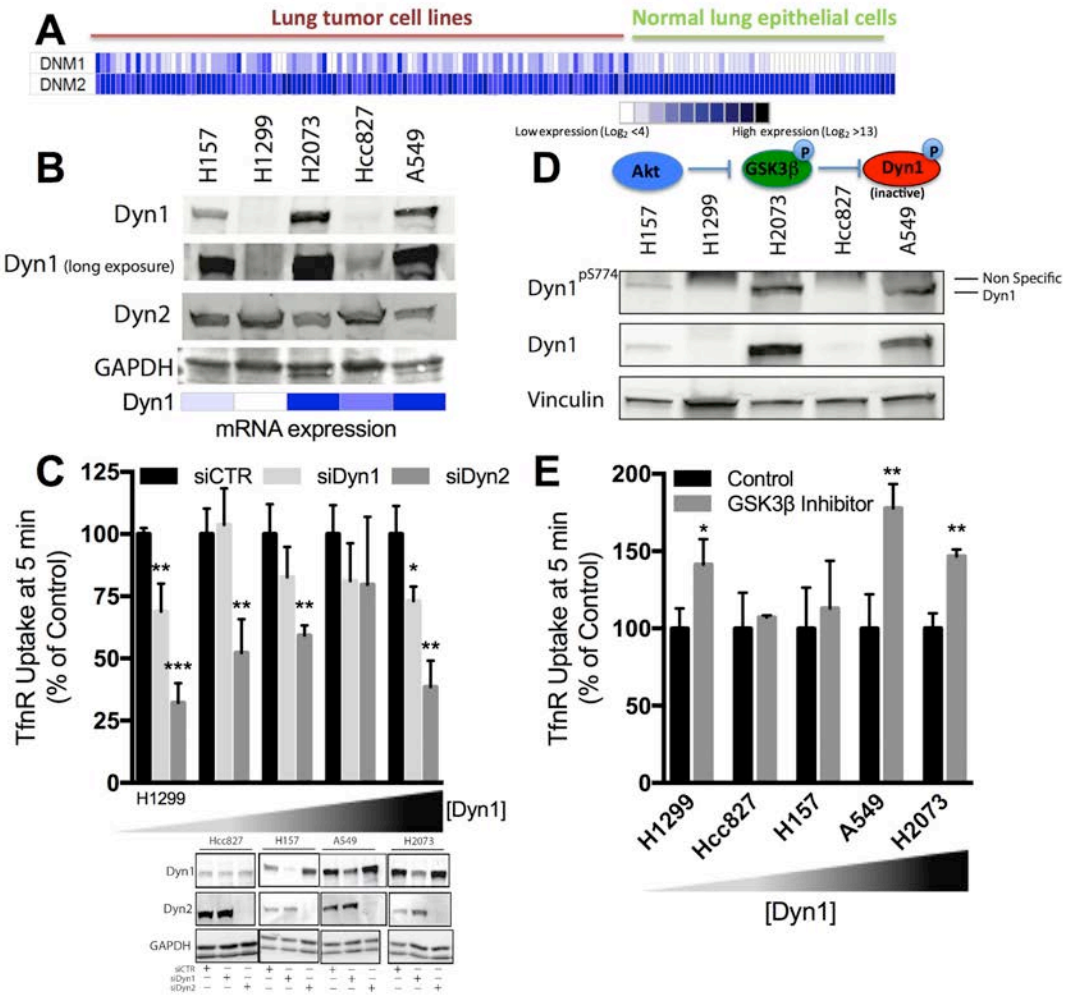

Figure 1: Diverse mechanisms underlie adaptive CME in cancer cells. **A)** Dyn1 (DNM1) mRNA, but not Dyn2 (DNM2) mRNA is upregulated in many nonsmall cell lung cancer (NSCLC) cell lines relative to normal bronchial epithelial cells. **B)** Comparison of Dyn1 and Dyn2 protein expression in 5 NSCLC cell lines relative to mRNA expression. **C)** Comparison of the effect of Dyn1 or Dyn2 knockdown on TfnR uptake at 5 minutes in 5 NSCLC cell lines with increasing Dyn1 protein expression. **D)** Schematic of Dyn1 regulation downstream of Akt. Comparison of Dyn1 phosphorylation in 5 NSCLC cell lines with varying Dyn1 protein expression. **E)** Comparison of the effect of a GSK3β inhibitor on TfnR uptake at 5 minutes in 5 NSCLC cell lines with increasing Dyn1 protein expression. Statistical significance was assessed by two-tailed Student's t-test. *$p < 0.05$; **$p < 0.005$; ***$p < 0.0005$. All experiments represent ($n = 3$, avg. ± SD).

posttranscriptional modifications. Moreover, although GSK3β appears to regulate Dyn1 activation there might be other mechanisms of Dyn1 activation in cancer cells, for example by regulation of phosphatase activities [163]. These results suggest that there are multiple posttranslational regulation mechanisms that affect Dyn1 activity.

The effect of Dyn1 KD and KO on endocytic trafficking in H1299 cells

During maturation, early endosomes acquire the Rab5 effectors APPL1 and EEA1 either sequentially [164] or distinctly [165]. APPL1 also functions as a scaffold on the endosomal surfaces that interacts with Akt and regulates its activity [165]. Previous work had suggested that Dyn1 expression might cause changes in endocytic trafficking specifically altering the number and distribution of APPL1 and EEA1 endosomes in the cell [160]. To test this hypothesis, we treated H1299 cells with Dyn1 siRNA and looked for morphological changes in these early endosomal compartments. Dyn1 KD cells showed no phenotypic change in EEA1 endosomes. However, APPL1 endosomes became more dispersed and redistributed to the periphery of the cell (Figure 2A).

RNA interference (RNAi) using siRNA cannot completely ablate protein expression and only provides transient inhibition. To overcome these pitfalls of RNAi we used CRISPR-Cas9, which targets DNA with less off target effects and provides complete knockout. Interestingly, H1299 Dyn1 knockout (KO) cells did not have the same APPL1 endosomal

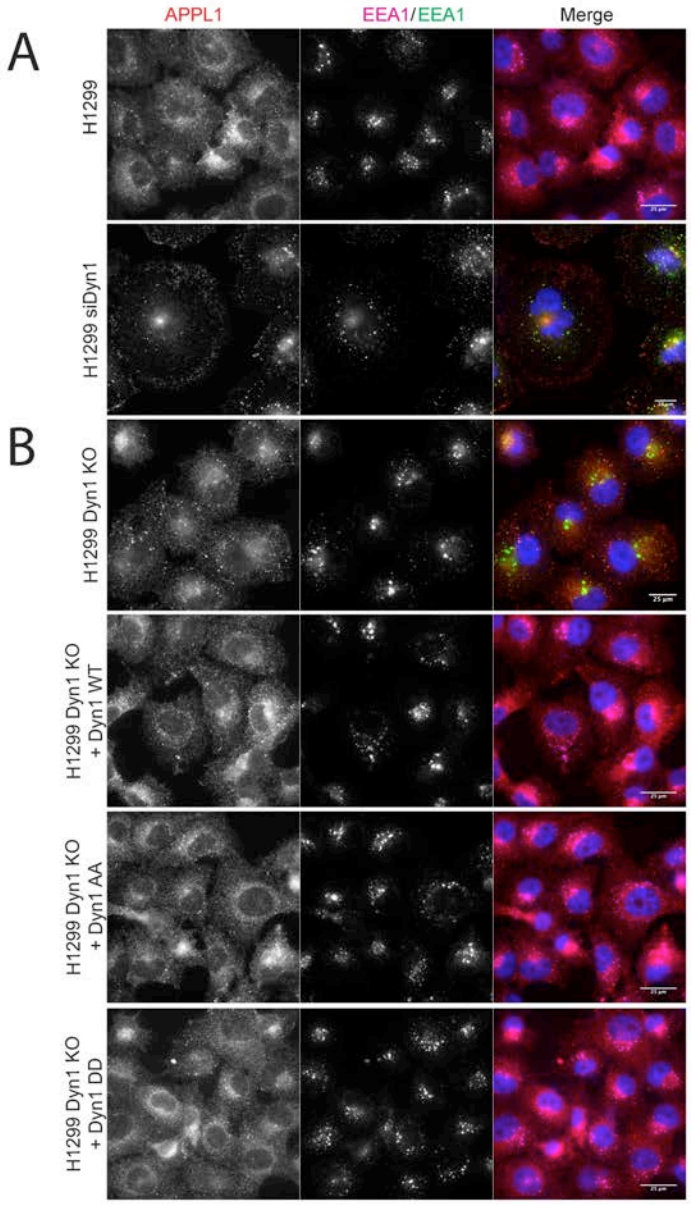

Figure 2: Effect of Dyn1 depletion on early endocytic trafficking in H1299 cells. **A)** Immunofluorescence of siDyn1 treated or control H1299 cells **B)** Dyn1 knockout cells (Dyn1 KO) and Dyn1 KO cells reconstituted with Dyn1 $Dyn1^{WT}$-EGFP, $Dyn1^{S774A/S778A}$-EGFP, or Dyn1 $Dyn1^{S774D/S778D}$-EGFP as indicated. Cells are probed with antibodies to APPL1 or EEA1 containing early endosomes.

phenotype seen in H1299 Dyn1 KD cells (Figure 2B). APPL1 and EEA1 endosomes in H1299 Dyn1 KO cells looked like those in H1299 control cells.

To further explore the role of Dyn1 in regulating endosomal trafficking several different Dyn1 constructs were reintroduced into H1299 Dyn1 KO cells. Rescue with wild type (WT) Dyn1 fused to EGFP ($Dyn1^{WT}$-EGFP) had no effect on APPL1 and EEA1 endosome morphology (Figure 2C). In order to determine if Dyn1 activation by phosphorylation plays a role in alteration of endosomal trafficking, two known regulation sites of Dyn1, S774 and S778, were mutated to create a nonphosphorylatable Dyn1 ($Dyn1^{S774A/S778A}$-EGFP) and a phosphomimetic Dyn1 ($Dyn1^{S774D/S778D}$-EGFP). However, neither Dyn1 constructs had any effect on APPL1 and EEA1 endosomes (Figure 2D). These results suggest that although transient knockdown of Dyn1 appears to change the trafficking of APPL1 endosomes this phenotype is not observed in either Dyn1 KO and Dyn1 rescued cells. Thus, while short-term removal of Dyn1 alters endocytic trafficking, cells were able to compensate when Dyn1 is deleted.

The effect of Dyn1 KO and reconstitution on proliferation

CME controls signaling downstream of mitogenic receptors such as EGFR [166], therefore we next asked if Dyn1 expression had any effect on the ability of cancer cells to proliferate. Proliferation rates of H1229 parental, Dyn1 KO, Dyn1 KO + $Dyn1^{WT}$-EGFP, Dyn1 KO + $Dyn1^{S774A/S778A}$-EGFP, and Dyn1 KO + $Dyn1^{S774D/S778D}$-EGFP were compared.

Dyn1 KO cells grew significantly slower than the parental cell lines (Figure 3A), and this growth defect was rescued by reintroducing Dyn1 WT and Dyn1$^{S774A/S778A}$, but not by Dyn1$^{S774D/S778D}$. Dyn1 was also required for proliferation in a second NSCLC cell line: A549 (Figure 3B).

Dyn2 has previously been shown to play a role in cell cycle progression through association with microtubules at mitosis [167] and a role in cytokinesis [168]. Therefore, we tested whether the growth effects of Dyn1 KO were due to defects in the cell cycle. However, there was no biologically significant change in the percent of cells in each phase of the cell cycle in parental and Dyn1 KO H1299 and A549 cells (Figure 3C and D respectfully). These results suggest Dyn1 expression alters the proliferation rates of cancer cells but that Dyn1 effects on proliferation are not due to changes in the cell cycle.

Interestingly, A549 KO cells were more sensitive to media composition than parental cells (Figure 3E). Two plates of A549 Dyn1 KO cells were seeded at the same time and density. One plate received new media on day 1 and day 3 (control) while the other plate remained in the original media. After four days the cells in the plate that did not receive fresh media were rounded and dead while the cells in the control plate were still healthy and growing. Not changing the media had no effect on A549 parental cells (data not shown) or H1299 parental or knockout cells (data not shown). These results suggest alterations in A549 Dyn1 KO cells lead to an enhanced susceptibility either to depletion of something in the media (possibly nutrients or growth factors) or Dyn1 KO A549 cells might produce

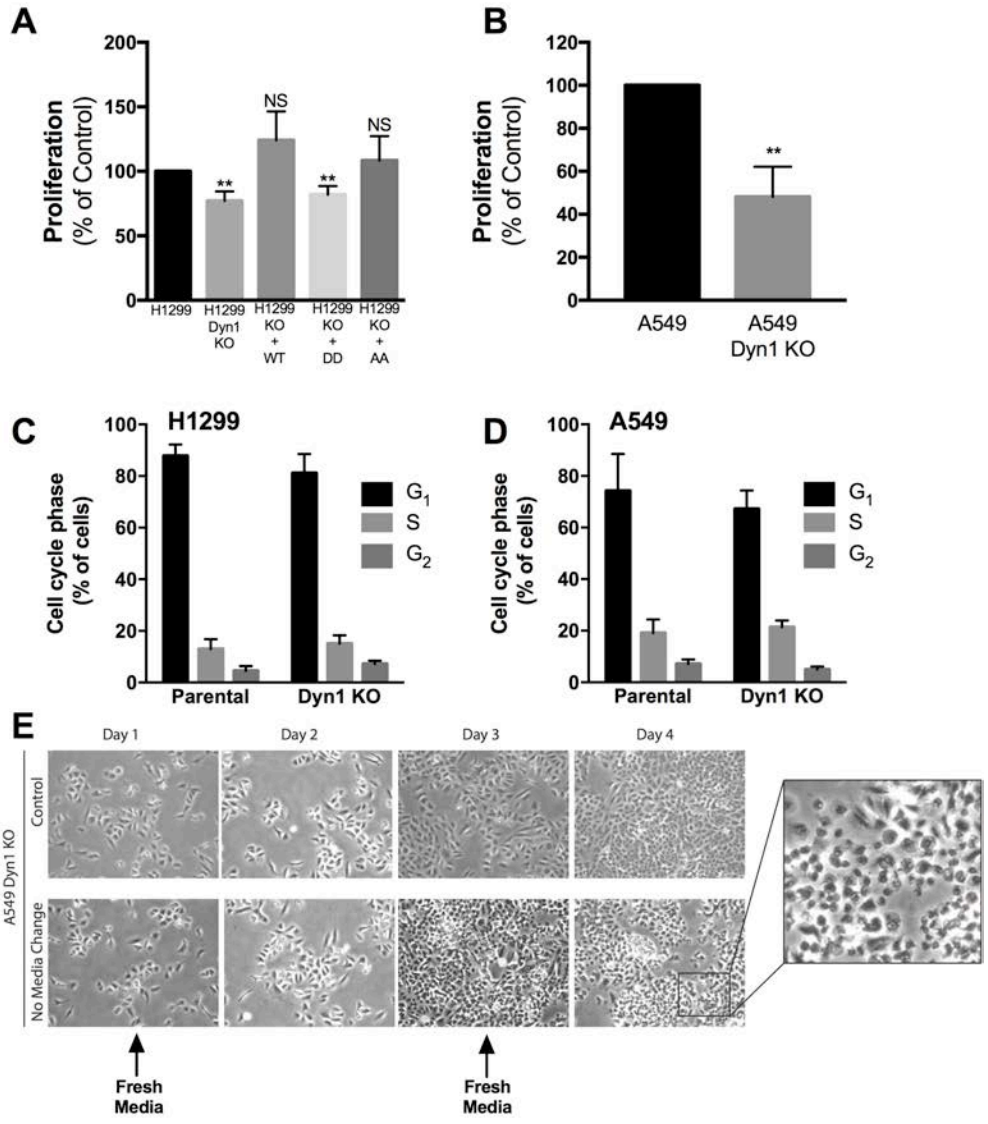

Figure 3: Effect of Dyn1 depletion on cell proliferation. **A)** Proliferation of H1229 parental, Dyn1 KO, Dyn1 KO + Dyn1^{WT}-EGFP, Dyn1 KO + Dyn1$^{S774A/S778A}$-EGFP, and Dyn1 KO + Dyn1$^{S774D/S778D}$-EGFP cells after 4 days. **B)** Proliferation of A549 parental and Dyn1 KO cells after 4 days. Percent of either parental or Dyn1 KO cells from total population in each cell cycle phase in **C)** H1299 or **D)** A549 cells. **E)** A549 Dyn1 KO cells were plated with fresh media and then allowed to grow. Arrows indicate that media was changed in the control group on Day 1 and Day 3. Statistical significance was assessed by two-tailed Student's t-test. *$p < 0.05$; **$p < 0.005$; ***$p < 0.0005$. All experiments represent ($n = 3$, avg. ± SD).

something in the media that is toxic. Regardless, Dyn1 KO in A549 cells causes a differential response of surface proteins to the environment.

The effect of Dyn1 and reconstitution on tumor growth in vitro and in vivo

Anchorage independent growth of cells in soft agar is one of the main methods to measure cellular transformation and uncontrolled cell growth; nontransformed cells typically cannot grow in this condition. Therefore, growth in soft agar was used to determine the role of Dyn1 in anchorage-independent uncontrolled cell growth. H1229 parental, Dyn1 KO, Dyn1 KO + Dyn1^{WT}-EGFP, Dyn1 KO + Dyn1$^{S774A/S778A}$-EGFP, and Dyn1 KO + Dyn1$^{S774D/S778D}$-EGFP were cultured in soft agar. H1299 Dyn1 KO cells grew less effectively in soft agar compared to the parental cell lines (Figure 4A and B) and this phenotype was rescued by reintroduction of Dyn1 WT. Unexpectedly, both Dyn1 KO + Dyn1$^{S774A/S778A}$-EGFP, and Dyn1 KO + Dyn1$^{S774D/S778D}$-EGFP were also able to restore growth in soft agar to WT levels. However, the size of colonies in the Dyn1 KO + Dyn1$^{S774A/S778A}$-EGFP, and Dyn1 KO + Dyn1$^{S774D/S778D}$-EGFP conditions differed (Figure 4B). Dyn1 KO + Dyn1$^{S774A/S778A}$-EGFP cells grew fewer larger colonies while Dyn1 KO + Dyn1$^{S774D/S778D}$-EGFP grew more smaller colonies. As with H1299 cells, Dyn1 KO A549 cells had a decrease in the number and size of colonies (Figure 4C and D). Together these results suggest that Dyn1 expression and activity can affect growth of transformed cells in soft agar.

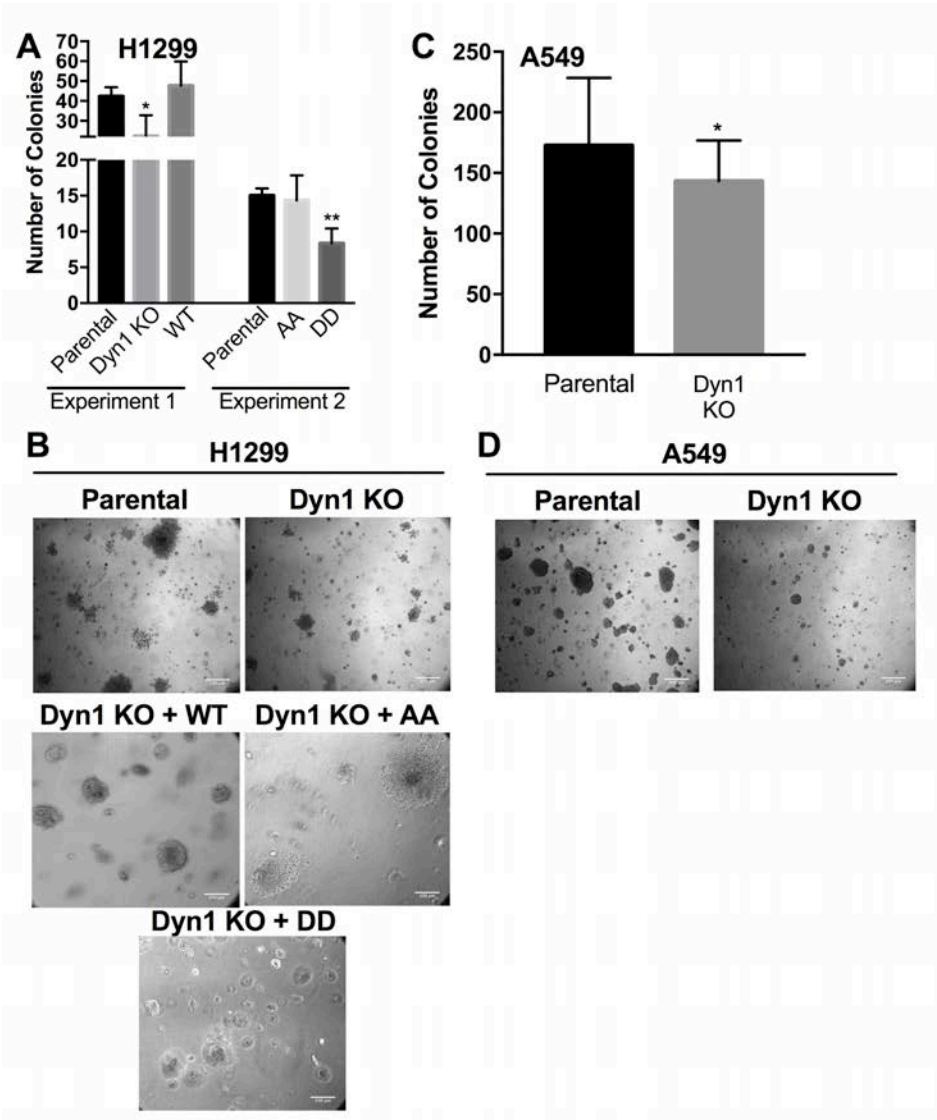

Figure 4: Effect of Dyn1 depletion on growth in soft agar. Quantification of the number of colonies formed in soft agar and representative pictures of colony growth either from **A, B)** H1299 or **C, D)** A549 cells. Statistical significance was assessed by two-tailed Student's t-test. *$p < 0.05$; **$p < 0.005$; ***$p < 0.0005$. All experiments represent ($n = 3$, avg. ± SD)

To future explore the effects of Dyn1 expression on tumor growth we used a mouse xenograft model, which is routinely used to easily monitor tumorigenicity and tumor growth and identify anticancer targets. Nude SCID mice were injected subcutaneously with H1299 and H1299 Dyn1 KO cells. Tumors were harvested 40 days post injection and their volumes were measured. Similar to our *in vitro* data, Dyn1 KO cells formed smaller tumors than the parental cells (Figure 5A). We repeated the experiment with the entire Dyn1 construct library: H1229 parental, Dyn1 KO, Dyn1 KO + $Dyn1^{WT}$-EGFP, Dyn1 KO + $Dyn1^{S774A/S778A}$-EGFP, and Dyn1 KO + $Dyn1^{S774D/S778D}$-EGFP. Interestingly, Dyn1 KO tumor growth was variable and heterogeneous and although there was a tendency to reduce growth, this did not reach statistical significance relative to the parental (Figure 5B). However, Dyn1 WT tumors grew more homogeneously and as efficiently as parental tumors. Dyn1 KO + $Dyn1^{S774A/S778A}$-EGFP cells grew larger tumors in 3 of the 4 mice while Dyn1 KO + $Dyn1^{S774D/S778D}$-EGFP had significantly reduced tumor growth compared to parental and Dyn1 KO + $Dyn1^{WT}$-EGFP tumors (Figure 5B). While we did not observe significant difference between H1299 and Dyn1 KO tumors, when we combined our results from our two mouse experiments we observed a significant difference between the two conditions (data not shown). We also observed a significant difference between the Dyn1 KO + $Dyn1^{WT}$-EGFP, Dyn1 KO + $Dyn1^{S774A/S778A}$-EGFP, and Dyn1 KO + $Dyn1^{S774D/S778D}$-EGFP conditions.

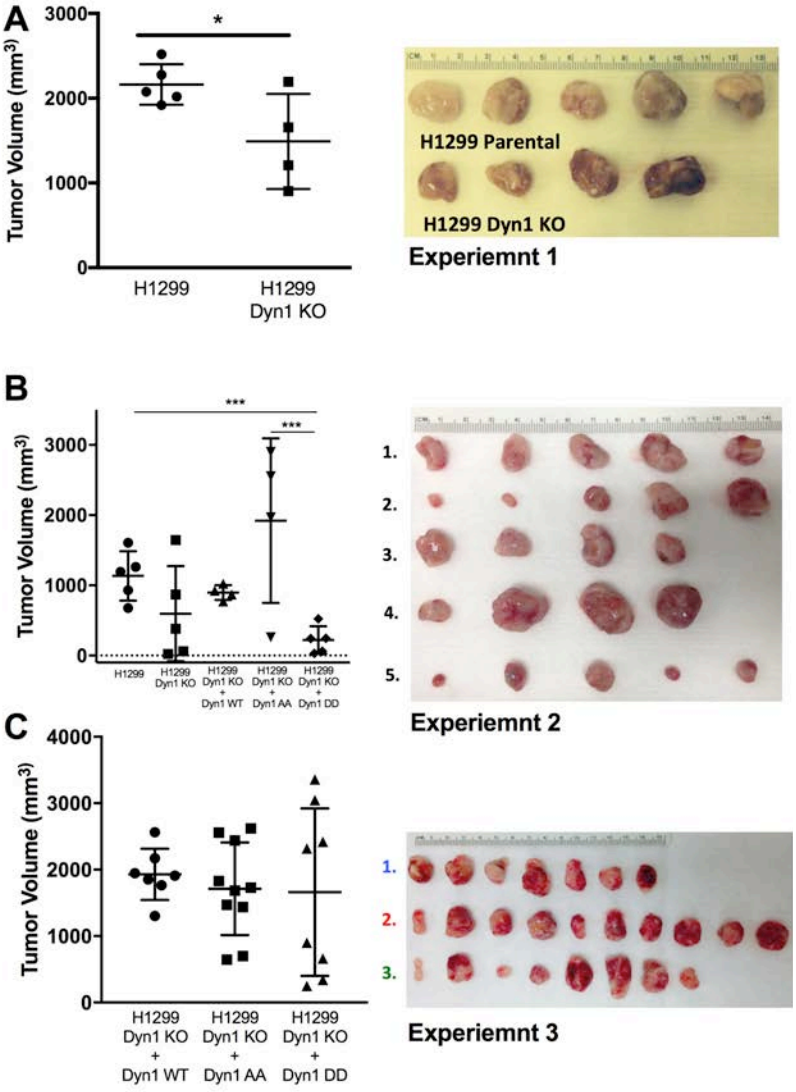

Figure 5: Effect of Dyn1 depletion on tumor growth *in vivo*. Tumor volume measured 40 days after injection and images of extracted xenograft tumors derived from **A)** H1299 parental or H1299 Dyn1 KO **B)** H1229 parental, Dyn1 KO, Dyn1 KO + Dyn1^{WT}-EGFP, Dyn1 KO + Dyn1$^{S774A/S778A}$-EGFP, and Dyn1 KO + Dyn1$^{S774D/S778D}$-EGFP. All experiments represent (n = 5, avg. ± SD) **C)** Dyn1 KO + Dyn1^{WT}-EGFP, Dyn1 KO + Dyn1$^{S774A/S778A}$-EGFP, and Dyn1 KO + Dyn1$^{S774D/S778D}$-EGFP (n = 10, avg. ± SD). Statistical significance was assessed by two-tailed Student's t-test. *$p < 0.05$; **$p < 0.005$; ***$p < 0.0005$.

Given the observed heterogeneity a third experiment was performed, this time using only the Dyn1 KO + Dyn1^{WT}-EGFP, Dyn1 KO + Dyn1$^{S774A/S778A}$-EGFP, and Dyn1 KO + Dyn1$^{S774D/S778D}$-EGFP cells, as these were derived from the same Dyn1 KO H1299 clone. We also used a larger number of mice, 10 instead of 5 per condition. Surprisingly, there were no differences between any of the three conditions for this experiment (Figure 5C). Once again we obtained inconsistent results and a high degree of variability. Though we do not know why these experiments had such a high degree of variability, some possibilities might be: 1) clonal variation from CRISPR, since our KO and rescue conditions all come from a single clone derived from a heterogeneous H1299 parental line. 2) There might have been technical issues such as low cell viability or growth stage, not enough cells injected, or the cell's time in culture. Finally, a different mouse model, such as a metastasis model, might be a better model for measuring the role of Dyn1 *in vivo*.

Reverse Phase Protein Array (RPPA)

In an attempt to gain more insight from the large degree of variability observed in our xenograft experiments and a better understanding of the role of Dyn1 expression in tumorigenesis, we asked: Can effects of Dyn1 on tumor growth be correlated with changes in signaling pathways? One approach to address this question is to use a Reverse Phase Protein Array (RPPA), a robust, sensitive, cost-effective antibody-based approach with the ability to analyze a large number of samples for quantitative assessment of key protein molecules in

functionally relevant pathways. RPPA allows simultaneous examination of multiple signaling molecules and their functional status.

Protein lysates were prepared from frozen tissue acquired from the mouse experiments above (H1299 and H1299 Dyn1 KO from experiment 1 or H1229 parental, Dyn1 KO, Dyn1 KO + $Dyn1^{WT}$-EGFP, Dyn1 KO + $Dyn1^{S774A/S778A}$-EGFP, and Dyn1 KO + $Dyn1^{S774D/S778D}$-EGFP from experiment 2). Serial diluted lysates were arrayed on nitrocellulose-coated slides probed with 303 validated primary antibodies plus a biotin-conjugated secondary antibody. The slides were scanned, analyzed, and quantified using customized software to generate spot intensity. Relative protein levels for each sample were determined by interpolation of each dilution curves from the standard curve of the slide. The protein concentrations of each set of slides were then normalized for protein loading and transformed to a linear value which was then used to look for proteins with significantly different expression or functional status ($p \leq 0.01$) between H1299 parental or H1299 Dyn1 KO + $Dyn1^{WT}$-EGFP and Dyn1 KO, Dyn1 KO + $Dyn1^{S774D/S778D}$-EGFP, and Dyn1 KO + $Dyn1^{S774A/S778A}$-EGFP.

Fifty-four proteins were identified as being significantly different between H1299 parental and Dyn1 KO tumors from two replicate experiments (Table 1). While twenty-eight and five proteins were identified as being significantly different between H1299 parental and Dyn1 KO + $Dyn1^{S774D/S778D}$-EGFP or Dyn1 KO + $Dyn1^{S774A/S778A}$-EGFP respectfully (Table 1). Five, three, and thirteen proteins were identified as being significantly different between

Table 1: RPPA Results using p-value cutoff < 0.01							
Parental vs.				**Dyn1 KO + Dyn1 WT vs.**			
Dyn1 KO (n=2)	**Dyn1 KO + Dyn1 DD**	**Dyn1 KO + Dyn1 AA**	**Dyn1 KO + Dyn1 WT**	**Dyn1 KO**	**Dyn1 KO + Dyn1 DD**	**Dyn1 KO + Dyn1 AA**	**Dyn1 KO Experiment 2: Small vs. Large**
14-3-3-zeta	53BP1	ACC1		c-Abl	Bax	ARID1A	B-Raf
AMPKa	ATM	ATM		c-Kit	Glutaminase	PI3K p85	NF-kB-p65_pS536
Atg7	Bax	b-Catenin pT41_S45		FAK	GSK-3a/b pS21_S9	TUFM	Rad51
ATM	NF-kB-p65_pS536	DJ1		MAPK pT202_Y204	NF-kB-p65_pS536		Rb pS807_S811
Axl	c-Kit	PMS2		NDRG1 pT346	MSH6		
B-Raf	cdc25C				mTOR pS2448		
B-Raf pS445	Creb				IGFRb		
Bak	GSK-3a/b pS21_S9				p53		
Bcl-xL	IGFRb				p90RSK pT573		
Beclin	IR-b				PAR		
c-Kit	MSH6				Rictor pT1135		
Caspase-3	PSIN-A				RPA32 pS4_S8		
DUSP4	Beclin				Src pY527		
E-Cadherin	p27 pT198						
eEF2	p53						
Elk1_pS383	p90RSK pT573						
FAK	PAR						
Gab2	PKCa						
Granzyme-B	PR						
Hexokise-II	PREX1						
Histone-H3	Rictor						
HSP27_pS82	Rictor pT1135						
IR-b	RIP						
IRS1	RPA32 pS4_S8						
JNK pT183_Y185	Shc pY317						

LRP6 pS1490	Smad1						
MAPK pT202_Y204	Src pY527						
Mcl-1	TIM-3						
Merlin							
MSH6							
NDRG1 pT346							
p21							
p27-Kip-1							
p27 pT198							
PAICS							
PAK1							
Paxillin							
Pdcd4							
PEA-15							
PEA-15 pS116							

H1299 Dyn1 KO + Dyn1^{WT}-EGFP and either Dyn1 KO or Dyn1 KO + Dyn1$^{S774A/S778A}$-EGFP or Dyn1 KO + Dyn1$^{S774D/S778D}$-EGFP respectfully (Table 1). No proteins were significantly different between H1299 parental and Dyn1 KO + Dyn1^{WT}-EGFP tumors. Interestingly, we observed few differences between either parental or Dyn1 KO + Dyn1^{WT}-EGFP cells and those expressing Dyn1 KO + Dyn1$^{S774A/S778A}$-EGFP. These data suggest that Dyn1 might be activated in tumor cells *in vivo*. Instead we observed greater differences between parental and Dyn1 KO cells or cells expressing Dyn1 KO + Dyn1$^{S774D/S778D}$-EGFP, a phosphomimic mutant described to be constitutively inactive.

In an attempt to identify which proteins are consistently affected by changes in Dyn1 expression and functional status we looked for proteins that appear in at least two different comparison conditions. We found fourteen of the fifty-four proteins in the H1299 parental versus Dyn1 KO condition that also showed up in at least one other condition (Table 2). Furthermore, seven more proteins were found in both the H1299 parental versus Dyn1 KO + Dyn1$^{S774D/S778D}$-EGFP and H1299 Dyn1 KO + Dyn1^{WT}-EGFP versus Dyn1 KO + Dyn1$^{S774D/S778D}$-EGFP tumors (Table 2). Additionally, changes in either expression or functional status were consistent across the different Dyn1 conditions (Table 2).

We next asked if any of these eighteen proteins have been previously linked to endocytosis or certain cancer properties. The findings are summarized in Table 3. Interestingly, several of the proteins such as ATM, Shc, and c-Kit have been previously shown to interact with endocytic adaptor proteins [169-171]. Additionally, many of the

Table 2: Expression Level Changes in Key RPPA Analysis Proteins

	Parental vs.			Dyn1 KO + Dyn1 WT vs.			Parental vs. Dyn1 WT
Protein Name	**Dyn1 KO (n=2)**	**Dyn1 KO + Dyn1 DD**	**Dyn1 KO + Dyn1 AA**	**Dyn1 KO**	**Dyn1 KO + Dyn1 DD**	**Dyn1 KO + Dyn1 AA**	
ATM							
c-Kit							
MSH6							
Rictor_pT1135							
Src_pY527							
p27_pT198							
PKCa							
Shc_pY317							
Smad1							
TIM-3							
IR-b							
FAK							
MAPK_pT202_Y204							
NDRG1_pT346							
Bax							
GSK3α/β_pS21_pS9							
IGFRb							
NF-κB-p65_pS536							
p90RSK_pT573							
PAR							
RPA32_pS4_pS8							

proteins appear to be regulated by Akt or regulate Akt [160, 172-174]. Moreover, several of the proteins such as PKCa, Smad1, and Shc have been previously shown to interact with either Dyn2 or Dyn1 directly [175-179]. Finally using the STRING database [180] all of these proteins except Tim-3, which is normally only found in immune cells [181] have been shown to interact in some way and Akt is a main hub in these interactions (Figure 6). Together these results suggest that altering Dyn1 in a xenograft model changes the expression of signaling molecules critical for cell survival and growth. Elucidating the Dyn1 dependent mechanism of these changes will be the next important step in understanding the role of Dyn1 in cancer progression.

Cargo-selectivity of Dyn1 dependent CME

To further understand the role of Dyn1 expression in tumorigenesis we asked: Can effects of Dyn1 on tumor growth be correlated with changes in expression of proteins at the PM? Previous work from our lab discovered that Dyn1 but not Dyn2, specifically regulates TRAIL-induced apoptosis through active CME [163]. TNF-related apoptosis-inducing ligand (TRAIL) is a protein ligand that binds to cell surface death receptors (DR) and induces apoptosis. Consequently, TRAIL has been considered as a target of several cancer therapies. Inhibition of CME by siRNA-mediated knockdown of clathrin or AP2 sensitized A549 cells, which are highly resistant to TRAIL-induced cell death, to TRAIL-induced apoptosis. Unexpectedly, siRNA knockdown of Dyn1 but not Dyn2 had the same effect. These results

Table 3: Proteins from RPPA screen and possible links to Endocytosis or Cancer	
Dyn1 KO & Dyn1 KO + Dyn1 DD tumors	
Protein Name	**Possible Links to Endocytosis or Cancer**
ATM	Has been shown to interact with APPL proteins [169], β-adaptin [182], and regulate GLUT1 uptake [183].
c-Kit	Many adaptor proteins such as CALM [170] and HIP1 [184] play a critical role in signaling cellular transport of KIT. Shown to traffic in a PI3K, clathrin, and Ca^{2+} dependent manner [185].
MSH6	Component of the post-replicative DNA mismatch repair system (MMR). Mutations in MSH6 leads to increased risk of Colorectal Cancer caused by Lynch syndrome [186].
Rictor_pT1135	Following growth factor stimulation (specifically IGF-1) and activation of the PI3K/mTOR/Akt pathway, Rictor is specifically phosphorylated on the Thr-1135 site [172].
Src_pY527	Phosphorylation at Y527 by CSK is required to turn off Src catalytic activity [187]. Src phosphorylation of Dyn 1 at T231 and T597 is required for GPCR uptake [175].
p27_pT198	T198 is of primary importance for the regulation of protein stability and for control of cell motility [188]. T198 phosphorylation of p27kip1 is Akt-dependent in breast cancer [174].
PKCa	Phosphorylation of Dynamin 1 on S795 by PKC blocks its association with phospholipids [178].
Shc_pY317	Phosphorylation of Y317 has been implicated in Grb2 binding and activation of the Ras pathway [189]. Shc mediates ligand-induced internalization of epidermal growth factor receptors, through Shc-AP2 complex formation [171]. Dyn1 associates with Shc and becomes tyrosine phosphorylated in response to insulin [190].
Smad1	Dyn2 allows for modulation of basal and ligand-dependent Smad signaling capacity. Possible Dyn1 regulation has never been studied [177].
TIM-3	An immune checkpoint receptor that limits the duration and magnitude of Th1 and Tc1 T-cell responses. Approximately 1/3 of NSCLC patients have Tim-3 expressing $CD8^{+}$ tumor-infiltrating lymphocytes [181].
IR-b	A dominant-interfering mutant of Dyn 1 (K44A) selectively attenuates specific insulin receptor signal transduction pathways [176]
Dyn1 KO + Dyn1 DD tumors Only	
Protein Name	**Possible Links to Endocytosis or Cancer**
Bax	Dynamin-related protein Drp1 is required for the pro- apoptotic protein translocation to mitochondria a crucial step in DNA damage-mediated apoptosis [179].
GSK3α/β_pS21_pS9	Crosstalk between Akt/GSK3β signaling and dynamin-1 regulates clathrin-mediated endocytosis [160].
IGFRb	Knockdown of Dyn2, prevented IGFR dephosphorylation although Dyn1 has not been tested [191]. Has been suggested to traffic in a Dyn2 dependent fast endophilin-mediated endocytosis (FEME) pathway [42].
NF-κB-p65_pS536	p53 expression leads to the activation of $p90^{RSK}$, which phosphorylates p65 at S536 resulting in increased nuclear translocation and accumulation of p65 [192].
$p90^{RSK}$_pT573	EGFR activation at the PM versus endosomes resulted in differential spatio-temporal dynamics of phosphorylated ERK, which caused differential activation of RSK [193]. In AKT-impaired cells, EGFR accumulates in early endosomes, resulting in increased activation of RSK [173, 194].
PARP1	This modification follows DNA damages and appears as an obligatory step in a detection/signaling pathway leading to the reparation of DNA strand breaks, which is often disregulated in Cancer [195].
RPA32_pS4_pS8	Phosphorylation at these sites occurs in response to DNA damage [196].

led to the surprising finding that Dyn1 but not Dyn2 was required for CME of TRAIL-DR complexes. Whereas the opposite was true for CME of TfnR [163].

To identify other CME cargo that might be regulated in a Dyn1 specific manner, we applied a quantitative proteomic approach. Surface expression of Dyn1 specific cargo receptors would be expected to be increased in Dyn1-CME deficient cells compared to WT. To analyze purified PM fractions from WT and Dyn1 KO cells, the cells were labeled using stable isotope labeling with amino acids in cell culture (SILAC). First, to purify PM, biotinylated Concanavalin A (ConA), a lectin that binds specifically to mannose and can be used to bind the sugar on proteins, was bound to streptavidin magnetic beads. Whole cells were then added to the ConA magnetic beads and allowed to bind. Cells were next gently lysed by freeze thaw so as not to break the bond between the PM proteins and the ConA coated beads. The PM was then eluted from the beads by washing two times with methyl α-manno-pyranoside (Figure 7A).

For differential proteomic analysis, cells were labeled for SILAC. H1299 parental and Dyn1 KO cells were either cultured with “light media” (Arg-0/Lys-0) or “heavy media” (Arg-6/Lys-6) until 95% incorporation of the heavy amino acids were achieved. The PM from each condition was then purified as described above and H1299 “heavy” and H1299 Dyn1 KO “light” samples and H1299 “light” and H1299 Dyn1 KO “heavy” were mixed together. Mass spectrometry was used to determine changes in protein concentrations between the PM of H1299 cells and H1299 Dyn1 KO cells (Figure 7B).

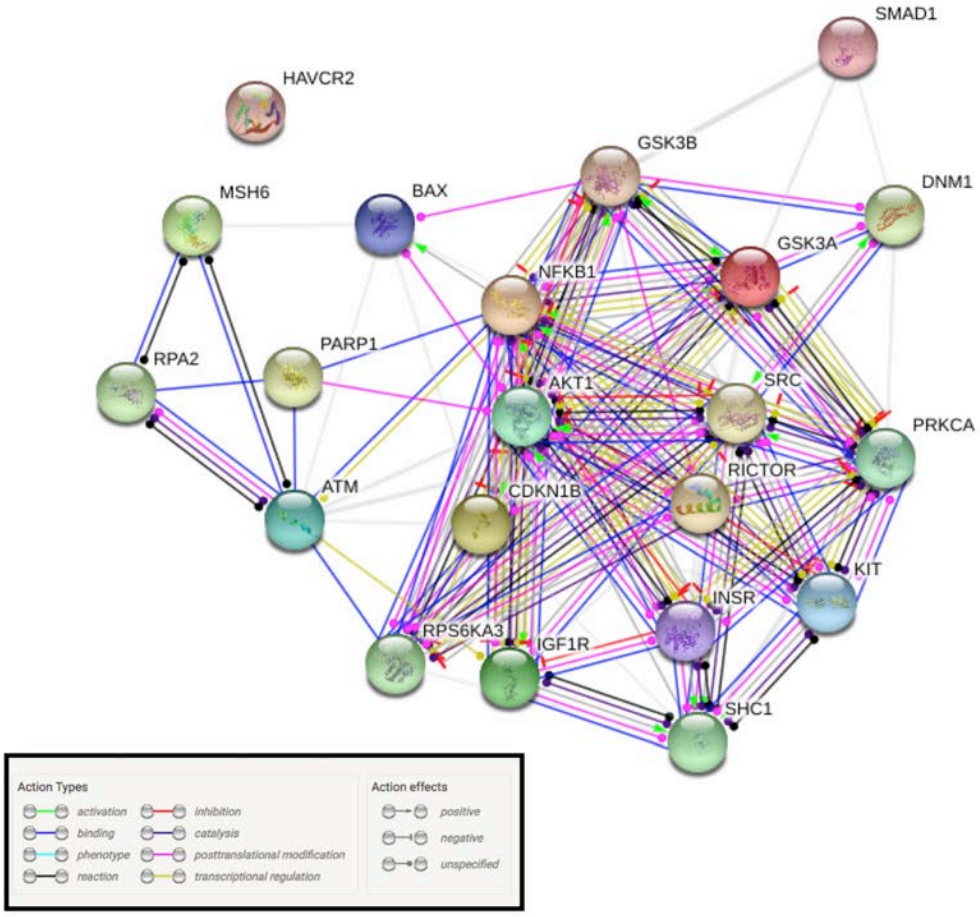

Figure 6: A schematic created using the STRING database [180] representing known interactions between proteins discovered in the RPPA assay comparing H1299 parental and Dyn1 KO + Dyn1$^{S774D/S778D}$-EGFP tumors.

After optimization by western blotting, we confirmed the purity of the PM by looking at the presence of PM proteins such as Na^+/K^+ ATPase or EGFR, the early endosomal protein EEA1, a Golgi protein GM130, and the cytosolic protein GAPDH. We would expect to see all five proteins in the whole cell lysates, while we would expect to see GAPDH, EEA1, and GM130 in the unbound fractions, since they are found inside the cell and are unable to bind to the ConA magnetic beads, while we would expect to see Na^+/K^+ ATPase and EGFR in the elution fractions, since they are found on the PM and are able to bind to the ConA magnetic beads. Indeed, as expected GAPDH and EEA1 were detected in the unbound fractions but depleted from the bound fraction, whereas Na^+/K^+ ATPase and EGFR were enriched in the elution fractions (Figure 8A and B). However, the PM fraction was contaminated by Golgi (Figure 8B). We next tested whether expression of surface receptors changed in H1299 Dyn1 KO cells compared to H1299 cells by measuring changes in expression of Na^+/K^+ ATPase and TfnR (Figure 8C). Both proteins show enrichment compared to the whole cell lysate. Furthermore, WT and Dyn1 KO cells show quantifiable differences in protein expression (Figure 8D). These results indicate that Dyn1 KO does change the composition of cell surface receptors.

After confirmation of the ability to enrich the PM and to measure changes in PM expression resulting from Dyn1 KO, we scaled up the procedure and performed SILAC and mass spectrometry on two different sets of samples: 1. H1299 “heavy” mixed with H1299 Dyn1 KO “light” and 2. H1299 “light” mixed with H1299 Dyn1 KO “heavy”. From these

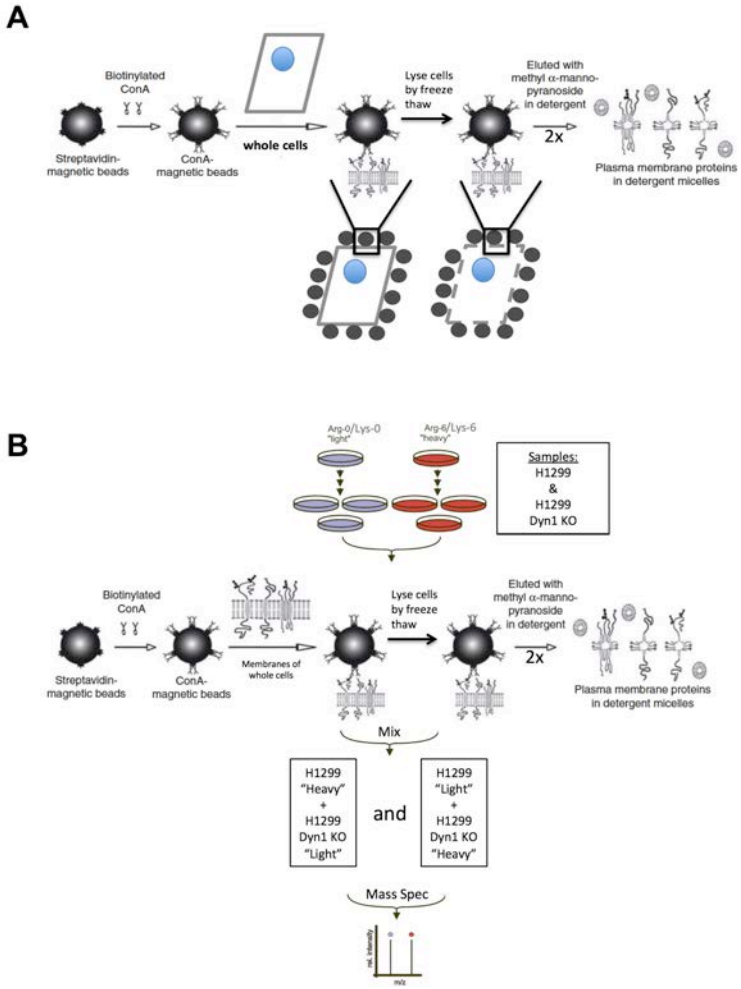

Figure 7: Schematic of **A)** Plasma membrane isolation using magnetic biotinynlated ConA beads and B) Experimental design of SILAC experiments comparing PM protein expression between H1299 and H1299 Dyn1 KO cells.

samples we have obtained the first round of "hits" (Tables 4 and 5). However, the experiment requires further optimization. The "hits" obtained in the first experiment contained very few transmembrane (TM) proteins (around 11% of total proteins). Further optimization is needed for better enrichment of the plasma membrane. Increased sample volume in order to increase sensitivity might improve TM protein detection. Furthermore, phase separation using the detergent TX114 might improve TM protein enrichment.

Once optimized, the experiment can be repeated at least two more times to enable statistical analysis, which will identify "hits" for future study. To confirm differential expression of the "hits" between WT and Dyn1 KO, "hits" will be validated using PM purification and western blot.

Discussion

Endocytosis of cell surface receptors can potentially control many activities related to cancer cell proliferation and growth, including nutrient acquisition, cell–cell and cell–matrix adhesion, and receptor signaling. Moreover, many components of the endocytic machinery are mutated or have altered expression in a number of cancers [12, 116, 150]. Furthermore, specific components of CME are altered in cancer cells [116]. However, changes in Dyn1 expression levels in cancer have yet to be reported and a possible role for Dyn1 in cancer progression has never been explored. Here, we sought support for the hypothesis that

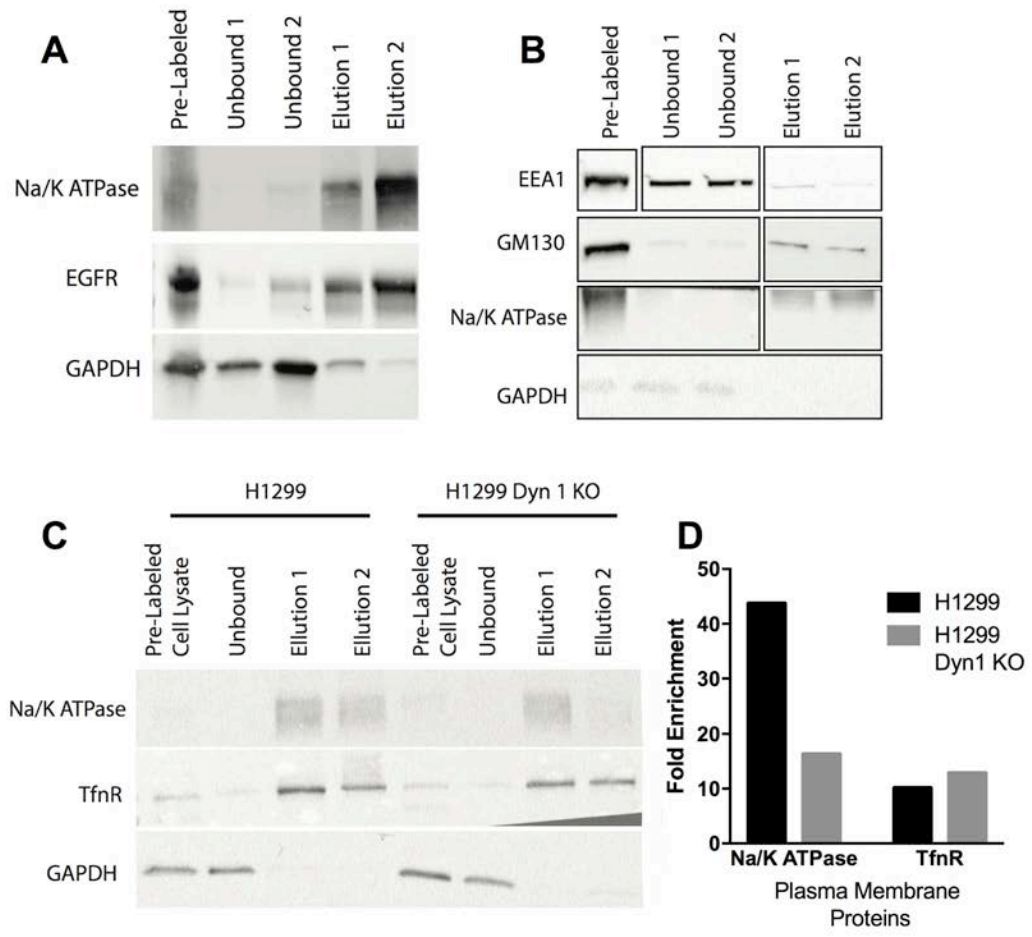

Figure 8: Optimization of the plasma membrane (PM) isolation technique. A) PM isolation of H1299 cells probed for plasma membrane markers Na+/K+ ATPase and EGFR, which will also be present in endosomes, as well as a cytosolic marker GAPDH. B) PM isolation of H1299 cells probed for EEA1 (and Early Endosome marker), GM130 (A Golgi marker), Na+/K+ ATPase, and GAPDH. **C)** PM isolation of H1299 parental and Dyn1 KO cells probed for Na+/K+ ATPase, TfnR, and GAPDH. The same protein concentration was loaded for each condition. D) Quantification of Na+/K+ ATPase and TfnR in H1299 parental versus H1299 Dyn1 KO cells, plotted as fold enrichment from the pre-labeled cell lysate (n=1).

changes in Dyn1 expression in cancer alters CME, which leads to alterations in critical cellular behaviors, such as proliferation and growth important for tumorigenesis.

We have shown that Dyn1 protein expression alone does not determine the activity of Dyn1 in regulating CME in cancer cells. In addition, phosphorylation/dephosphorylation is required to regulate the activity of Dyn1 in cancer cells. Furthermore, we have shown that there are probably multiple posttranslational regulation mechanisms that affect Dyn1 activity since only 3 of 5 cell lines tested responded to GSK3β inhibition, which is only one mechanism responsible for phosphorylating/dephosporylating Dyn1. Looking specifically at the role of Dyn1 in endocytic trafficking we showed that while short-term depletion of Dyn1 alters endocytic trafficking, cells were able to compensate when Dyn1 is deleted. Together these results suggest that Dyn1 is highly regulated by multiple mechanisms. Furthermore, although previous work has suggested that Dyn1 expression might cause changes in early endocytic trafficking [160, 197] we found no evidence of this in cells with long-term removal of Dyn1. This difference in results could be due to differences in image acquisition. Previous work used TIRF microscopy to look at early endocytic trafficking while this work used epifluorescence.

Crosstalk between Dyn1 and cancer signaling pathways

CME controls signaling downstream of mitogenic receptors such as EGFR [166]; therefore, we examined the role of Dyn1 expression in cancer cell proliferation. We have

shown that Dyn1 expression alters the proliferation rates of cancer cells but that Dyn1 effects on proliferation are not due to changes in the cell cycle. We also have shown that Dyn1 expression alters growth *in vitro* and *in vivo* although we observed heterogeneity in tumor size across experiments, which might be due to clonal variation from CRISPR or technical issues such as low cell viability or growth stage, not enough cells injected, or the cell's time in culture. Future work will need to be done to determine the cause of this heterogeneity or if a better model system exists to explore the role of Dyn1 in tumor growth before the experiment can be repeated.

Although endocytosis and cell signaling were previously thought to be separate processes, crosstalk between endocytosis and signaling has now been shown [198, 199]. Therefore, this work set out to better understand the relationship between Dyn1 and known signaling pathways in cancer using RPPA analysis. We identified 14 proteins that had significantly different expression and/or phosphorylation levels between H1299 parental and Dyn1 KO tumors. Additionally, we discovered another 7 proteins that had differential expression and/or phosphorylation levels in the Dyn1 KO + Dyn1$^{S774D/S778D}$-EGFP tumors compared to parental and the WT rescue conditions while parental and H1299 Dyn1 KO + Dyn1^{WT}-EGFP had no significant differences suggesting that Dyn1 WT expression was able to rescue Dyn1 function back to parental levels. Several of these proteins have been reported to interact with known components of the endocytic machinery and several others appear to play a role in Akt signaling. However the relationship to Akt signaling may be cell type

dependent given that the H1299 cell line is an Akt driven tumor cell line. Further work is necessary to directly explore the relationship between Dyn1 and the proteins discovered in the RPPA assay. That many signaling molecules important for cell survival and growth were identified suggests a functional link.

Cargo-selectivity of Dyn1 dependent CME

A recent study has shown that Dyn1 but not Dyn2 activity regulates TRAIL-induced apoptosis through active CME [163]. Using SILAC our work set out to explore if the effects of Dyn1 on tumor growth can be correlated with changes in expression of other proteins at the PM using a quantitative proteomic approach. Although we successfully purified the PM using biotinylated ConA magnetic beads, further optimization is needed at the SILAC step. The "hits" obtained from SILAC contained only 11% TM proteins, which is significantly lower than expected. Better enrichment of the plasma membrane might be needed. Using techniques like phase separation using the detergent TX114 might be one way to improve TM protein enrichment. Furthermore, increased sample volume to increase sensitivity might improve TM protein detection.

Together, our results suggest that dynamic regulation of signaling molecules and surface expression of important cancer molecules by Dyn1 may in some cases, contribute to cancer cell properties such as proliferation and growth. Although more work is needed to determine the mechanisms responsible.

Materials and Methods:

Cell lines and culture

All NSCLC lines used in this study (H157, H1299, H2073, Hcc827, A549) were obtained from the Hamon Cancer Center Collection (University of Texas Southwestern Medical Center) and maintained in RPMI-1640 (Life Technologies) supplemented with 5% fetal calf serum. All cell lines were cultured at 37°C in a humidified atmosphere containing 5% CO_2 and 95% air. All cell lines have been DNA fingerprinted using the PowerPlex 1.2 kit (Promega) and are mycoplasma free using the e-Myco kit (Boca Scientific). Culture media were purchased from Life Technologies.

Generation of dynamin-1 KO H1299 cell lines by CRISPR-Cas9n and reconstitution with Dyn1-EGFP constructs

Genome editing of H1299 cells was performed using a double-nicking strategy to knockout (KO) endogenous dynamin-1 as described previously [160]. Briefly, two pairs of 20-bp-long dynamin-1 sgRNAs (single guide) were designed using the CRISPR design tool available at www.genome-engineering.org/crispr [200]. The guide RNA pairs (+ and − strands) were cloned into a bicistronic expression vector (pX335) containing a human codon-optimized Cas9n and necessary RNA components (Addgene). Top two double nickase "hits" targeting exon 1 of human dynamin-1 were chosen for cloning into pX335 vector.

The single-guide RNAs (sgRNAs) in the pX335 vector (1 μg each for a sgRNA pair) were mixed with pmaxGFP plasmid (0.2 μg; Lonza) and co-transfected into H1299 cells using lipofectamine 2000 transfection reagent (Life Technologies). Forty-eight hours post-transfection, the cells were trypsinized, washed with PBS and resuspended in PBS containing 2% serum. GFP-positive cells were single-cell sorted by FACS (The Moody Foundation Flow Cytometry Facility, UT Southwestern Medical Center, Dallas, TX) into a 96-well plate format into RPMI containing 5% FBS. Single clones were expanded and screened for dynamin-1 expression by Western blotting using the anti-dynamin-1 rabbit monoclonal antibody (EP772Y, Abcam).

Stable reconstitution with WT Dyn1-EGFP, SS774/8AA Dyn1-EGFP, and SS774/8DD Dyn1 EGFP fusion proteins in H1299 Dyn1 KO cells (Clone B22) was performed as previously described [168]. Briefly, WT Dyn1 containing an N-terminal HA tag and C-terminal EGFP fusion protein were cloned into pMIEG3 retroviral vector. Virus was produced in 293T packaging cells and the retroviral supernatant was used to infect H1299 Dyn1 KO cells. Cells were collected 48 h post-infection and FACS sorted for low expression levels based on GFP intensity. The S774A, SS774/8AA, and S774/8DD mutations were introduced into the above retroviral vector via site directed mutagenesis and similarly infected and sorted for comparable expression levels.

Antibodies and reagents

Anti-TfnR (HTR-D65) monoclonal antibody was produced in hybridoma as in [108]. Anti-Dyn-1 (ab52852) and anti-Dyn-1 phospho-S774 (ab55324) were purchased from Abcam. Anti-Dyn-2 (sc-64000) antibodies was purchased from Santa Cruz Biotechnology. APPL1 (#3858), was purchased from Cell Signaling. Anti-EEA1 antibody (#610457) was obtained from BD Pharmingen™. Horseradish peroxidase (HRP)- and AlexaFluor®-conjugated antibodies were purchased from Life Technologies. OPD (#P1536) and Concanavalin A (C2010) were obtained from Sigma-Aldrich. Streptavidin-POD was purchased from Roche. Fluoromount G and PFA were purchased from Electron Microscopy Sciences.

TfnR internalization

Assays were performed in PBS^{4+} (PBS supplemented with 1 mM $MgCl_2$, 1 mM $CaCl_2$, 5 mM glucose, and 0.2% BSA) using the receptor-specific monoclonal antibodie D65 as a ligand for TfnR exactly as described in [48]. Briefly, 2.8×10^4 cells/well seeded on collagen coated 96-well plates and cultured overnight. For assays, cells were washed with PBS^{4+}, and then incubated for the indicated times at 37°C in PBS^{4+}-containing 4 μg/mL of D65 before being rapidly cooled on ice, washed with cold PBS^{4+} and then stripped of remaining surface-bound mAbs by an acid wash (5 × 2 min 0.2 M acetic acid, 0.2 M NaCl, pH 2.5). Cells were then fixed in 4% PFA, permeabilized with 0.1% Triton-X100 and internalized mAbs detected and quantified using an HRP-conjugated secondary antibody and

OPD detection. The absorbance was read at 490 nm using a Biotek Synergy H1 Hybrid Reader. Well-to-well variability in cell number was accounted for by normalizing the reading at 490 nm with a bicinchoninic acid (BCA) readout at 560 nm (Biotek Synergy H1 Hybrid Reader). The fraction of internalized ligand was calculated relative to the initial total surface bound ligand at 4°C (without the acid wash step) measured in parallel for all the assays.

For Tfn internalization using the GSK3β inhibitor CHIR-99021 (Sigma), cells were initially pre-incubated in the absence (i.e., control) or presence of the indicated inhibitor (10 μM) for 30 min at 37°C, Tfn internalization assays were then performed as described above in the continual presence of 10 μM CHIR-99021. Percentage of Tfn uptake was calculated relative to the initial total surface-bound ligand at 4°C for all the assays.

For *siRNA-mediated* inhibition of endocytosis, RNAiMAX transfection reagent (Life Technologies) was used to deliver siRNA targeting: dynamin-1 (5′-GGCUUACAUGAACACCAACCACGAA-3′) or dynamin-2 (1:1 mixture of Dyn2_1: 5′-CCGAAUCAAUCGCAUCUUCUU-3′ and Dyn2_2: 5′-GACAUGAUCCUGCAGUUCAUU-3′) to NSCLC cells, following the manufacturer's instructions. Transfection was performed at day 1 and day 3 after plating, and experiments were performed at day 5. The AllStars Negative siRNA non-targeting sequence was purchased from Qiagen.

Immunofluorescence

H1299 cells, some expressing enhanced green fluorescent protein (EGFP) fused to the C-terminus of dynamin 1 (Dyn1-eGFP), were grown overnight on glass cover slips and then washed with PBS and fixed in 4% PFA in PBS for 10 min at room temperature, permeabilized with 0.1% Triton X-100 for 2 min and further blocked with Q-PBS (0.01% saponin, 2% BSA, 0.1% lysine, pH 7.4) for 1 h. After three washes with PBS, cells were incubated with the indicated primary antibody in Q-PBS for 1 h using the recommended dilution. Cells were washed three times with PBS and further incubated with suitable AlexaFluor®-labeled secondary antibodies for 1 h. After three additional washes with PBS, samples were mounted on Fluoromount G on glass slides and examined using either 60× 1.49 NA objectives (Nikon) mounted on an epifluorescence Ti-Eclipse inverted microscope.

Proliferation

Measurement of proliferation was performed using the CCK-8 Counting Kit (Dojindo), which measures dehydrogenase activity in viable cells. Briefly, 2×10^3 cells/well of each cell line were dispensed, in triplicate, in a 96-well plate. 24, 48, 72, and 96 h later the plates analyzed according to the manufacturer's instructions. Data presented are from the 72 h time point.

Cell Cycle Analysis

Cells were harvested and fixed in 1ml ice cold 80% ethanol and incubated for 30min. Samples were subsequently spun down on a table top centrifuge 3500rpm 3 min and washed twice with PBS. Cells were resuspended in 1ml fresh 0.1% TritonX-100, 1μg/ml DAPI (Invitrogen D1306) and incubated for 30 min at room temperature. Samples were analyzed with the LSRFortessa flow cytometer (BD Biosciences). Data was analyzed with FlowJo (FlowJo, LLC).

Growth in Soft Agar

Anchorage-independent growth in soft agar was performed by seeding cells in 0.4% noble agar on top of a 1% layer. After 3 weeks, cells were fixed with 4% PFA in PBS for 1 h at 37°C. Cells were then stained with DAPI in PBS (1/500) for 1 h at 37°C and extensively washed (2x for 30 mins at RT) with PBS to remove excess stain. Cell nuclei were visualized using a 10× air objective mounted on a T*i*-Eclipse inverted microscope (Nikon) driven by NIS Elements V4.13 software and quantified using the "Object Count" feature of NIS Elements software.

Mouse Experiments

Mouse experiments were performed in collaboration with Boning Gao and Hyunsil Park at UT Southwestern (Dallas, Tx). Fresh cells were thawed and allowed to grow in culture for 3 to 4 passages before harvesting for mouse injections. Cells were detached from

the plate with 0.05% trypsin at 37°C. After 80% of the cells were detached, trypsinization was stopped by adding fresh media. Cells were counted and spun down at 1000rpm for 2 min and resuspended in PBS at 1 $x10^7$ cells/mL. Mice were submitted to hair clipping and antisepsis with Povidine® (polyvinylpyrrolidone) and alcohol pad (alternate 3X) in the flank area. One million tumor cells in 200 µl PBS were injected in subcutaneous area using a 23G needle. Tumor volume was measured every 3-4 days using digital calipers.

Reverse Phase Protein Array (RPPA)

This work was performed by the RPPA core facility at MD Anderson (Houston, Tx). Protein lysates were prepared from frozen tumor-derived tissue acquired from the mouse experiments above. Ice-cold lysis buffer (1% Triton X-100, 50 mM HEPES, pH 7.4, 150 mM NalL, 1.5 mM $MgCl_2$, 1 mM EGTA, 100 mM NaF, 10 mM Na pyrophosphate, 1 mM NA_3VO_4, 10% glycerol, containing freshly added protease and phosphatase inhibitors (Roche)) was added to a small piece of tumor tissue and homogenized with a hand homogenizer for 8 seconds on ice. The samples were then spun at 14,000 rpm for 10 min at 4°C. The supernatant was transferred to clean tubes and the protein concentration was adjusted to 1.5µg/µl using the lysis buffer.

Cellular proteins were denatured by 1% SDS (with Beta-mercaptoethanol) and diluted in five 2-fold serial dilutions in dilution lysis buffer. Serial diluted lysates were arrayed on nitrocellulose-coated slides (Grace Bio Lab) by Aushon 2470 Arrayer (Aushon BioSystems).

A total of 5808 array spots were arranged on each slide including the spots corresponding to serial diluted: 1) “Standard Lysates”; 2) positive and negative controls prepared from mixed cell lysates or dilution buffer, respectively. Each slide was probed with a validated primary antibody plus a biotin-conjugated secondary antibody. Only antibodies with a Pearson correlation coefficient between RPPA and western blotting of greater than 0.7 were used for RPPA. Antibodies with a single or dominant band on western blotting were further assessed by direct comparison to RPPA using cell lines with differential protein expression or modulated with ligands/inhibitors or siRNA for phospho- or structural proteins, respectively. The signal obtained was amplified using a Dako Cytomation–Catalyzed system (Dako) and visualized by DAB colorimetric reaction. The slides were scanned, analyzed, and quantified using customized software to generate spot intensity. Each dilution curve was fitted with a logistic model (“Supercurve Fitting” developed by the Department of Bioinformatics and Computational Biology in MD Anderson Cancer Center, “http://bioinformatics.mdanderson.org/OOMPA”). This fits a single curve using all the samples (i.e., dilution series) on a slide with the signal intensity as the response variable and the dilution steps are independent variable. The fitted curve is plotted with the signal intensities both observed and fitted on the y-axis and the log2-concentration of proteins on the-axis for diagnostic purposes. The protein concentrations of each set of slides were then normalized for protein loading. Correction factor was calculated by: 1) median-centering

across samples of all antibody experiments; and 2) median-centering across antibodies for each sample.

Plasma Membrane Isolation

The plasma membrane of H1299 and H1299 Dyn1 KO cells were isolated as previously described [201] with slight modification. Briefly, ConA was immobilized onto streptavidin magnetic beads by binding biotinylated ConA to them. First, beads were washed and resuspended with PBS and biotinylated ConA (2.5mg/mL). This suspension was mixed on a rocker at RT for 1 h to allow binding of biotinylated ConA to streptavidin. The beads were then washed with PBS, followed by PBS containing 1% TritonX-100, and three times PBS then resuspended in PBS.

Cells from three 15 cm dishes per condition were detached using 5mM EDTA in PBS. Once cells had detached the cells were washed three times and resuspended in PBS. The cells were added to the streptavidin magnetic beads, prepared as described above, and mixed on a rocker at 4°C for 1 h. Cells were lysed in 0.25% BSA and excess ConA (0.1 mg/mL) by three cycles of freezing/thawing in liquid N_2 and the lysate was washed three times with 500mM NaCl in PBS. The plasma membrane was eluted from the magnetic beads by two consecutive incubations with 0.25M methyl-α-mannoside and 0.5% CHAPS at RT for 10 mins.

SILAC

This work was performed with the help of the Mass Spectrometry Core at UT Southwestern (Dallas, Tx). H1299 parental and KO cells were cultured in either “heavy” or “light” media until 95% incorporation of Arg/Lys was reached about 2 weeks for H1299 cells. Plasma membrane isolation was performed as stated above. “Heavy” and “light” samples from each condition were mixed and then run 5-10mm into a resolving gel, fixed, coomassie stained, and diced into 1mm cubes.

Gel bands were digested overnight with trypsin (Promega) following reduction and alkylation with DTT and iodoacetamide (Sigma–Aldrich). Following solid-phase extraction cleanup with Oasis HLB plates (Waters), the resulting samples were analyzed by LC/MS/MS using an Orbitrap Elite (for label incorporation and mixing test) or Orbitrap Fusion Lumos mass spectrometer (Thermo Electron) coupled to an Ultimate 3000 RSLC-Nano liquid chromatography system (Dionex) with an Easy Spray column (Thermo). Peptides were eluted with a gradient from 1-28% buffer B over 60 min. Buffer A contained 2% (v/v) acetonitrile (ACN) and 0.1% formic acid in water, and buffer B contained 80% (v/v) ACN, 10% (v/v) trifluoroethanol, and 0.08% formic acid in water. The mass spectrometer acquired up to 10 MS/MS spectra for each full spectrum acquired.

For testing heavy isotope label incorporation, raw MS data files were converted to a peak list format and analyzed using the central proteomics facilities pipeline (CPFP), version 2.0.3 [202, 203]. Peptide identification was performed using the X!Tandem [204] and open

MS search algorithm (OMSSA) [205] search engines against the human protein database from Uniprot, with stable contaminants and reversed decoy sequences appended [206]. Fragment and precursor tolerances of 20 ppm and 0.5 Da were specified, and three missed cleavages were allowed. Carbamidomethylation of Cys was set as a fixed modification, with oxidation of Met, Lys 13C(6), and Arg 13C(6_15N(4) set as variable modifications. Label incorporation was considered to be complete if the percentage of heavy labelled peptides was at least 95% of the total number of non-contaminant peptides.

A mixing test was performed prior to cell treatment in order to determine the proper mixing ratio to obtain a 1:1 mixture of heavy to light cells prior to treatment. Based on the median heavy to light protein ratio for the proteins observed in the mixing test sample, mixing ratios were adjusted accordingly.

SILAC data were analyzed with MaxQuant 1.5.0.30. Lys6 and Arg10 were set as labels, with requantify selected. Cysteine carbamidomethylation was set as a fixed modification and acetylation of protein N-termini and methionine oxidation were set as variable modifications. The enzyme specificity was set to trypsin with three missed cleavages allowed. The first search was at 20 ppm and the main search at 4.5 ppm, with PSM FDR was set to 1%.

Table 4: H1299 "Heavy" & H1299 Dyn1 KO "Light" SILAC Results

Protein names	Gene names	Ratio H/L	Ratio H/L normalized	log (Ratio H/L)	log (Ratio H/L normalized)
Hornerin	HRNR	0.033763	0.027507	-4.88841309	-5.184057386
Protein S100-A8;Protein S100-A8, N-terminally processed	S100A8	0.069086	0.05921	-3.855462806	-4.078015336
Cullin-3	CUL3	0.091729	0.08832	-3.446478278	-3.501116018
Nance-Horan syndrome protein	NHS	0.094542	0.074478	-3.402900805	-3.747041858
Desmoplakin	DSP	0.10481	0.08774	-3.254151723	-3.510621483
Lactotransferrin;Lactoferricin-H;Kaliocin-1;Lactoferroxin-A;Lactoferroxin-B;Lactoferroxin-C	LTF	0.10564	0.095008	-3.242771888	-3.395807191
Alpha-amylase 1;Alpha-amylase 2B;Pancreatic alpha-amylase	AMY1B; AMY1A; AMY2B; AMY2A	0.15771	0.12826	-2.664653954	-2.962856783
SH3 domain-containing kinase-binding protein 1	SH3KBP1	0.46866	0.38091	-1.093386428	-1.392477932
mRNA cap guanine-N7 methyltransferase	RNMT	0.47684	0.4171	-1.068422833	-1.261534783
Melanoma-associated antigen D2	MAGED2	0.48762	0.41056	-1.036170795	-1.284335019
CD2-associated protein	CD2AP	0.50175	0.4419	-0.994959383	-1.178208164
Serine/threonine-protein kinase PAK 2;PAK-2p27;PAK-2p34	PAK2	0.51828	0.49552	-0.948196373	-1.012984807
Septin-9	SEP9	0.55091	0.46389	-0.860111444	-1.108145348
Serpin H1	SERPINH1	0.55556	0.45252	-0.847985365	-1.143946539
Putative protein FAM10A4;Hsc70-interacting protein;Putative protein FAM10A5	ST13; ST13P4; ST13P5	0.61424	0.51053	-0.70312563	-0.969932355
PRKC apoptosis WT1 regulator protein	PAWR	0.62647	0.5443	-0.674682671	-0.877526059
Apoptosis inhibitor 5	API5	0.63979	0.55893	-0.644329652	-0.839260483
Ataxin-2-like protein	ATXN2L	0.65162	0.53412	-0.61789721	-0.904764188
Kinesin-like protein KIF2C	KIF2C	0.65931	0.55087	-0.600971131	-0.860216198
Protein FAM114A2	FAM114A2	0.65974	0.52435	-0.600030517	-0.931397973
Plasminogen activator inhibitor 1	SERPINE1	0.67186	0.59107	-0.573767455	-0.758599097
Signal recognition particle 54 kDa protein	SRP54	0.68515	0.55431	-0.545508223	-0.85123506
Leucine-rich repeat-containing protein 47	LRRC47	0.68591	0.61597	-0.543908806	-0.699068007
IQ motif and SEC7 domain-containing protein 2	IQSEC2	0.69313	0.66396	-0.528802132	-0.590831765
Tetratricopeptide repeat protein 1	TTC1	0.7142	0.60112	-0.485599961	-0.734275074
Integrin alpha-5;Integrin alpha-5 heavy chain;Integrin alpha-5 light chain	ITGA5	0.72093	0.62538	-0.47206891	-0.677195013
Adipocyte plasma membrane-associated protein	APMAP	0.72181	0.56959	-0.470308964	-0.812004277
Caldesmon	CALD1	0.7316	0.61547	-0.45087302	-0.700239558
Perilipin-3	PLIN3	0.73334	0.6286	-0.447445862	-0.669785823
Squalene synthase	FDFT1	0.73348	0.6308	-0.447170467	-0.664745435

26S proteasome non-ATPase regulatory subunit 2	PSMD2	0.73567	0.62678	-0.442869334	-0.673968949
ADP-ribosylation factor GTPase-activating protein 1	ARFGAP1	0.73674	0.62088	-0.440772522	-0.687613635
Large proline-rich protein BAG6	BAG6	0.74321	0.62035	-0.428158181	-0.688845685
Septin-7	SEP7	0.75554	0.60792	-0.404419958	-0.718046612
Glycogen phosphorylase, brain form	PYGB	0.76636	0.65069	-0.383905833	-0.619957713
Coatomer subunit beta	COPB2	0.77058	0.62098	-0.375983353	-0.687381291
Mitotic checkpoint protein BUB3	BUB3	0.78458	0.66952	-0.350007535	-0.578800942
Protein transport protein Sec23A	SEC23A	0.79364	0.63726	-0.333443355	-0.650045987
Nuclear pore complex protein Nup153	NUP153	0.79954	0.71491	-0.322757883	-0.484166462
Protein enabled homolog;Ena/VASP-like protein	ENAH;EVL	0.80254	0.64094	-0.317354794	-0.641738786
Actin-binding protein anillin	ANLN	0.80311	0.67142	-0.316330491	-0.574712583
RuvB-like 2	RUVBL2	0.8049	0.69359	-0.31311854	-0.527844997
60S ribosomal export protein NMD3	NMD3	0.80822	0.65276	-0.307180042	-0.615375441
Glycylpeptide N-tetradecanoyltransferase 1	NMT1	0.82291	0.66884	-0.28119344	-0.580266964
Lanosterol synthase	LSS	0.82438	0.68784	-0.27861859	-0.539855079
Eukaryotic translation initiation factor 2 subunit 3	EIF2S3	0.82854	0.72018	-0.271356746	-0.47357056
Talin-1	TLN1	0.83197	0.73593	-0.265396588	-0.442359548
Src substrate cortactin	CTTN	0.8382	0.72826	-0.254633573	-0.457474488
WD40 repeat-containing protein SMU1	SMU1	0.84525	0.71492	-0.242549984	-0.484146282
Peroxisomal multifunctional enzyme type 2;(3R)-hydroxyacyl-CoA dehydrogenase;Enoyl-CoA hydratase 2	HSD17B4	0.84573	0.72238	-0.24173094	-0.469170144
Cleavage stimulation factor subunit 3	CSTF3	0.84677	0.71741	-0.239957938	-0.47913024
HLA class I histocompatibility antigen, C; HLA class I histocompatibility antigen, C	HLA-C;HLA-B	0.8515	0.74169	-0.231921565	-0.431111777
Synaptic vesicle membrane protein VAT-1 homolog	VAT1	0.85354	0.70187	-0.22846933	-0.510724255
26S proteasome non-ATPase regulatory subunit 4	PSMD4	0.86091	0.72984	-0.21606567	-0.454347873
Elongation factor 1-gamma	EEF1G	0.86332	0.71074	-0.212032684	-0.492606199
Insulin-like growth factor 2 mRNA-binding protein 1	IGF2BP1	0.87026	0.7537	-0.200481608	-0.407937702
Transferrin receptor protein 1;Transferrin receptor protein 1, serum form	TFRC	0.87149	0.75925	-0.198443985	-0.397353091
Putative ribosomal RNA methyltransferase NOP2	NOP2	0.87565	0.74808	-0.191573759	-0.418735534
Nuclear pore complex protein Nup93	NUP93	0.87669	0.75146	-0.189861303	-0.412231783
Tumor protein D54	TPD52L2	0.87885	0.75661	-0.186311144	-0.40237825
Ribosomal L1 domain-containing protein 1	RSL1D1	0.88203	0.71976	-0.181100369	-0.474412167
Cold shock domain-containing protein E1	CSDE1	0.8826	0.73115	-0.180168348	-0.45176068
26S protease regulatory subunit 10B	PSMC6	0.88283	0.71867	-0.179792439	-0.476598631
Histone H1.5;Histone H1t;Histone H1.1;Histone H1.4;Histone H1.3	HIST1H1B; HIST1H1T; HIST1H1A; HIST1H1E; HIST1H1D	0.8873	0.77445	-0.172506126	-0.368755996

Ran GTPase-activating protein 1	RANGAP1	0.89712	0.75579	-0.15662712	-0.403942665
Splicing factor 3A subunit 2	SF3A2	0.89802	0.73239	-0.155180519	-0.449316002
RNA-binding protein 12	RBM12	0.8984	0.78513	-0.154570167	-0.348996543
Coatomer subunit gamma-1;Coatomer subunit gamma-2	COPG1;COPG2	0.901	0.72006	-0.150400989	-0.473810969
DnaJ homolog subfamily C member 10	DNAJC10	0.9018	0.73062	-0.149120585	-0.452806848
Nucleoprotein TPR	TPR	0.90288	0.74026	-0.14739384	-0.43389602
Importin subunit alpha-1	KPNA2	0.90935	0.80094	-0.137092414	-0.320233923
26S protease regulatory subunit 4	PSMC1	0.91005	0.79565	-0.135982283	-0.329794154
Ubiquilin-1;Ubiquilin-4;Ubiquilin-2	UBQLN1; UBQLN4; UBQLN2	0.91154	0.72892	-0.133622129	-0.456167609
Elongation factor 1-delta	EEF1D	0.91267	0.75024	-0.131834785	-0.414575911
Kinesin-1 heavy chain	KIF5B	0.91428	0.76582	-0.129292034	-0.384922757
Vasodilator-stimulated phosphoprotein	VASP	0.91711	0.8065	-0.124833311	-0.310253562
Stress-induced-phosphoprotein 1	STIP1	0.9173	0.80948	-0.124534455	-0.304932659
Ubiquitin-60S ribosomal protein L40;Ubiquitin;60S ribosomal protein L40;Ubiquitin-40S ribosomal protein S27a;Ubiquitin;40S ribosomal protein S27a;Polyubiquitin-B;Ubiquitin;Polyubiquitin-C;Ubiquitin	UBA52; UBB; RPS27A; UBC; UBBP4	0.91963	0.76885	-0.120874565	-0.379225934
Integrin alpha-6;Integrin alpha-6 heavy chain;Integrin alpha-6 light chain	ITGA6	0.9207	0.76481	-0.119196948	-0.386826708
CAD protein;Glutamine-dependent carbamoyl-phosphate synthase;Aspartate carbamoyltransferase;Dihydroorotase	CAD	0.92526	0.74221	-0.112069272	-0.430100656
Spliceosome RNA helicase DDX39B	DDX39B	0.92526	0.79005	-0.112069272	-0.339984135
Nuclear migration protein nudC	NUDC	0.92859	0.75741	-0.10688635	-0.400853626
Methionine--tRNA ligase, cytoplasmic	MARS	0.92866	0.74526	-0.1067776	-0.424184266
RuvB-like 1	RUVBL1	0.92871	0.74351	-0.106699925	-0.427575949
Tyrosine--tRNA ligase, cytoplasmic;Tyrosine--tRNA ligase, cytoplasmic, N-terminally processed	YARS	0.92918	0.78243	-0.105969993	-0.353966408
Heterogeneous nuclear ribonucleoprotein F;Heterogeneous nuclear ribonucleoprotein F, N-terminally processed	HNRNPF	0.9323	0.75975	-0.101133828	-0.396403325
Cleavage stimulation factor subunit 2;Cleavage stimulation factor subunit 2 tau variant	CSTF2;CSTF2T	0.93266	0.77924	-0.100576851	-0.359860359
UBX domain-containing protein 7	UBXN7	0.93404	0.78659	-0.098443761	-0.34631625
Eukaryotic translation initiation factor 5	EIF5	0.93502	0.77894	-0.09693087	-0.36041589
UBX domain-containing protein 4	UBXN4	0.93993	0.77773	-0.089374777	-0.362658705
Far upstream element-binding protein 1	FUBP1	0.94279	0.79583	-0.084991639	-0.32946781
Basic leucine zipper and W2 domain-containing protein 1	BZW1	0.94283	0.80343	-0.08493043	-0.315755762
Perilipin-2	PLIN2	0.94601	0.77039	-0.080072661	-0.376339118
Myristoylated alanine-rich C-kinase substrate	MARCKS	0.94888	0.80935	-0.075702446	-0.30516437
Insulin-like growth factor 2 mRNA-binding protein 3	IGF2BP3	0.9489	0.81919	-0.075672038	-0.287729991

Golgi-associated PDZ and coiled-coil motif-containing protein	GOPC	0.94988	0.83606	-0.074182828	-0.258321614
Signal recognition particle subunit SRP68	SRP68	0.95087	0.76092	-0.072679981	-0.394183312
Catenin alpha-1	CTNNA1	0.9524	0.82112	-0.070360474	-0.284335019
Structural maintenance of chromosomes protein 3	SMC3	0.95289	0.75162	-0.069618413	-0.411924639
Ubiquitin carboxyl-terminal hydrolase 10	USP10	0.95632	0.81237	-0.064434647	-0.299791132
Hypoxia up-regulated protein 1	HYOU1	0.95726	0.79176	-0.063017269	-0.336864911
RNA polymerase II-associated protein 3	RPAP3	0.95804	0.8262	-0.061842202	-0.275437035
Cytoplasmic dynein 1 light intermediate chain 2	DYNC1LI2	0.95828	0.79902	-0.061480836	-0.32369648
Poliovirus receptor-related protein 2	PVRL2	0.95902	0.80364	-0.060367192	-0.315378721
Heat shock cognate 71 kDa protein	HSPA8	0.95905	0.80196	-0.060322063	-0.318397815
Splicing factor 3A subunit 3	SF3A3	0.95908	0.76832	-0.060276935	-0.380220786
Large neutral amino acids transporter small subunit 1	SLC7A5	0.96134	0.77131	-0.056881331	-0.374617279
Cytoplasmic dynein 1 intermediate chain 2	DYNC1I2	0.96236	0.79512	-0.055351416	-0.330755486
RNA-binding protein 14	RBM14	0.9635	0.75642	-0.053643428	-0.402740586
Serine/threonine-protein phosphatase 2A 56 kDa regulatory subunit delta isoform	PPP2R5D	0.96767	0.83005	-0.047412959	-0.268729852
Y-box-binding protein 3	YBX3	0.96879	0.79093	-0.045744121	-0.338378078
Calnexin	CANX	0.96986	0.89394	-0.044151587	-0.161750092
Endoplasmin	HSP90B1	0.97051	0.81474	-0.043185017	-0.295588355
Hepatoma-derived growth factor	HDGF	0.9729	0.85812	-0.03963657	-0.220748686
Craniofacial development protein 1	CFDP1	0.97402	0.87136	-0.037976699	-0.198659207
Hsp90 co-chaperone Cdc37;Hsp90 co-chaperone Cdc37, N-terminally processed	CDC37	0.9761	0.81923	-0.034899138	-0.287659547
Proteasomal ubiquitin receptor ADRM1	ADRM1	0.9805	0.80083	-0.028410464	-0.320432075
Lupus La protein	SSB	0.98073	0.80709	-0.028072085	-0.309198535
Band 4.1-like protein 2	EPB41L2	0.98075	0.85801	-0.028042665	-0.220933633
Poliovirus receptor	PVR	0.98087	0.78136	-0.027866154	-0.355940693
Transcription intermediary factor 1-beta	TRIM28	0.98174	0.83532	-0.026587097	-0.259599114
Splicing factor 1	SF1	0.98242	0.82381	-0.025588164	-0.279616456
78 kDa glucose-regulated protein	HSPA5	0.98925	0.82719	-0.015592935	-0.27370935
Na(+)/H(+) exchange regulatory cofactor NHE-RF1	SLC9A3R1	0.98995	0.80188	-0.014572435	-0.318541739
Nucleosome assembly protein 1-like 4	NAP1L4;NAP1L4b	0.9954	0.85689	-0.006651708	-0.222818079
UBX domain-containing protein 1	UBXN1	0.9957	0.81404	-0.006216965	-0.296828408
Microtubule-associated protein 4;Microtubule-associated protein	MAP4	0.99754	0.91129	-0.003553402	-0.134017859
Mitochondrial import inner membrane translocase subunit TIM44	TIMM44	0.99804	0.82906	-0.002830457	-0.27045158
Endophilin-A2;Endophilin-A1	SH3GL1;SH3GL2	0.99911	0.81568	-0.00128457	-0.293924816
Long-chain-fatty-acid--CoA ligase 4	ACSL4	1.0002	0.8276	0.00028851	-0.27299445
Ezrin	EZR	1.0008	0.859	0.001153695	-0.219269964

Interleukin enhancer-binding factor 3	ILF3	1.0013	0.87047	0.001874286	-0.200133517
Heat shock 70 kDa protein 1A/1B	HSPA1A	1.0032	0.81746	0.004609253	-0.290779957
Proliferation-associated protein 2G4	PA2G4	1.0049	0.82965	0.007051943	-0.269425252
26S proteasome non-ATPase regulatory subunit 11	PSMD11	1.0101	0.81631	0.014498127	-0.292810964
Glycerol-3-phosphate dehydrogenase, mitochondrial	GPD2	1.0108	0.79723	0.015497569	-0.326932095
26S proteasome non-ATPase regulatory subunit 1	PSMD1	1.0128	0.83213	0.01834931	-0.265119163
Filamin-C	FLNC	1.014	0.83947	0.020057652	-0.252449326
cAMP-dependent protein kinase type I-alpha regulatory subunit;cAMP-dependent protein kinase type I-alpha regulatory subunit, N-terminally processed	PRKAR1A	1.0151	0.81016	0.021621858	-0.303721238
Thioredoxin domain-containing protein 5	TXNDC5	1.0209	0.82861	0.029841557	-0.271234863
Thyroid receptor-interacting protein 11	TRIP11	1.0211	0.88872	0.030124161	-0.17019914
Neutral alpha-glucosidase AB	GANAB	1.0246	0.88929	0.035060797	-0.169274132
		1.0247	0.82743	0.035201596	-0.273290829
DNA replication licensing factor MCM7	MCM7	1.0277	0.83349	0.039419183	-0.262763205
Bifunctional glutamate/proline--tRNA ligase;Glutamate--tRNA ligase;Proline--tRNA ligase	EPRS	1.03	0.90302	0.042644337	-0.147170154
Importin-5	IPO5	1.0303	0.83864	0.043064479	-0.253876452
Heat shock protein HSP 90-beta	HSP90AB1	1.0305	0.88007	0.043344505	-0.184309816
DNA damage-binding protein 1	DDB1	1.0306	0.84101	0.043484498	-0.24980514
26S protease regulatory subunit 7	PSMC2	1.0326	0.86927	0.046281503	-0.202123739
Histone acetyltransferase type B catalytic subunit	HAT1	1.0335	0.86213	0.047538389	-0.214022666
C-Jun-amino-terminal kinase-interacting protein 4	SPAG9	1.0434	0.86059	0.061292338	-0.216602019
Probable ATP-dependent RNA helicase DDX6	DDX6	1.0456	0.82639	0.064331046	-0.275105298
Signal recognition particle subunit SRP72	SRP72	1.0464	0.85215	0.065434446	-0.230820691
YTH domain family protein 3	YTHDF3	1.0493	0.91405	0.06942721	-0.12965501
Calcium-binding mitochondrial carrier protein Aralar2;Calcium-binding mitochondrial carrier protein Aralar1	SLC25A13; SLC25A12	1.0517	0.87147	0.072723231	-0.198477094
DNA replication licensing factor MCM3	MCM3	1.0554	0.87492	0.077789889	-0.192776988
Nuclear pore complex protein Nup85	NUP85	1.056	0.91959	0.078609835	-0.120937317
Very long-chain specific acyl-CoA dehydrogenase, mitochondrial	ACADVL	1.0565	0.90067	0.079292767	-0.150929487
Lysine--tRNA ligase	KARS	1.058	0.90832	0.081339627	-0.138727448
Calreticulin	CALR	1.0665	0.89201	0.092883966	-0.164868211
Importin subunit alpha-5	KPNA1	1.0667	0.89411	0.093154488	-0.161475762
Staphylococcal nuclease domain-containing protein 1	SND1	1.0724	0.86043	0.100843124	-0.216870268
Opioid growth factor receptor	OGFR	1.0725	0.84902	0.100977648	-0.236129556
UDP-glucose:glycoprotein glucosyltransferase 1	UGGT1	1.0747	0.9104	0.103933991	-0.135427537
Exportin-2	CSE1L	1.0758	0.92316	0.105409894	-0.115347381

Heterogeneous nuclear ribonucleoprotein H;Heterogeneous nuclear ribonucleoprotein H, N-terminally processed	HNRNPH1	1.0772	0.94249	0.107286135	-0.085450784
DNA replication licensing factor MCM2	MCM2	1.0787	0.87001	0.109293689	-0.200896111
Nucleosome assembly protein 1-like 1	NAP1L1	1.0789	0.90808	0.109561152	-0.139108693
Eukaryotic translation initiation factor 4 gamma 2	EIF4G2	1.0822	0.85472	0.113967146	-0.226476214
Importin subunit beta-1	KPNB1	1.0845	0.8917	0.117030053	-0.165369678
Major vault protein	MVP	1.0873	0.88575	0.120750053	-0.175028535
Valine--tRNA ligase	VARS	1.0907	0.90018	0.125254339	-0.151714583
Poly(rC)-binding protein 1	PCBP1	1.0922	0.86882	0.127237062	-0.202870781
Fatty acid synthase	FASN	1.0936	0.86988	0.129085148	-0.2011117
26S protease regulatory subunit 8	PSMC5	1.094	0.90948	0.129612738	-0.136886182
General transcription factor II-I	GTF2I	1.0997	0.86926	0.137110008	-0.202140336
Coatomer subunit alpha;Xenin;Proxenin	COPA	1.1025	0.88878	0.140778656	-0.170101742
DNA replication licensing factor MCM6	MCM6	1.1052	0.87667	0.144307467	-0.189894216
Heat shock protein 105 kDa;Heat shock 70 kDa protein 4L	HSPH1; HSPA4L	1.1059	0.90794	0.145220937	-0.139331133
Vinculin	VCL	1.1061	0.95202	0.145481822	-0.070936213
60 kDa SS-A/Ro ribonucleoprotein	TROVE2	1.1072	0.95514	0.146915848	-0.066215883
Septin-2	SEP2	1.1076	0.87434	0.147436959	-0.193733693
ERO1-like protein alpha	ERO1L	1.1105	0.87636	0.151209393	-0.190404458
ATP-dependent RNA helicase DDX19B;ATP-dependent RNA helicase DDX19A	DDX19A; DDX19B	1.1113	0.9631	0.152248331	-0.054242492
Stomatin-like protein 2, mitochondrial	STOML2	1.1134	0.87701	0.154971988	-0.189334802
Eukaryotic translation initiation factor 2 subunit 2	EIF2S2	1.1181	0.99487	0.161049225	-0.007420074
Coatomer subunit delta	ARCN1	1.1233	0.94161	0.16774328	-0.086798453
Putative pre-mRNA-splicing factor ATP-dependent RNA helicase DHX15	DHX15	1.1244	0.92659	0.169155359	-0.109996982
Protein ERGIC-53	LMAN1	1.126	1.0295	0.171206827	0.04194383
Melanoma-associated antigen 4	MAGEA4	1.1286	0.91999	0.174534255	-0.120309915
Vimentin	VIM	1.1288	0.93965	0.174789893	-0.089804612
AP-2 complex subunit beta;AP-1 complex subunit beta-1	AP2B1; AP1B1	1.1304	0.97207	0.176833371	-0.040867887
Peroxiredoxin-4	PRDX4	1.133	0.92426	0.180147861	-0.113629347
Eukaryotic translation initiation factor 4B	EIF4B	1.1407	0.97661	0.189919418	-0.034145544
Importin subunit alpha-3	KPNA4	1.1477	1.097	0.198745582	0.133563526
ATP-dependent DNA helicase Q1	RECQL	1.1531	1.0082	0.205517633	0.011781859
Cytochrome b-c1 complex subunit 2, mitochondrial	UQCRC2	1.1594	0.97615	0.213378391	-0.034825238
Nucleobindin-2;Nesfatin-1	NUCB2	1.166	0.98071	0.221567789	-0.028101506
LIM domain and actin-binding protein 1	LIMA1	1.1738	1.0164	0.231186613	0.023468281
T-complex protein 1 subunit theta	CCT8	1.176	0.97023	0.23388806	-0.043601306
Polyadenylate-binding protein 2	PABPN1	1.1765	0.928	0.234501321	-0.10780329

Echinoderm microtubule-associated protein-like 4	EML4	1.1782	0.99325	0.236584458	-0.009771207
Glucosidase 2 subunit beta	PRKCSH	1.18	0.98	0.23878686	-0.029146346
Protein disulfide-isomerase A6	PDIA6	1.1846	1.0414	0.244399991	0.058524312
Transcription elongation factor A protein 1	TCEA1	1.1854	0.93753	0.245373963	-0.093063239
Integrin beta-1	ITGB1	1.188	0.98332	0.248534836	-0.024267108
Apoptosis-inducing factor 1, mitochondrial	AIFM1	1.1951	0.97964	0.257131341	-0.029676413
Heterogeneous nuclear ribonucleoprotein M	HNRNPM	1.1951	1.0216	0.257131341	0.03083043
Adenylyl cyclase-associated protein 1	CAP1	1.1987	0.97009	0.261470639	-0.043809495
Eukaryotic initiation factor 4A-I	EIF4A1	1.1988	1.0011	0.261590989	0.001586092
Double-strand break repair protein MRE11A	MRE11A	1.2006	0.97855	0.263755573	-0.031282526
X-ray repair cross-complementing protein 6	XRCC6	1.2043	1.0038	0.268194823	0.005471851
Phenylalanine--tRNA ligase beta subunit	FARSB	1.2043	1.0076	0.268194823	0.010923027
ATP-dependent RNA helicase A	DHX9	1.2068	0.99858	0.271186602	-0.002050083
Phostensin	PPP1R18	1.2077	0.99448	0.272262125	-0.007985738
Moesin	MSN	1.2103	1.0552	0.275364696	0.07751647
Eukaryotic translation initiation factor 3 subunit B	EIF3B	1.2113	0.95698	0.276556218	-0.063439321
Glucose-6-phosphate 1-dehydrogenase	G6PD	1.2136	0.95923	0.279292991	-0.060051315
Glutamate dehydrogenase 1, mitochondrial;Glutamate dehydrogenase;Glutamate dehydrogenase 2, mitochondrial	GLUD1; GLUD2	1.2148	1.0899	0.280718814	0.124195772
Far upstream element-binding protein 2	KHSRP	1.2188	1.0104	0.285461405	0.014926544
Aspartate--tRNA ligase, cytoplasmic	DKFZp781B11202; DARS	1.219	0.97391	0.285698126	-0.038139637
39S ribosomal protein L37, mitochondrial	MRPL37	1.2201	0.97347	0.286999397	-0.038791576
Coronin;Coronin-1C	CORO1C	1.2225	1.1244	0.289834465	0.169155359
Tubulin beta chain	TUBB	1.2243	1.0376	0.291957116	0.053250385
Multifunctional protein ADE2	PAICS	1.2298	0.98137	0.298423712	-0.027130925
40S ribosomal protein SA	RPSA; RPSAP58	1.23	1.0303	0.298658316	0.043064479
Eukaryotic initiation factor 4A-III;Eukaryotic initiation factor 4A-III, N-terminally processed	EIF4A3	1.2302	0.9676	0.298892881	-0.047517326
Transitional endoplasmic reticulum ATPase	VCP	1.2324	1.0085	0.301470587	0.012211084
Serine/threonine-protein kinase OSR1	OXSR1	1.2338	1.0168	0.303108551	0.024035935
60S ribosomal protein L4	RPL4	1.234	1.0198	0.303342394	0.028286243
Procollagen galactosyltransferase 1;Procollagen galactosyltransferase 2	COLGALT1; COLGALT2	1.2373	1.0442	0.307195344	0.062398064
Polyadenylate-binding protein 1;Polyadenylate-binding protein 3	PABPC1; PABPC3	1.2379	1.0277	0.307894776	0.039419183
Nuclear pore complex protein Nup155	NUP155	1.2379	1.0261	0.307894776	0.037171338
Sodium-coupled neutral amino acid transporter 2	SLC38A2	1.242	1.0315	0.312665174	0.044743821

Protein disulfide-isomerase	P4HB	1.2432	1.0152	0.314058409	0.021763974
Filamin-A	FLNA	1.2444	1.0402	0.3154503	0.056860943
Heat shock protein HSP 90-alpha	HSP90AA1	1.245	1.0326	0.316145742	0.046281503
Serine/threonine-protein phosphatase 2A 65 kDa regulatory subunit A alpha isoform	PPP2R1A	1.2456	1.0611	0.31684085	0.085560625
26S proteasome non-ATPase regulatory subunit 12	PSMD12	1.2476	0.99423	0.319155458	-0.008348459
Clathrin heavy chain 1	CLTC	1.2493	0.98882	0.321119959	-0.016220171
Myosin-9;Myosin-14;Myosin-11	MYH9; MYH14; MYH11	1.2502	1.0682	0.322158908	0.095181789
Nuclear pore complex protein Nup214	NUP214	1.2645	1.0774	0.338567037	0.10755397
DNA replication licensing factor MCM5	MCM5	1.2652	0.9971	0.339365461	-0.004189894
NADPH--cytochrome P450 reductase	POR	1.2657	1.1368	0.339935493	0.18497846
2-oxoglutarate dehydrogenase, mitochondrial	OGDH	1.2669	1.0354	0.341302653	0.050188223
Protein disulfide-isomerase A4	PDIA4	1.2672	1.0333	0.341644241	0.047259175
Ephrin type-A receptor 2	EPHA2	1.2691	1.0622	0.343805752	0.087055435
Sec1 family domain-containing protein 1	SCFD1	1.2694	1.0607	0.344146748	0.085016673
TAR DNA-binding protein 43	TARDBP	1.2721	1.0744	0.347212086	0.10353121
Heterogeneous nuclear ribonucleoprotein D0	HNRNPD	1.2761	1.0518	0.351741389	0.072860402
Arginine--tRNA ligase, cytoplasmic	RARS	1.2779	1.0761	0.353774945	0.105812151
Sodium/potassium-transporting ATPase subunit alpha-1;Sodium/potassium-transporting ATPase subunit alpha-3;Sodium/potassium-transporting ATPase subunit alpha-2	ATP1A1;ATP1A3;ATP1A2	1.2784	1.0515	0.354339313	0.07244885
Tubulin beta-6 chain	TUBB6	1.279	1.0765	0.355016264	0.10634832
Alpha-centractin	ACTR1A	1.2795	1.0579	0.355580147	0.08120326
Protein SET	SET	1.28	1.0475	0.35614381	0.066950244
Dihydrolipoyllysine-residue acetyltransferase component of pyruvate dehydrogenase complex, mitochondrial	DLAT	1.2835	1.0345	0.360083296	0.048933645
Peptidyl-prolyl cis-trans isomerase FKBP4;Peptidyl-prolyl cis-trans isomerase FKBP4, N-terminally processed	FKBP4	1.2842	1.112	0.360869904	0.153156788
5-nucleotidase	NT5E	1.2843	1.0577	0.360982241	0.080930488
Elongation factor 2	EEF2	1.2863	1.0526	0.363227157	0.0739573
Vesicle-fusing ATPase	NSF	1.2873	1.0369	0.364348307	0.052276765
Inosine-5-monophosphate dehydrogenase 2	IMPDH2	1.2884	1.098	0.365580566	0.134878054
Putative elongation factor 1-alpha-like 3;Elongation factor 1-alpha 1;Elongation factor 1-alpha 2	EEF1A1P5; EEF1A1; EEF1A2	1.2884	1.0778	0.365580566	0.108089492
GMP synthase [glutamine-hydrolyzing]	GMPS	1.2964	1.068	0.374510926	0.094911647
CD44 antigen	CD44	1.2984	1.0776	0.376734905	0.107821756
Tubulin alpha-1C chain;Tubulin alpha-1B chain;Tubulin alpha-4A chain	TUBA1C; TUBA1B; TUBA4A	1.3019	1.1452	0.380618638	0.195599575

T-complex protein 1 subunit zeta	CCT6A	1.3022	1.0962	0.380951044	0.13251104
Nuclease-sensitive element-binding protein 1	YBX1	1.303	1.2078	0.381837084	0.272381578
60S ribosomal protein L3	RPL3	1.3072	1.0938	0.386479889	0.129348967
C-1-tetrahydrofolate synthase, cytoplasmic; N-terminally processed	MTHFD1	1.3126	1.1214	0.392427338	0.165300975
Delta-1-pyrroline-5-carboxylate synthase;Glutamate 5-kinase;Gamma-glutamyl phosphate reductase	ALDH18A1	1.3128	1.0344	0.392647144	0.04879418
Heterogeneous nuclear ribonucleoprotein L	HNRNPL	1.3139	1.1534	0.393855477	0.205892928
X-ray repair cross-complementing protein 5	XRCC5	1.3157	1.0887	0.39583057	0.122606463
Aspartyl/asparaginyl beta-hydroxylase	ASPH	1.3174	1.0864	0.397693455	0.119555385
Asparagine synthetase [glutamine-hydrolyzing]	ASNS	1.3229	1.0893	0.40370401	0.123401336
E3 ubiquitin/ISG15 ligase TRIM25	TRIM25	1.3232	1.0683	0.40403114	0.095316842
Fragile X mental retardation syndrome-related protein 1	FXR1	1.3313	1.0525	0.41283571	0.073820233
Nucleolar GTP-binding protein 1	GTPBP4	1.3343	1.1526	0.416083074	0.204891925
SWI/SNF-related matrix-associated actin-dependent regulator of chromatin subfamily E member 1	SMARCE1	1.3395	1.0747	0.421694581	0.103933991
Heat shock protein 75 kDa, mitochondrial	TRAP1	1.3413	1.1342	0.423631952	0.181675061
Eukaryotic peptide chain release factor subunit 1	ETF1	1.3439	1.0607	0.426425791	0.085016673
Ubiquitin-like modifier-activating enzyme 1	UBA1	1.3555	1.1176	0.438825113	0.160403926
Guanine nucleotide-binding protein G(s) subunit alpha isoforms short;Guanine nucleotide-binding protein G(s) subunit alpha isoforms XLas	GNAS	1.3601	1.1825	0.443712728	0.241840184
Spectrin beta chain, non-erythrocytic 1	SPTBN1	1.3621	1.0934	0.445832624	0.128821281
Protein disulfide-isomerase A3	PDIA3	1.3741	1.1493	0.458487	0.200755432
Annexin;Annexin A7	ANXA7	1.3797	1.0922	0.464354604	0.127237062
Sodium bicarbonate cotransporter 3	SLC4A7	1.381	1.1554	0.46571332	0.2083924
Cytochrome b-c1 complex subunit 1, mitochondrial	UQCRC1	1.3823	1.0915	0.467070757	0.12631213
Filamin-B	FLNB	1.3837	1.1562	0.468531186	0.209390977
Aspartate--tRNA ligase, mitochondrial	DARS2	1.3868	1.1062	0.471759742	0.145612247
Ribonuclease inhibitor	RNH1	1.3929	1.0965	0.478091687	0.132905812
Rab GDP dissociation inhibitor beta	GDI2	1.3936	1.1401	0.478816529	0.189160371
NADH-ubiquinone oxidoreductase 75 kDa subunit, mitochondrial	NDUFS1	1.3991	1.1314	0.484499082	0.178109076
Radixin	RDX	1.4028	1.2207	0.488309336	0.287708686
Adenosylhomocysteinase	AHCY	1.403	1.182	0.488515009	0.241230036
Caprin-1	CAPRIN1	1.41	1.186	0.495695163	0.24610401
Ras GTPase-activating protein-binding protein 1	G3BP1	1.4111	1.1607	0.496820231	0.214995135
4-trimethylaminobutyraldehyde dehydrogenase	ALDH9A1	1.4171	1.1901	0.502941568	0.251082803
Cytoskeleton-associated protein 5	CKAP5	1.4174	1.1268	0.503246954	0.172231469
4F2 cell-surface antigen heavy chain	SLC3A2	1.4205	1.1974	0.506398832	0.259905175
Eukaryotic translation initiation factor 4 gamma 1	EIF4G1	1.4226	1.2079	0.508530069	0.272501021

Reticulocalbin-1	RCN1	1.4259	1.2666	0.511872807	0.340960985
Nucleolin	NCL	1.4306	1.1982	0.516620347	0.260868739
DNA-dependent protein kinase catalytic subunit	PRKDC	1.4314	1.1364	0.517426885	0.184470737
Dihydrolipoyllysine-residue succinyltransferase component of 2-oxoglutarate dehydrogenase complex, mitochondrial	DLST	1.4324	1.2655	0.518434424	0.339707507
Nucleophosmin	NPM1	1.4328	1.1989	0.518837242	0.261711329
Spectrin alpha chain, non-erythrocytic 1	SPTAN1	1.4354	1.2124	0.521452826	0.277865757
ATP-dependent RNA helicase DDX39A	DDX39A;DDX39	1.4394	1.2114	0.525467563	0.276675317
Long-chain-fatty-acid--CoA ligase 3	ACSL3	1.4402	1.2188	0.526269172	0.285461405
T-complex protein 1 subunit delta	CCT4	1.4412	1.2174	0.527270557	0.283803271
Protein LAP2	ERBB2IP	1.4443	1.2868	0.53037044	0.363787841
T-complex protein 1 subunit eta	CCT7	1.452	1.2172	0.538041453	0.283566239
Heterogeneous nuclear ribonucleoproteins C1/C2	HNRNPC	1.4522	1.2353	0.538240158	0.304861451
Ubiquitin carboxyl-terminal hydrolase;Ubiquitin carboxyl-terminal hydrolase 14	USP14	1.4613	1.2444	0.547252389	0.3154503
Heat shock 70 kDa protein 4	HSPA4	1.4622	1.1757	0.548140657	0.233519979
Far upstream element-binding protein 3	FUBP3	1.4626	1.1894	0.548535267	0.250233981
U5 small nuclear ribonucleoprotein 200 kDa helicase	SNRNP200	1.464	1.253	0.549915554	0.325386415
Dynamin-like 120 kDa protein, mitochondrial;Dynamin-like 120 kDa protein, form S1	OPA1	1.4709	1.2394	0.556699167	0.309641873
Reticulon-4	RTN4	1.4736	1.2357	0.559344967	0.305328532
Transportin-1	TNPO1	1.4883	1.1851	0.573665363	0.2450088
6-phosphogluconate dehydrogenase, decarboxylating	PGD	1.4935	1.2415	0.578697238	0.312084262
	CAST	1.4987	1.1924	0.583711623	0.25386828
Glucose-6-phosphate isomerase	GPI	1.4999	1.2797	0.584866318	0.355805639
Ubiquitin carboxyl-terminal hydrolase 5	USP5	1.5152	1.2669	0.599508236	0.341302653
Lamina-associated polypeptide 2, isoform alpha;Thymopoietin;Thymopentin;Lamina-associated polypeptide 2, isoforms beta/gamma;Thymopoietin;Thymopentin	TMPO	1.5176	1.2381	0.601791584	0.308127844
Small nuclear ribonucleoprotein F	SNRPF	1.524	1.2556	0.607862903	0.328376934
Ribosome biogenesis regulatory protein homolog	RRS1	1.5413	1.3058	0.624147697	0.384933947
T-complex protein 1 subunit alpha	TCP1	1.5474	1.2675	0.629846179	0.341985747
Heterogeneous nuclear ribonucleoprotein U-like protein 1	HNRNPUL1	1.5687	1.2553	0.649569476	0.32803219
Myoferlin	MYOF	1.5754	1.3487	0.655718181	0.431569476
T-complex protein 1 subunit beta	CCT2	1.5802	1.2976	0.660107166	0.375845725
Protein phosphatase 1G	PPM1G	1.5808	1.3823	0.660654852	0.467070757
T-complex protein 1 subunit gamma	CCT3	1.5862	1.2532	0.665574688	0.325616675
Dolichyl-diphosphooligosaccharide--protein glycosyltransferase subunit 1	RPN1	1.5905	1.3408	0.669480372	0.423094054
Drebrin	DBN1	1.6013	1.3487	0.679243619	0.431569476

T-complex protein 1 subunit epsilon	CCT5	1.6024	1.3187	0.680234326	0.399116393
Lamin-B2	LMNB2	1.6071	1.264	0.684459702	0.337996464
28S ribosomal protein S27, mitochondrial	MRPS27	1.6139	1.3317	0.69055119	0.413269114
ATP synthase subunit beta, mitochondrial;ATP synthase subunit beta	ATP5B	1.6145	1.3648	0.691087441	0.448689552
Nucleolar RNA helicase 2	DDX21	1.62	1.3436	0.695993813	0.426103701
Glutaminase kidney isoform, mitochondrial	GLS	1.6242	1.3482	0.699729293	0.43103453
EH domain-containing protein 4	EHD4	1.6298	1.3638	0.704694936	0.44763209
Ubiquitin-associated protein 2-like	UBAP2L	1.633	1.4553	0.707524791	0.541316585
Neuroblast differentiation-associated protein AHNAK	AHNAK	1.6345	1.3761	0.708849377	0.460585313
Lamin-B1	LMNB1	1.6378	1.347	0.711759193	0.429749851
60 kDa heat shock protein, mitochondrial	HSPD1	1.647	1.3863	0.719840555	0.471239495
Fascin	FSCN1	1.6546	1.3481	0.726482487	0.430927517
Glycine--tRNA ligase	GARS	1.6578	1.4042	0.729269968	0.489748433
Prelamin-A/C;Lamin-A/C	LMNA	1.6627	1.4043	0.733527887	0.489851171
Protein RCC2	RCC2	1.6656	1.491	0.736041974	0.576280258
Alpha-enolase;Enolase	ENO1	1.6679	1.3881	0.738032794	0.473111505
Splicing factor 3A subunit 1	SF3A1	1.6722	1.3527	0.741747408	0.435841916
Polypyrimidine tract-binding protein 1	PTBP1	1.6782	1.4486	0.74691466	0.53465928
Alpha-actinin-1	ACTN1	1.6814	1.3509	0.749662978	0.433920884
Nodal modulator 2;Nodal modulator 1;Nodal modulator 3	NOMO2; NOMO1; NOMO3	1.682	1.436	0.750177706	0.522055749
Syntaxin-7	STX7	1.6827	1.3792	0.750777989	0.46383168
Phosphoglycerate kinase;Phosphoglycerate kinase 1	PGK1	1.7107	1.4439	0.774586781	0.529970829
Transketolase	TKT	1.7152	1.4325	0.778376811	0.518535139
Pyruvate kinase PKM;Pyruvate kinase	PKM	1.7242	1.4568	0.785927131	0.542802827
ATP synthase subunit alpha, mitochondrial;ATP synthase subunit alpha	ATP5A1	1.7352	1.4256	0.795101958	0.511569242
Pyruvate dehydrogenase E1 component subunit alpha, somatic form, mitochondrial	PDHA1	1.7396	1.4202	0.798755614	0.506094112
Pre-mRNA-processing-splicing factor 8	PRPF8	1.7579	1.3944	0.813853004	0.479644475
Neutral cholesterol ester hydrolase 1	NCEH1	1.7611	1.4034	0.816476832	0.488926268
Tubulin beta-3 chain	TUBB3	1.77	1.4843	0.82374936	0.569782712
Podocalyxin	PODXL	1.7787	1.5341	0.830823203	0.617392528
Actin, cytoplasmic 1;Actin, cytoplasmic 1, N-terminally processed;Actin, gamma-enteric smooth muscle;Actin, alpha skeletal muscle;Actin, alpha cardiac muscle 1;Actin, aortic smooth muscle	ACTB; ACTA1; ACTG2; ACTC1; ACTA2	1.7846	1.4753	0.835600745	0.561008354
Nuclear ubiquitous casein and cyclin-dependent kinase substrate 1	NUCKS1	1.7868	1.5902	0.83737816	0.669208225
Elongation factor Tu, mitochondrial	TUFM	1.793	1.4637	0.842375488	0.549619889

Histone-binding protein RBBP4	RBBP4	1.8011	1.6174	0.848878284	0.693676517
UDP-N-acetylhexosamine pyrophosphorylase;	UAP1	1.8074	1.4752	0.853915828	0.560910561
Heterogeneous nuclear ribonucleoprotein R	HNRNPR; HNRPR	1.8094	1.4825	0.855511377	0.568032105
Dolichyl-diphosphooligosaccharide--protein glycosyltransferase subunit 2	RPN2	1.8138	1.4764	0.859015385	0.562083643
ATP-dependent RNA helicase DDX3X;ATP-dependent RNA helicase DDX3Y	DDX3X; DDX3Y	1.817	1.4937	0.86155842	0.578890421
Heterogeneous nuclear ribonucleoprotein K	HNRNPK	1.8191	1.4938	0.863224853	0.578987003
Annexin;Annexin A11	ANXA11	1.8366	1.492	0.877037451	0.577247536
Transcription elongation factor SPT5	SUPT5H	1.838	1.488	0.878136767	0.573374526
Kinectin	KTN1	1.8736	1.6474	0.905812981	0.720190894
Probable ATP-dependent RNA helicase DDX17	DDX17	1.8906	1.583	0.91884416	0.662661255
Trifunctional enzyme subunit beta, mitochondrial;3-ketoacyl-CoA thiolase	HADHB	1.8913	1.5805	0.919378223	0.660381035
Dolichyl-diphosphooligosaccharide--protein glycosyltransferase subunit STT3A	STT3A	1.9077	1.6069	0.931834315	0.684280151
Ribosome-binding protein 1	RRBP1	1.9178	1.6735	0.939452275	0.742868551
Heterogeneous nuclear ribonucleoprotein U	HNRNPU	1.9246	1.7047	0.944558634	0.76951787
Actin, cytoplasmic 2;Actin, cytoplasmic 2, N-terminally processed	ACTG1	1.9271	1.5237	0.946431437	0.60757888
WD repeat-containing protein 1	WDR1	1.9283	1.5363	0.94732952	0.619459965
Serine--tRNA ligase, mitochondrial	SARS2	1.9485	1.5412	0.962363932	0.624054091
Sarcoplasmic/endoplasmic reticulum calcium ATPase 2	ATP2A2	1.9529	1.6479	0.965618077	0.720628698
Sulfide:quinone oxidoreductase, mitochondrial	SQRDL	1.9531	1.5932	0.965765818	0.671927385
Sodium-coupled neutral amino acid transporter 1	SLC38A1	1.9539	1.632	0.966356633	0.706641057
Trifunctional enzyme subunit alpha, mitochondrial;Long-chain enoyl-CoA hydratase;Long chain 3-hydroxyacyl-CoA dehydrogenase	HADHA	1.964	1.6245	0.97379493	0.699995744
Dihydrolipoyl dehydrogenase, mitochondrial;Dihydrolipoyl dehydrogenase	DLD	1.9821	1.6448	0.987029751	0.71791217
FAS-associated factor 2	FAF2	1.9903	1.7311	0.992985906	0.791689067
Stress-70 protein, mitochondrial	HSPA9	2.0124	1.7601	1.008917095	0.815657398
Alanine--tRNA ligase, cytoplasmic	AARS	2.0208	1.658	1.014926544	0.729444007
Nuclear mitotic apparatus protein 1	NUMA1	2.03	1.5971	1.021479727	0.675454648
Cleft lip and palate transmembrane protein 1	CLPTM1	2.0708	1.7433	1.050188223	0.80182086
Unconventional myosin-Ic	MYO1C	2.0794	1.6823	1.056167306	0.750435
DNA repair protein RAD50	RAD50	2.0832	1.7094	1.058801354	0.773490027
Tubulin beta-4B chain;Tubulin beta-4A chain	TUBB4B; TUBB4A	2.1249	1.7419	1.087394948	0.800661803
Non-POU domain-containing octamer-binding protein	NONO	2.1268	1.6762	1.088684372	0.745194298
Leucine-rich PPR motif-containing protein, mitochondrial	LRPPRC	2.1395	1.6865	1.097273679	0.754032318

Copine-3	CPNE3	2.1681	1.7656	1.1164313	0.820158535
Citrate synthase;Citrate synthase, mitochondrial	CS	2.1979	1.7358	1.136125748	0.795600729
Acetolactate synthase-like protein	ILVBL	2.2297	1.8114	1.156849613	0.857105163
Heterogeneous nuclear ribonucleoprotein Q	SYNCRIP	2.2344	2.0241	1.159887479	1.017280568
Extended synaptotagmin-1	ESYT1	2.2437	1.9242	1.165879789	0.94425876
Aspartate aminotransferase, mitochondrial;Aspartate aminotransferase	GOT2	2.2904	2.0754	1.195599575	1.05338942
Lon protease homolog, mitochondrial	LONP1	2.3464	1.9814	1.230448976	0.986520157
Fumarate hydratase, mitochondrial	FH	2.3542	2.0086	1.235236889	1.006190289
Acetyl-CoA acetyltransferase, mitochondrial	ACAT1	2.3599	1.8612	1.238725727	0.896233092
Golgin subfamily A member 2	GOLGA2	2.3884	1.9841	1.256044474	0.98848474
Ras GTPase-activating-like protein IQGAP1	IQGAP1	2.4033	1.8924	1.265016749	0.920217066
Matrin-3	MATR3	2.5962	2.3827	1.376401527	1.252597317
Probable ATP-dependent RNA helicase DDX5	DDX5	2.6149	2.394	1.386755775	1.259423152
Alpha-actinin-4	ACTN4	2.6452	2.2228	1.403376807	1.152378145
Neutral amino acid transporter B(0)	SLC1A5	2.9568	2.4615	1.564036662	1.29953774
Aconitate hydratase, mitochondrial	ACO2	3.0213	2.5356	1.595169444	1.342327173
ATP-dependent RNA helicase DDX42	DDX42	3.0794	2.4863	1.622649279	1.314000384
Plasminogen activator inhibitor 1 RNA-binding protein	SERBP1	6.2252	5.3169	2.638120188	2.410585333

Table 5: H1299 "Light" & H1299 Dyn1 KO "Heavy" SILAC Results

Protein names	Gene names	Ratio H/L	Ratio H/L normalized	log (Ratio H/L)	log (Ratio H/L normalized)
Lysine--tRNA ligase	KARS	0.47822	0.48149	-1.064253628	-1.05442226
Sequestosome-1	SQSTM1	0.49103	0.48586	-1.026116925	-1.041387432
Lamin-B1	LMNB1	0.52704	0.51109	-0.924015635	-0.968350731
Leucine-rich repeat flightless-interacting protein 1	LRRFIP1	0.56941	0.5588	-0.812460265	-0.839596074
Neutral cholesterol ester hydrolase 1	NCEH1	0.59513	0.58384	-0.74872325	-0.776355039
Prelamin-A/C;Lamin-A/C	LMNA	0.60581	0.60561	-0.723062702	-0.723539067
Extended synaptotagmin-1	ESYT1	0.61018	0.60155	-0.712693202	-0.733243438
Alpha-actinin-4	ACTN4	0.61893	0.63415	-0.692151843	-0.657103963
Na(+)/H(+) exchange regulatory cofactor NHE-RF1	SLC9A3R1	0.63035	0.60214	-0.665774992	-0.731829136
CD44 antigen	CD44	0.63381	0.62629	-0.657877673	-0.675097251
Reticulon-4	RTN4	0.63476	0.6636	-0.655716877	-0.591614209
Ubiquilin-1;Ubiquilin-4	UBQLN1; UBQLN4	0.638	0.63087	-0.648371671	-0.664585347
Ribosome-binding protein 1	RRBP1	0.64482	0.61672	-0.633031603	-0.697312462
Fumarate hydratase, mitochondrial	FH	0.66832	0.66342	-0.581389046	-0.592005589
Ras GTPase-activating protein-binding protein 1	G3BP1	0.67038	0.66774	-0.576948986	-0.58264163
Lamin-B2	LMNB2	0.67269	0.64328	-0.571986283	-0.63648126
C-1-tetrahydrofolate synthase, cytoplasmic; N-terminally processed	MTHFD1	0.67345	0.65881	-0.570357257	-0.602065641
Transcription elongation factor SPT5	SUPT5H	0.67833	0.63978	-0.559940796	-0.644352201
ATP synthase subunit beta;ATP synthase subunit beta, mitochondrial	ATP5B	0.68732	0.69125	-0.540946155	-0.53272052
General transcription factor II-I	GTF2I	0.68786	0.66889	-0.539813131	-0.580159118
Stress-70 protein, mitochondrial	HSPA9	0.68955	0.67909	-0.536272928	-0.558325307
Heterogeneous nuclear ribonucleoprotein K	HNRNPK	0.70254	0.695	-0.509347726	-0.524915117
Cleft lip and palate transmembrane protein 1	CLPTM1	0.70498	0.65586	-0.504345765	-0.608540205
Tubulin beta-4B chain;Tubulin beta-4A chain	TUBB4B; TUBB4A	0.70875	0.69286	-0.496651265	-0.529364226
Acetyl-CoA acetyltransferase, mitochondrial	ACAT1	0.71003	0.69964	-0.494048113	-0.515315321
Myristoylated alanine-rich C-kinase substrate	MARCKS	0.71049	0.70559	-0.493113751	-0.50309798
Splicing factor 1	SF1	0.71346	0.70559	-0.487095547	-0.50309798
Microtubule-associated protein;Microtubule-associated protein 4	MAP4	0.71581	0.7694	-0.482351396	-0.378194265
Far upstream element-binding protein 2	KHSRP	0.71817	0.69217	-0.477602706	-0.530801681
Vigilin	HDLBP	0.71822	0.7055	-0.477502267	-0.503282012

Vimentin	VIM	0.72239	0.7106	-0.469150173	-0.492890406
Peroxisomal multifunctional enzyme type 2;(3R)-hydroxyacyl-CoA dehydrogenase;Enoyl-CoA hydratase 2	HSD17B4	0.72459	0.71102	-0.464763199	-0.492037953
Tetratricopeptide repeat protein 1	TTC1	0.73269	0.72221	-0.448725169	-0.469509698
Transcription elongation factor A protein 1	TCEA1	0.73403	0.68108	-0.446089067	-0.554103827
Ubiquitin-associated protein 2-like	UBAP2L	0.73453	0.72886	-0.44510668	-0.456286368
DNA replication licensing factor MCM6	MCM6	0.73967	0.71797	-0.435046332	-0.478004532
Syntaxin-7	STX7	0.7404	0.74839	-0.4336232	-0.418137813
LETM1 and EF-hand domain-containing protein 1, mitochondrial	LETM1	0.74264	0.73567	-0.429265071	-0.442869334
Neuroblast differentiation-associated protein AHNAK	AHNAK	0.74473	0.73825	-0.42521062	-0.437818644
Host cell factor 1;HCF N-terminal chain 1;	HCFC1	0.74833	0.74206	-0.418253482	-0.430392253
Importin subunit alpha-1	KPNA2	0.74872	0.72001	-0.417501802	-0.473911151
Calnexin	CANX	0.75212	0.81912	-0.410965234	-0.287853275
Staphylococcal nuclease domain-containing protein 1	SND1	0.75751	0.73094	-0.400663161	-0.452175109
Sodium/potassium-transporting ATPase subunit alpha-1;Sodium/potassium-transporting ATPase subunit alpha-3;Sodium/potassium-transporting ATPase subunit alpha-2	ATP1A1; ATP1A3; ATP1A2	0.7577	0.74629	-0.400301347	-0.42219174
Nuclear pore complex protein Nup153	NUP153	0.7578	0.73332	-0.400110955	-0.447485208
Tubulin beta-3 chain	TUBB3	0.7686	0.75598	-0.379695118	-0.403580027
Probable ATP-dependent RNA helicase DDX17	DDX17	0.77195	0.74358	-0.373420689	-0.427440128
Trifunctional enzyme subunit alpha, mitochondrial;	HADHA	0.78012	0.77382	-0.358232035	-0.369930078
Dihydrolipoyllysine-residue acetyltransferase component of pyruvate dehydrogenase complex, mitochondrial	DLAT	0.78299	0.76832	-0.352934213	-0.380220786
Ephrin type-A receptor 2	EPHA2	0.78773	0.77396	-0.344226874	-0.369669088
ATP synthase subunit alpha, mitochondrial;ATP synthase subunit alpha	ATP5A1	0.79366	0.77802	-0.333406999	-0.362120853
Leucine-rich PPR motif-containing protein, mitochondrial	LRPPRC	0.80048	0.77973	-0.321062737	-0.358953452
Acetolactate synthase-like protein	ILVBL	0.80472	0.79229	-0.313441206	-0.335899502
Alkyldihydroxyacetonephosphate synthase, peroxisomal	AGPS	0.81333	0.79927	-0.298087266	-0.323245155
NADPH--cytochrome P450 reductase	POR	0.81705	0.80082	-0.291503727	-0.32045009
Heterogeneous nuclear ribonucleoproteins C1/C2	HNRNPC	0.83117	0.81217	-0.266784512	-0.300146357
Myoferlin	MYOF	0.83381	0.82733	-0.26220942	-0.273465198
Pyruvate dehydrogenase E1 component subunit alpha, somatic form, mitochondrial	PDHA1	0.83483	0.82083	-0.26044565	-0.284844635
Nucleoprotein TPR	TPR	0.84002	0.87498	-0.251504418	-0.192678054

Peptidyl-prolyl cis-trans isomerase FKBP4;Peptidyl-prolyl cis-trans isomerase FKBP4, N-terminally processed	FKBP4	0.84342	0.83646	-0.245676862	-0.257631543
Protein diaphanous homolog 1	DIAPH1	0.84554	0.82973	-0.242055089	-0.269286145
Glucosidase 2 subunit beta	PRKCSH	0.85529	0.83584	-0.225514423	-0.258701293
Transketolase	TKT	0.85632	0.84065	-0.223778074	-0.250422828
Dihydrolipoyllysine-residue succinyltransferase component of 2-oxoglutarate dehydrogenase complex, mitochondrial	DLST	0.86122	0.84373	-0.215546271	-0.245146695
T-complex protein 1 subunit beta	CCT2	0.86283	0.8505	-0.212851756	-0.233616859
Drebrin	DBN1	0.86638	0.85923	-0.206928156	-0.218883729
Polyadenylate-binding protein 1;Polyadenylate-binding protein 1-like 2;Polyadenylate-binding protein 1-like;Polyadenylate-binding protein 3;Polyadenylate-binding protein 4	PABPC1; PABPC4; PABPC1L2A; PABPC1L; PABPC3	0.86777	0.84686	-0.204615384	-0.239804607
Nucleosome assembly protein 1-like 4	NAP1L4; NAP1L4b	0.87869	0.86477	-0.18657382	-0.20961162
Sarcoplasmic/endoplasmic reticulum calcium ATPase 2;Sarcoplasmic/endoplasmic reticulum calcium ATPase 1	ATP2A2; ATP2A1	0.8833	0.86763	-0.179024583	-0.204848157
Neutral alpha-glucosidase AB	GANAB	0.88862	0.93375	-0.170361483	-0.098891757
Poly(rC)-binding protein 1	PCBP1	0.88969	0.87751	-0.168625358	-0.188512529
Apoptosis-inducing factor 1, mitochondrial	AIFM1	0.89364	0.87196	-0.162234332	-0.19766614
Pyruvate kinase PKM;Pyruvate kinase	PKM	0.89415	0.88924	-0.161411221	-0.169355249
DNA fragmentation factor subunit alpha	DFFA	0.89614	0.82571	-0.158203959	-0.276292917
Integrin beta-1	ITGB1	0.89669	0.88691	-0.157318786	-0.173140382
60 kDa heat shock protein, mitochondrial	HSPD1	0.89855	0.88559	-0.15432931	-0.175289163
Heat shock 70 kDa protein 4	HSPA4	0.90249	0.88402	-0.148017149	-0.177849085
Nuclear migration protein nudC	NUDC	0.90329	0.89616	-0.146738858	-0.158171761
Very long-chain specific acyl-CoA dehydrogenase, mitochondrial	ACADVL	0.91184	0.89884	-0.133147397	-0.153863766
Ubiquitin-60S ribosomal protein L40;Ubiquitin;60S ribosomal protein L40;Ubiquitin-40S ribosomal protein S27a;Ubiquitin;40S ribosomal protein S27a;Polyubiquitin-B;Ubiquitin;Polyubiquitin-C;Ubiquitin	UBA52; UBB; RPS27A; UBC; UBBP4	0.91581	0.88333	-0.126879777	-0.178975585
Eukaryotic translation initiation factor 4 gamma 1	EIF4G1	0.92023	0.90245	-0.119933605	-0.148081093
Heat shock protein 75 kDa, mitochondrial	TRAP1	0.9316	0.91909	-0.102217455	-0.121721954
Eukaryotic translation initiation factor 4B	EIF4B	0.93391	0.90702	-0.098644569	-0.140793732
Eukaryotic initiation factor 4A-I	EIF4A1	0.93546	0.91764	-0.096252129	-0.123999815
Fragile X mental retardation syndrome-related protein 1	FXR1	0.93866	0.92043	-0.091325413	-0.119620088
Stress-induced-phosphoprotein 1	STIP1	0.9404	0.94758	-0.088653556	-0.077680346
T-complex protein 1 subunit delta	CCT4	0.94713	0.91496	-0.078365636	-0.128219422

NSFL1 cofactor p47	NSFL1C	0.95316	0.93492	-0.069209686	-0.097085174
Phosphoglycerate kinase 1;Phosphoglycerate kinase	PGK1	0.95366	0.91281	-0.068453088	-0.131613498
Heterogeneous nuclear ribonucleoprotein H;Heterogeneous nuclear ribonucleoprotein H, N-terminally processed	HNRNPH1	0.95522	0.92514	-0.066095051	-0.112256392
Filamin-A	FLNA	0.96036	0.99506	-0.05835278	-0.007144575
Polypyrimidine tract-binding protein 1;Polypyrimidine tract-binding protein 3	PTBP1;PTBP3	0.9606	0.93395	-0.057992286	-0.098582779
Heterogeneous nuclear ribonucleoprotein A3	HNRNPA3	0.96285	0.91171	-0.054617033	-0.133353095
Tyrosine--tRNA ligase, cytoplasmic;Tyrosine--tRNA ligase, cytoplasmic, N-terminally processed	YARS	0.96357	0.94742	-0.053538618	-0.077923967
Septin-9	SEP9	0.96389	0.95657	-0.053059581	-0.064057549
T-complex protein 1 subunit zeta	CCT6A	0.96641	0.93577	-0.049292712	-0.095774117
T-complex protein 1 subunit alpha	TCP1	0.96674	0.94476	-0.048800159	-0.081980211
Protein disulfide-isomerase A3	PDIA3	0.97093	0.9367	-0.042560808	-0.09434103
Glutamate dehydrogenase;Glutamate dehydrogenase 1, mitochondrial	GLUD1	0.9766	0.96887	-0.034160317	-0.045624993
Perilipin-3	PLIN3	0.97831	0.99366	-0.031636406	-0.009175805
Putative elongation factor 1-alpha-like 3;Elongation factor 1-alpha 1;Elongation factor 1-alpha 2	EEF1A1P5;EEF1A1;EEF1A2	0.97865	0.98375	-0.031135102	-0.023636364
Cytoplasmic dynein 1 heavy chain 1	DYNC1H1	0.98063	0.96644	-0.028219197	-0.049247927
Vinculin	VCL	0.98363	0.97664	-0.023812358	-0.034101228
Perilipin-2	PLIN2	0.98445	0.97489	-0.022610161	-0.036688651
T-complex protein 1 subunit gamma	CCT3	0.98537	0.96356	-0.021262546	-0.05355359
Protein disulfide-isomerase A4	PDIA4	0.98701	0.97376	-0.018863393	-0.038361856
Eukaryotic translation initiation factor 4 gamma 2	EIF4G2	0.98966	0.9221	-0.014995126	-0.117004878
Hypoxia-inducible factor 1-alpha inhibitor	HIF1AN	0.98969	0.92295	-0.014951393	-0.115675602
Protein disulfide-isomerase	P4HB	0.99126	0.99036	-0.01266458	-0.013975049
Cytosol aminopeptidase	LAP3	0.99935	0.95558	-0.000938057	-0.065551436
Moesin	MSN	1.0069	0.99951	0.00992041	-0.000707094
Elongation factor Tu, mitochondrial	TUFM	1.0108	0.98708	0.015497569	-0.018761079
Calreticulin	CALR	1.0126	0.99925	0.018064389	-0.001082427
GTP-binding nuclear protein Ran	RAN	1.0198	1.012	0.028286243	0.01720929
Ubiquilin-2	UBQLN2	1.0199	1.0062	0.028427705	0.008917095
Mitochondrial import inner membrane translocase subunit TIM44	TIMM44	1.0201	1.0022	0.028710586	0.003170443
Polyadenylate-binding protein 2	PABPN1	1.0246	1.0056	0.035060797	0.008056555
Actin, cytoplasmic 2;Actin, cytoplasmic 2, N-terminally processed	ACTG1	1.0307	0.99835	0.043624477	-0.002382413
Vasodilator-stimulated phosphoprotein	VASP	1.0317	1.0156	0.045023522	0.0223323
Cytoplasmic dynein 1 intermediate chain 2	DYNC1I2	1.0362	0.991	0.051302489	-0.013043037

Transferrin receptor protein 1;Transferrin receptor protein 1, serum form	TFRC	1.0432	1.0203	0.061015775	0.028993412
Poly(rC)-binding protein 2	PCBP2	1.0452	1.0119	0.06377903	0.017066724
Dolichyl-diphosphooligosaccharide--protein glycosyltransferase subunit 1	RPN1	1.0468	1.0275	0.065985829	0.039138394
T-complex protein 1 subunit eta	CCT7	1.0489	1.0415	0.068877141	0.058662839
Protein disulfide-isomerase A6	PDIA6	1.0519	1.0147	0.07299756	0.021053252
Dynamin-like 120 kDa protein, mitochondrial;Dynamin-like 120 kDa protein, form S1	OPA1	1.052	1.044	0.073134705	0.062121712
Far upstream element-binding protein 1	FUBP1	1.0531	1.0365	0.074642438	0.051720116
UDP-glucose:glycoprotein glucosyltransferase 1	UGGT1	1.0551	1.0347	0.077379741	0.049212535
Hypoxia up-regulated protein 1	HYOU1	1.0592	1.0794	0.082975027	0.110229592
Heat shock 70 kDa protein 1A/1B	HSPA1A	1.0596	1.0306	0.083519749	0.043484498
Elongation factor 2	EEF2	1.0623	1.0381	0.08719125	0.053945425
DNA replication licensing factor MCM2	MCM2	1.0648	0.98197	0.090582476	-0.026249145
Heat shock cognate 71 kDa protein	HSPA8	1.0662	1.0743	0.092478087	0.103396924
DNA-dependent protein kinase catalytic subunit	PRKDC	1.0679	1.0574	0.094776557	0.080521232
Proliferation-associated protein 2G4	PA2G4	1.0687	1.0501	0.095856924	0.070526721
Y-box-binding protein 3	YBX3	1.0746	1.0617	0.103799743	0.086376168
Actin, cytoplasmic 1;Actin, cytoplasmic 1, N-terminally processed	ACTB	1.0759	1.0375	0.105543992	0.053111336
DNA replication licensing factor MCM3	MCM3	1.0775	1.0575	0.107687869	0.080657663
Alpha-enolase;Enolase	ENO1	1.0851	1.0605	0.117828004	0.084744621
40S ribosomal protein SA	RPSA;RPSAP58	1.091	1.1049	0.125651102	0.143915803
Nuclease-sensitive element-binding protein 1	YBX1	1.0915	1.124	0.12631213	0.168642036
ADP-ribosylation factor GTPase-activating protein 1	ARFGAP1	1.0921	1.0681	0.127104965	0.095046725
X-ray repair cross-complementing protein 5	XRCC5	1.0943	1.0848	0.130008304	0.117429084
CAD protein;	CAD	1.0947	1.0842	0.130535557	0.116630912
General vesicular transport factor p115	USO1	1.0957	1.0597	0.131852846	0.083655897
Transcription intermediary factor 1-beta	TRIM28	1.1047	1.1666	0.143654635	0.222309979
DNA replication licensing factor MCM5	MCM5	1.1069	1.086	0.146524891	0.119024103
Elongation factor 1-gamma	EEF1G	1.1112	1.0917	0.152118504	0.126576457
Fructose-bisphosphate aldolase A;Fructose-bisphosphate aldolase	ALDOA	1.1133	1.0943	0.154842407	0.130008304
Poliovirus receptor-related protein 2	PVRL2	1.1191	1.0954	0.162338958	0.131457785
Heterogeneous nuclear ribonucleoprotein L	HNRNPL	1.1198	1.093	0.163241085	0.128293401
Mitotic checkpoint protein BUB3	BUB3	1.1229	1.103	0.167229454	0.141432791
78 kDa glucose-regulated protein	HSPA5	1.1337	1.1371	0.181038924	0.185359135
Elongation factor 1-delta	EEF1D	1.1354	1.108	0.183200647	0.147957881

Sterol-4-alpha-carboxylate 3-dehydrogenase, decarboxylating	NSDHL	1.1357	1.1117	0.183581791	0.152767519
Mitochondrial import receptor subunit TOM70	TOMM70A	1.1379	1.1249	0.186373777	0.169796756
Arginine--tRNA ligase, cytoplasmic	RARS	1.139	1.0881	0.187767747	0.121811151
RuvB-like 2	RUVBL2	1.1408	1.0979	0.190045887	0.134746655
Plasminogen activator inhibitor 1	SERPINE1	1.1413	1.133	0.190678066	0.180147861
Inosine-5-monophosphate dehydrogenase 2	IMPDH2	1.1416	1.1217	0.19105724	0.165686877
Ezrin	EZR	1.1423	1.1337	0.191941593	0.181038924
RuvB-like 1	RUVBL1	1.144	1.1188	0.194087052	0.161952159
Peroxiredoxin-4	PRDX4	1.1454	1.1228	0.195851509	0.167100969
Transportin-1	TNPO1	1.1467	1.1126	0.197488002	0.153935011
Terminal uridylyltransferase 4	ZCCHC11	1.1511	1.1642	0.203013171	0.219338923
cAMP-dependent protein kinase type I-alpha regulatory subunit;cAMP-dependent protein kinase type I-alpha regulatory subunit, N-terminally processed	PRKAR1A	1.153	1.0971	0.205392513	0.133695033
Band 4.1-like protein 2	EPB41L2	1.1533	1.1292	0.20576784	0.175301034
Valine--tRNA ligase	VARS	1.1564	1.1154	0.209640514	0.157561176
T-complex protein 1 subunit theta	CCT8	1.1585	1.1352	0.212258044	0.182946495
Src substrate cortactin	CTTN	1.1655	1.1344	0.220949004	0.181929438
Importin subunit beta-1	KPNB1	1.1666	1.1313	0.222309979	0.177981556
Heterogeneous nuclear ribonucleoprotein F, N-terminally processed	HNRNPF	1.1674	1.1375	0.223298973	0.185866545
Splicing factor 3A subunit 3	SF3A3	1.1716	1.1322	0.228480098	0.179128829
Coatomer subunit gamma-2; Coatomer subunit gamma-1	COPG2;COPG1	1.1719	1.1488	0.228849468	0.200127654
Adenosylhomocysteinase	AHCY	1.1729	1.1388	0.230080016	0.187514398
Septin-11	SEP11	1.1764	1.2558	0.234378689	0.328606717
Endoplasmin	HSP90B1	1.1782	1.1494	0.236584458	0.200880954
Hepatoma-derived growth factor	HDGF	1.183	1.1262	0.242450074	0.171463056
Alpha-actinin-1	ACTN1	1.1837	1.1935	0.243303487	0.255198566
Lupus La protein	SSB	1.1917	1.1426	0.253021096	0.192320435
Reticulocalbin-1	RCN1	1.1944	1.2566	0.256286071	0.329525485
Talin-1	TLN1	1.195	1.1708	0.257010618	0.227494651
Stomatin-like protein 2, mitochondrial	STOML2	1.203	1.1672	0.266636643	0.223051788
Melanoma-associated antigen 4	MAGEA4	1.2102	1.1986	0.27524549	0.261350279
Heat shock protein HSP 90-alpha	HSP90AA1	1.2108	1.1847	0.27596058	0.244521774
Filamin-C	FLNC	1.2182	1.1815	0.28475101	0.240619629
Plasma membrane calcium-transporting ATPase 1;Plasma membrane calcium-transporting ATPase 3;Plasma membrane calcium-transporting ATPase 4;Plasma membrane calcium-transporting ATPase 2	ATP2B1;ATP2B2;ATP2B3;ATP2B4	1.221	1.1813	0.2880632	0.240375394

Nucleophosmin	NPM1	1.2249	1.203	0.292663973	0.266636643
26S proteasome non-ATPase regulatory subunit 12	PSMD12	1.2262	1.144	0.29419431	0.194087052
4F2 cell-surface antigen heavy chain	SLC3A2	1.227	1.2227	0.295135249	0.29007047
Hsp90 co-chaperone Cdc37;Hsp90 co-chaperone Cdc37, N-terminally processed	CDC37	1.2311	1.1968	0.299947954	0.25918208
Fatty acid synthase;	FASN	1.2318	1.1994	0.300768033	0.262312878
Proteasomal ubiquitin receptor ADRM1	ADRM1	1.2485	1.154	0.320195821	0.206643224
Heterogeneous nuclear ribonucleoprotein U	HNRNPU	1.251	1.2177	0.32308179	0.284158746
Insulin-like growth factor 2 mRNA-binding protein 2;Insulin-like growth factor 2 mRNA-binding protein 3	IGF2BP2;IGF2BP3	1.2546	1.2227	0.327227468	0.29007047
T-complex protein 1 subunit epsilon	CCT5	1.2636	1.2787	0.337539842	0.354677829
Protein FAM98B	FAM98B	1.2636	1.2009	0.337539842	0.264116022
ATP-dependent DNA helicase Q1	RECQL	1.2737	1.2527	0.349025513	0.325040955
Eukaryotic translation initiation factor 3 subunit B	EIF3B	1.2776	1.1982	0.353436218	0.260868739
X-ray repair cross-complementing protein 6	XRCC6	1.2841	1.2553	0.360757558	0.32803219
Ribosomal L1 domain-containing protein 1	RSL1D1	1.3032	1.2491	0.382058509	0.32088898
Tubulin alpha-1C chain;Tubulin alpha-1B chain;Tubulin alpha-1A chain;Tubulin alpha-3C/D chain;Tubulin alpha-4A chain;Tubulin alpha-3E chain	TUBA1C;TUBA1B;TUBA1A;TUBA3C;TUBA4A;TUBA3E	1.3065	1.2966	0.385707125	0.374733478
Putative eukaryotic translation initiation factor 2 subunit 3-like protein;Eukaryotic translation initiation factor 2 subunit 3	EIF2S3L;EIF2S3	1.316	1.2905	0.396159489	0.367930141
Insulin-like growth factor 2 mRNA-binding protein 1	IGF2BP1	1.3203	1.284	0.400865778	0.360645202
Bifunctional glutamate/proline--tRNA ligase;Glutamate--tRNA ligase;Proline--tRNA ligase	EPRS	1.3258	1.3075	0.406863158	0.386810946
Heat shock protein HSP 90-beta	HSP90AB1	1.3275	1.3204	0.408711861	0.400975044
Tubulin beta chain;Tubulin beta-2B chain;Tubulin beta-2A chain	TUBB;TUBB2B;TUBB2A	1.3277	1.2972	0.4089292	0.375400929
Coatomer subunit beta	COPB2	1.3287	1.2949	0.410015403	0.372840689
PRKC apoptosis WT1 regulator protein	PAWR	1.3298	1.2439	0.411209283	0.314870509
Eukaryotic initiation factor 4A-III;Eukaryotic initiation factor 4A-III, N-terminally processed	EIF4A3	1.3574	1.3269	0.440845918	0.408059648
26S protease regulatory subunit 7	PSMC2	1.3637	1.2895	0.447526301	0.366811773
Transitional endoplasmic reticulum ATPase	VCP	1.397	1.3617	0.482332021	0.445408894
Spectrin beta chain, non-erythrocytic 1	SPTBN1	1.3992	1.3463	0.484602194	0.428999926
Signal recognition particle subunit SRP72	SRP72	1.4093	1.3944	0.494978753	0.479644475
Heterogeneous nuclear ribonucleoprotein M	HNRNPM	1.42	1.3727	0.50589093	0.457016363
60S ribosomal protein L3	RPL3	1.4386	1.4279	0.524665509	0.513894947

Dolichyl-diphosphooligosaccharide--protein glycosyltransferase subunit 2	RPN2	1.4402	1.4706	0.526269172	0.55640489
Heterogeneous nuclear ribonucleoprotein U-like protein 1	HNRNPUL1	1.4459	1.4261	0.531967777	0.512075149
Tubulin beta-6 chain	TUBB6	1.4482	1.4361	0.534260856	0.522156212
Retrotransposon-derived protein PEG10	PEG10	1.4629	1.4224	0.548831154	0.508327229
26S proteasome non-ATPase regulatory subunit 2	PSMD2	1.4827	1.4698	0.568226722	0.555619857
Exportin-5	XPO5	1.5339	1.4843	0.617204432	0.569782712
60S ribosomal protein L4	RPL4	1.5454	1.5015	0.627980303	0.586404475
Clathrin heavy chain 1	CLTC	1.5804	1.5452	0.660289751	0.627793583
Cleavage stimulation factor subunit 3	CSTF3	1.6644	1.6422	0.735002193	0.715629841
Spliceosome RNA helicase DDX39B	DDX39B	1.6709	1.6457	0.740625394	0.718701366
Nucleolar RNA helicase 2	DDX21	1.6732	1.6301	0.742609903	0.704960471
Nucleolin	NCL	1.6918	1.6597	0.758559027	0.73092249
Putative ribosomal RNA methyltransferase NOP2	NOP2	1.7895	1.7692	0.839556544	0.823097147
Serpin H1	SERPINH1	1.889	1.8297	0.917622702	0.871607122
Melanoma-associated antigen D2	MAGED2	1.8995	1.8423	0.925619712	0.881508009
Myb-binding protein 1A	MYBBP1A	2.2655	2.2405	1.179829491	1.163820726

BIBLIOGRAPHY

1. Roth, T.F. and K.R. Porter, *Yolk Protein Uptake in the Oocyte of the Mosquito Aedes Aegypti. L.* J Cell Biol, 1964. **20**: p. 313-32.
2. Yamada, E., *The fine structure of the gall bladder epithelium of the mouse.* J Biophys Biochem Cytol, 1955. **1**(5): p. 445-58.
3. Moya, M., et al., *Inhibition of coated pit formation in Hep2 cells blocks the cytotoxicity of diphtheria toxin but not that of ricin toxin.* J Cell Biol, 1985. **101**(2): p. 548-59.
4. Hansen, S.H., K. Sandvig, and B. van Deurs, *The preendosomal compartment comprises distinct coated and noncoated endocytic vesicle populations.* J Cell Biol, 1991. **113**(4): p. 731-41.
5. Lamaze, C., et al., *Interleukin 2 receptors and detergent-resistant membrane domains define a clathrin-independent endocytic pathway.* Mol Cell, 2001. **7**(3): p. 661-71.
6. Kirkham, M., et al., *Ultrastructural identification of uncoated caveolin-independent early endocytic vehicles.* J Cell Biol, 2005. **168**(3): p. 465-76.
7. Scott, C.C., F. Vacca, and J. Gruenberg, *Endosome maturation, transport and functions.* Semin Cell Dev Biol, 2014. **31**: p. 2-10.
8. Preston, J.E., N. Joan Abbott, and D.J. Begley, *Transcytosis of macromolecules at the blood-brain barrier.* Adv Pharmacol, 2014. **71**: p. 147-63.
9. Antonescu, C.N., T.E. McGraw, and A. Klip, *Reciprocal regulation of endocytosis and metabolism.* Cold Spring Harb Perspect Biol, 2014. **6**(7): p. a016964.
10. Irannejad, R. and M. von Zastrow, *GPCR signaling along the endocytic pathway.* Curr Opin Cell Biol, 2014. **27**: p. 109-16.
11. Goh, L.K. and A. Sorkin, *Endocytosis of receptor tyrosine kinases.* Cold Spring Harb Perspect Biol, 2013. **5**(5): p. a017459.
12. Mellman, I. and Y. Yarden, *Endocytosis and cancer.* Cold Spring Harb Perspect Biol, 2013. **5**(12): p. a016949.
13. Carpentier, J.L., et al., *Co-localization of 125I-epidermal growth factor and ferritin-low density lipoprotein in coated pits: a quantitative electron microscopic study in normal and mutant human fibroblasts.* J Cell Biol, 1982. **95**(1): p. 73-7.
14. Neutra, M.R., et al., *Intracellular transport of transferrin- and asialoorosomucoid-colloidal gold conjugates to lysosomes after receptor-mediated endocytosis.* J Histochem Cytochem, 1985. **33**(11): p. 1134-44.
15. Robinson, M.S., *Forty Years of Clathrin-coated Vesicles.* Traffic, 2015.
16. Kirchhausen, T., D. Owen, and S.C. Harrison, *Molecular structure, function, and dynamics of clathrin-mediated membrane traffic.* Cold Spring Harb Perspect Biol, 2014. **6**(5): p. a016725.
17. Kirchhausen, T., *Adaptors for clathrin-mediated traffic.* Annu Rev Cell Dev Biol, 1999. **15**: p. 705-32.

18. McMahon, H.T. and E. Boucrot, *Molecular mechanism and physiological functions of clathrin-mediated endocytosis.* Nat Rev Mol Cell Biol, 2011. **12**(8): p. 517-33.
19. Honing, S., et al., *Phosphatidylinositol-(4,5)-bisphosphate regulates sorting signal recognition by the clathrin-associated adaptor complex AP2.* Mol Cell, 2005. **18**(5): p. 519-31.
20. Stimpson, H.E., et al., *Early-arriving Syp1p and Ede1p function in endocytic site placement and formation in budding yeast.* Mol Biol Cell, 2009. **20**(22): p. 4640-51.
21. Henne, W.M., et al., *FCHo proteins are nucleators of clathrin-mediated endocytosis.* Science, 2010. **328**(5983): p. 1281-4.
22. Reider, A., et al., *Syp1 is a conserved endocytic adaptor that contains domains involved in cargo selection and membrane tubulation.* EMBO J, 2009. **28**(20): p. 3103-16.
23. Cocucci, E., et al., *The first five seconds in the life of a clathrin-coated pit.* Cell, 2012. **150**(3): p. 495-507.
24. Woodward, M.P. and T.F. Roth, *Coated vesicles: characterization, selective dissociation, and reassembly.* Proc Natl Acad Sci U S A, 1978. **75**(9): p. 4394-8.
25. Qualmann, B., D. Koch, and M.M. Kessels, *Let's go bananas: revisiting the endocytic BAR code.* EMBO J, 2011. **30**(17): p. 3501-15.
26. Aguet, F., et al., *Advances in analysis of low signal-to-noise images link dynamin and AP2 to the functions of an endocytic checkpoint.* Dev Cell, 2013. **26**(3): p. 279-91.
27. Schmid, S.L. and V.A. Frolov, *Dynamin: functional design of a membrane fission catalyst.* Annu Rev Cell Dev Biol, 2011. **27**: p. 79-105.
28. Ferguson, S.M., et al., *Coordinated actions of actin and BAR proteins upstream of dynamin at endocytic clathrin-coated pits.* Dev Cell, 2009. **17**(6): p. 811-22.
29. Schlossman, D.M., et al., *An enzyme that removes clathrin coats: purification of an uncoating ATPase.* J Cell Biol, 1984. **99**(2): p. 723-33.
30. Ungewickell, E., et al., *Role of auxilin in uncoating clathrin-coated vesicles.* Nature, 1995. **378**(6557): p. 632-5.
31. Parton, R.G. and K. Simons, *The multiple faces of caveolae.* Nat Rev Mol Cell Biol, 2007. **8**(3): p. 185-94.
32. Pelkmans, L. and A. Helenius, *Endocytosis via caveolae.* Traffic, 2002. **3**(5): p. 311-20.
33. Murata, M., et al., *VIP21/caveolin is a cholesterol-binding protein.* Proc Natl Acad Sci U S A, 1995. **92**(22): p. 10339-43.
34. Harder, T. and K. Simons, *Caveolae, DIGs, and the dynamics of sphingolipid-cholesterol microdomains.* Curr Opin Cell Biol, 1997. **9**(4): p. 534-42.

35. Parton, R.G. and M.A. del Pozo, *Caveolae as plasma membrane sensors, protectors and organizers.* Nat Rev Mol Cell Biol, 2013. **14**(2): p. 98-112.
36. Nassar, Z.D. and M.O. Parat, *Cavin Family: New Players in the Biology of Caveolae.* Int Rev Cell Mol Biol, 2015. **320**: p. 235-305.
37. Kiss, A.L., *Caveolae and the regulation of endocytosis.* Adv Exp Med Biol, 2012. **729**: p. 14-28.
38. Li, S., R. Seitz, and M.P. Lisanti, *Phosphorylation of caveolin by src tyrosine kinases. The alpha-isoform of caveolin is selectively phosphorylated by v-Src in vivo.* J Biol Chem, 1996. **271**(7): p. 3863-8.
39. Kiss, A.L., et al., *Ocadaic acid treatment causes tyrosine phosphorylation of caveolin-2 and induces internalization of caveolae in rat peritoneal macrophages.* Micron, 2004. **35**(8): p. 707-15.
40. Henley, J.R., et al., *Dynamin-mediated internalization of caveolae.* J Cell Biol, 1998. **141**(1): p. 85-99.
41. Sandvig, K. and B. van Deurs, *Selective modulation of the endocytic uptake of ricin and fluid phase markers without alteration in transferrin endocytosis.* J Biol Chem, 1990. **265**(11): p. 6382-8.
42. Boucrot, E., et al., *Endophilin marks and controls a clathrin-independent endocytic pathway.* Nature, 2015. **517**(7535): p. 460-5.
43. Doherty, G.J. and H.T. McMahon, *Mechanisms of endocytosis.* Annu Rev Biochem, 2009. **78**: p. 857-902.
44. Conner, S.D. and S.L. Schmid, *Regulated portals of entry into the cell.* Nature, 2003. **422**(6927): p. 37-44.
45. Donaldson, J.G. and C.L. Jackson, *ARF family G proteins and their regulators: roles in membrane transport, development and disease.* Nat Rev Mol Cell Biol, 2011. **12**(6): p. 362-75.
46. Mayor, S.P., R. Donaldson, J. , *Clathrin-independent pathways of endocytosis*, in *Endocytosis*, A.S. S.L. Schmid, M. Zerial, Editor. In Press, Cold Spring Harb Perspect Biol.
47. Bitsikas, V., I.R. Correa, Jr., and B.J. Nichols, *Clathrin-independent pathways do not contribute significantly to endocytic flux.* Elife, 2014. **3**: p. e03970.
48. Elkin, S.R., et al., *A Systematic Analysis Reveals Heterogeneous Changes in the Endocytic Activities of Cancer Cells.* Cancer Res, 2015. **75**(21): p. 4640-50.
49. Radhakrishna, H. and J.G. Donaldson, *ADP-ribosylation factor 6 regulates a novel plasma membrane recycling pathway.* J Cell Biol, 1997. **139**(1): p. 49-61.
50. Glebov, O.O., N.A. Bright, and B.J. Nichols, *Flotillin-1 defines a clathrin-independent endocytic pathway in mammalian cells.* Nat Cell Biol, 2006. **8**(1): p. 46-54.

51. Frick, M., et al., *Coassembly of flotillins induces formation of membrane microdomains, membrane curvature, and vesicle budding.* Curr Biol, 2007. **17**(13): p. 1151-6.
52. Maldonado-Baez, L., C. Williamson, and J.G. Donaldson, *Clathrin-independent endocytosis: a cargo-centric view.* Exp Cell Res, 2013. **319**(18): p. 2759-69.
53. Mitsunari, T., et al., *Clathrin adaptor AP-2 is essential for early embryonal development.* Mol Cell Biol, 2005. **25**(21): p. 9318-23.
54. Royle, S.J., *The cellular functions of clathrin.* Cell Mol Life Sci, 2006. **63**(16): p. 1823-32.
55. Song, Y., et al., *Caveolin-1 knockdown is associated with the metastasis and proliferation of human lung cancer cell line NCI-H460.* Biomed Pharmacother, 2012. **66**(6): p. 439-47.
56. Zhan, P., et al., *Expression of caveolin-1 is correlated with disease stage and survival in lung adenocarcinomas.* Oncol Rep, 2012. **27**(4): p. 1072-8.
57. Sunaga, N., et al., *Different roles for caveolin-1 in the development of non-small cell lung cancer versus small cell lung cancer.* Cancer Res, 2004. **64**(12): p. 4277-85.
58. Le Roy, C. and J.L. Wrana, *Clathrin- and non-clathrin-mediated endocytic regulation of cell signalling.* Nat Rev Mol Cell Biol, 2005. **6**(2): p. 112-26.
59. Howes, M.T., et al., *Clathrin-independent carriers form a high capacity endocytic sorting system at the leading edge of migrating cells.* J Cell Biol, 2010. **190**(4): p. 675-91.
60. Mayor, S., R.G. Parton, and J.G. Donaldson, *Clathrin-independent pathways of endocytosis.* Cold Spring Harb Perspect Biol, 2014. **6**(6).
61. Cossart, P. and A. Helenius, *Endocytosis of viruses and bacteria.* Cold Spring Harb Perspect Biol, 2014. **6**(8).
62. Adjei, I.M., B. Sharma, and V. Labhasetwar, *Nanoparticles: cellular uptake and cytotoxicity.* Adv Exp Med Biol, 2014. **811**: p. 73-91.
63. Stenmark, H., *Rab GTPases as coordinators of vesicle traffic.* Nat Rev Mol Cell Biol, 2009. **10**(8): p. 513-25.
64. Seabra, M.C., E.H. Mules, and A.N. Hume, *Rab GTPases, intracellular traffic and disease.* Trends Mol Med, 2002. **8**(1): p. 23-30.
65. Cheng, K.W., et al., *Emerging role of RAB GTPases in cancer and human disease.* Cancer Res, 2005. **65**(7): p. 2516-9.
66. Hutagalung, A.H. and P.J. Novick, *Role of Rab GTPases in membrane traffic and cell physiology.* Physiol Rev, 2011. **91**(1): p. 119-49.
67. Sharma, S., A. Skowronek, and K.S. Erdmann, *The role of the Lowe syndrome protein OCRL in the endocytic pathway.* Biol Chem, 2015. **396**(12): p. 1293-300.
68. Di Paolo, G. and P. De Camilli, *Phosphoinositides in cell regulation and membrane dynamics.* Nature, 2006. **443**(7112): p. 651-7.

69. Bissig, C. and J. Gruenberg, *Lipid sorting and multivesicular endosome biogenesis.* Cold Spring Harb Perspect Biol, 2013. **5**(10): p. a016816.
70. Esposito, G., F. Ana Clara, and P. Verstreken, *Synaptic vesicle trafficking and Parkinson's disease.* Dev Neurobiol, 2012. **72**(1): p. 134-44.
71. Jiang, S., et al., *Trafficking regulation of proteins in Alzheimer's disease.* Mol Neurodegener, 2014. **9**: p. 6.
72. Goldenring, J.R., *A central role for vesicle trafficking in epithelial neoplasia: intracellular highways to carcinogenesis.* Nat Rev Cancer, 2013. **13**(11): p. 813-20.
73. Parachoniak, C.A., et al., *GGA3 functions as a switch to promote Met receptor recycling, essential for sustained ERK and cell migration.* Dev Cell, 2011. **20**(6): p. 751-63.
74. Mellman, I.Y., Y., *Endocytosis and Cancer*, in *Endocytosis*, A.S. S.L. Schmid, M. Zerial, Editor. In Press, Cold Spring Harb Perspect Biol.
75. Galvez, B.G., et al., *Caveolae are a novel pathway for membrane-type 1 matrix metalloproteinase traffic in human endothelial cells.* Mol Biol Cell, 2004. **15**(2): p. 678-87.
76. Sottile, J. and J. Chandler, *Fibronectin matrix turnover occurs through a caveolin-1-dependent process.* Mol Biol Cell, 2005. **16**(2): p. 757-68.
77. Shi, F. and J. Sottile, *Caveolin-1-dependent beta1 integrin endocytosis is a critical regulator of fibronectin turnover.* J Cell Sci, 2008. **121**(Pt 14): p. 2360-71.
78. Parat, M.O., B. Anand-Apte, and P.L. Fox, *Differential caveolin-1 polarization in endothelial cells during migration in two and three dimensions.* Mol Biol Cell, 2003. **14**(8): p. 3156-68.
79. Xu, B., et al., *The significance of dynamin 2 expression for prostate cancer progression, prognostication, and therapeutic targeting.* Cancer Med, 2014. **3**(1): p. 14-24.
80. Deborde, S., et al., *Clathrin is a key regulator of basolateral polarity.* Nature, 2008. **452**(7188): p. 719-23.
81. Wang, Y., et al., *Tyrosine phosphorylated Par3 regulates epithelial tight junction assembly promoted by EGFR signaling.* EMBO J, 2006. **25**(21): p. 5058-70.
82. Aranda, V., et al., *Par6-aPKC uncouples ErbB2 induced disruption of polarized epithelial organization from proliferation control.* Nat Cell Biol, 2006. **8**(11): p. 1235-45.
83. Thiery, J.P., et al., *Epithelial-mesenchymal transitions in development and disease.* Cell, 2009. **139**(5): p. 871-90.
84. Palacios, F., et al., *ARF6-GTP recruits Nm23-H1 to facilitate dynamin-mediated endocytosis during adherens junctions disassembly.* Nat Cell Biol, 2002. **4**(12): p. 929-36.

85. Morishige, M., et al., *GEP100 links epidermal growth factor receptor signalling to Arf6 activation to induce breast cancer invasion.* Nat Cell Biol, 2008. **10**(1): p. 85-92.
86. Fujita, Y., et al., *Hakai, a c-Cbl-like protein, ubiquitinates and induces endocytosis of the E-cadherin complex.* Nat Cell Biol, 2002. **4**(3): p. 222-31.
87. Menju, T., et al., *Engagement of overexpressed Her2 with GEP100 induces autonomous invasive activities and provides a biomarker for metastases of lung adenocarcinoma.* PLoS One, 2011. **6**(9): p. e25301.
88. Palacios, F., et al., *Lysosomal targeting of E-cadherin: a unique mechanism for the down-regulation of cell-cell adhesion during epithelial to mesenchymal transitions.* Mol Cell Biol, 2005. **25**(1): p. 389-402.
89. Gauthier, N.C., T.A. Masters, and M.P. Sheetz, *Mechanical feedback between membrane tension and dynamics.* Trends Cell Biol, 2012. **22**(10): p. 527-35.
90. Cosson, P., et al., *Low cytoplasmic pH inhibits endocytosis and transport from the trans-Golgi network to the cell surface.* J Cell Biol, 1989. **108**(2): p. 377-87.
91. Heuser, J.E. and R.G. Anderson, *Hypertonic media inhibit receptor-mediated endocytosis by blocking clathrin-coated pit formation.* J Cell Biol, 1989. **108**(2): p. 389-400.
92. Larkin, J.M., et al., *Depletion of intracellular potassium arrests coated pit formation and receptor-mediated endocytosis in fibroblasts.* Cell, 1983. **33**(1): p. 273-85.
93. Schlegel, R., et al., *Amantadine and dansylcadaverine inhibit vesicular stomatitis virus uptake and receptor-mediated endocytosis of alpha 2-macroglobulin.* Proc Natl Acad Sci U S A, 1982. **79**(7): p. 2291-5.
94. Wang, L.H., K.G. Rothberg, and R.G. Anderson, *Mis-assembly of clathrin lattices on endosomes reveals a regulatory switch for coated pit formation.* J Cell Biol, 1993. **123**(5): p. 1107-17.
95. Gibson, A.E., et al., *Phenylarsine oxide inhibition of endocytosis: effects on asialofetuin internalization.* Am J Physiol, 1989. **257**(2 Pt 1): p. C182-4.
96. Macia, E., et al., *Dynasore, a cell-permeable inhibitor of dynamin.* Dev Cell, 2006. **10**(6): p. 839-50.
97. Robertson, M.J., et al., *Synthesis of Dynole 34-2, Dynole 2-24 and Dyngo 4a for investigating dynamin GTPase.* Nat Protoc, 2014. **9**(4): p. 851-70.
98. von Kleist, L., et al., *Role of the clathrin terminal domain in regulating coated pit dynamics revealed by small molecule inhibition.* Cell, 2011. **146**(3): p. 471-84.
99. Park, R.J., et al., *Dynamin triple knockout cells reveal off target effects of commonly used dynamin inhibitors.* J Cell Sci, 2013. **126**(Pt 22): p. 5305-12.
100. Preta, G., J.G. Cronin, and I.M. Sheldon, *Dynasore - not just a dynamin inhibitor.* Cell Commun Signal, 2015. **13**: p. 24.

101. Dutta, D., et al., *Pitstop 2 is a potent inhibitor of clathrin-independent endocytosis.* PLoS One, 2012. **7**(9): p. e45799.
102. Lemmon, S.K. and L.M. Traub, *Getting in touch with the clathrin terminal domain.* Traffic, 2012. **13**(4): p. 511-9.
103. Jomon, K., et al., *A new antibiotic, ikarugamycin.* J Antibiot (Tokyo), 1972. **25**(5): p. 271-80.
104. Hasumi, K., et al., *Inhibition of the uptake of oxidized low-density lipoprotein in macrophage J774 by the antibiotic ikarugamycin.* Eur J Biochem, 1992. **205**(2): p. 841-6.
105. Luo, T., et al., *Human immunodeficiency virus type 1 Nef-induced CD4 cell surface downregulation is inhibited by ikarugamycin.* J Virol, 2001. **75**(5): p. 2488-92.
106. Moscatelli, A., et al., *Distinct endocytic pathways identified in tobacco pollen tubes using charged nanogold.* J Cell Sci, 2007. **120**(Pt 21): p. 3804-19.
107. Bandmann, V., et al., *Uptake of fluorescent nano beads into BY2-cells involves clathrin-dependent and clathrin-independent endocytosis.* FEBS Lett, 2012. **586**(20): p. 3626-32.
108. Schmid, S.L. and E. Smythe, *Stage-specific assays for coated pit formation and coated vesicle budding in vitro.* J Cell Biol, 1991. **114**(5): p. 869-80.
109. Mettlen, M., et al., *Cargo- and adaptor-specific mechanisms regulate clathrin-mediated endocytosis.* J Cell Biol, 2010. **188**(6): p. 919-33.
110. Traub, L.M. and J.S. Bonifacino, *Cargo recognition in clathrin-mediated endocytosis.* Cold Spring Harb Perspect Biol, 2013. **5**(11): p. a016790.
111. Motley, A., et al., *Clathrin-mediated endocytosis in AP-2-depleted cells.* J Cell Biol, 2003. **162**(5): p. 909-18.
112. Popescu, R., et al., *Ikarugamycin induces DNA damage, intracellular calcium increase, p38 MAP kinase activation and apoptosis in HL-60 human promyelocytic leukemia cells.* Mutat Res, 2011. **709-710**: p. 60-6.
113. Bacac, M. and I. Stamenkovic, *Metastatic cancer cell.* Annu Rev Pathol, 2008. **3**: p. 221-47.
114. Hanahan, D. and R.A. Weinberg, *Hallmarks of cancer: the next generation.* Cell, 2011. **144**(5): p. 646-74.
115. Lanzetti, L. and P.P. Di Fiore, *Endocytosis and cancer: an 'insider' network with dangerous liaisons.* Traffic, 2008. **9**(12): p. 2011-21.
116. Mosesson, Y., G.B. Mills, and Y. Yarden, *Derailed endocytosis: an emerging feature of cancer.* Nat Rev Cancer, 2008. **8**(11): p. 835-50.
117. Bar-Sagi, D. and J.R. Feramisco, *Induction of membrane ruffling and fluid-phase pinocytosis in quiescent fibroblasts by ras proteins.* Science, 1986. **233**(4768): p. 1061-8.

118. Muller, P.A., et al., *Mutant p53 enhances MET trafficking and signalling to drive cell scattering and invasion.* Oncogene, 2013. **32**(10): p. 1252-65.
119. Naslavsky, N., R. Weigert, and J.G. Donaldson, *Characterization of a nonclathrin endocytic pathway: membrane cargo and lipid requirements.* Mol Biol Cell, 2004. **15**(8): p. 3542-52.
120. Phelps, R.M., et al., *NCI-Navy Medical Oncology Branch cell line data base.* J Cell Biochem Suppl, 1996. **24**: p. 32-91.
121. Gazdar, A.F., et al., *Lung cancer cell lines as tools for biomedical discovery and research.* J Natl Cancer Inst, 2010. **102**(17): p. 1310-21.
122. Sato, M., et al., *Human lung epithelial cells progressed to malignancy through specific oncogenic manipulations.* Mol Cancer Res, 2013. **11**(6): p. 638-50.
123. Huang, F., et al., *Analysis of clathrin-mediated endocytosis of epidermal growth factor receptor by RNA interference.* J Biol Chem, 2004. **279**(16): p. 16657-61.
124. Arsic, N., et al., *A novel function for Cyclin A2: control of cell invasion via RhoA signaling.* J Cell Biol, 2012. **196**(1): p. 147-62.
125. Eisen, M.B., et al., *Cluster analysis and display of genome-wide expression patterns.* Proc Natl Acad Sci U S A, 1998. **95**(25): p. 14863-8.
126. Reich, M., et al., *GenePattern 2.0.* Nat Genet, 2006. **38**(5): p. 500-1.
127. Harding, C., J. Heuser, and P. Stahl, *Receptor-mediated endocytosis of transferrin and recycling of the transferrin receptor in rat reticulocytes.* J Cell Biol, 1983. **97**(2): p. 329-39.
128. Tiruppathi, C., et al., *Gp60 activation mediates albumin transcytosis in endothelial cells by tyrosine kinase-dependent pathway.* J Biol Chem, 1997. **272**(41): p. 25968-75.
129. Li, B., et al., *CD59 is overexpressed in human lung cancer and regulates apoptosis of human lung cancer cells.* Int J Oncol, 2013. **43**(3): p. 850-8.
130. Lakhan, S.E., S. Sabharanjak, and A. De, *Endocytosis of glycosylphosphatidylinositol-anchored proteins.* J Biomed Sci, 2009. **16**: p. 93.
131. Riento, K., et al., *Endocytosis of flotillin-1 and flotillin-2 is regulated by Fyn kinase.* J Cell Sci, 2009. **122**(Pt 7): p. 912-8.
132. Eyster, C.A., et al., *Discovery of new cargo proteins that enter cells through clathrin-independent endocytosis.* Traffic, 2009. **10**(5): p. 590-9.
133. Donatello, S., et al., *Lipid raft association restricts CD44-ezrin interaction and promotion of breast cancer cell migration.* Am J Pathol, 2012. **181**(6): p. 2172-87.
134. Ariza, A., et al., *Standard and variant CD44 isoforms are commonly expressed in lung cancer of the non-small cell type but not of the small cell type.* J Pathol, 1995. **177**(4): p. 363-8.
135. Leung, E.L., et al., *Non-small cell lung cancer cells expressing CD44 are enriched for stem cell-like properties.* PLoS One, 2010. **5**(11): p. e14062.

136. Luo, Z., et al., *Prognostic value of CD44 expression in non-small cell lung cancer: a systematic review.* Int J Clin Exp Pathol, 2014. **7**(7): p. 3632-46.
137. Trowbridge, I.S. and F. Lopez, *Monoclonal antibody to transferrin receptor blocks transferrin binding and inhibits human tumor cell growth in vitro.* Proc Natl Acad Sci U S A, 1982. **79**(4): p. 1175-9.
138. Weissman, A.M., et al., *Exposure of K562 cells to anti-receptor monoclonal antibody OKT9 results in rapid redistribution and enhanced degradation of the transferrin receptor.* J Cell Biol, 1986. **102**(3): p. 951-8.
139. Ramirez, R.D., et al., *Immortalization of human bronchial epithelial cells in the absence of viral oncoproteins.* Cancer Res, 2004. **64**(24): p. 9027-34.
140. Leroy, B., et al., *Analysis of TP53 mutation status in human cancer cell lines: a reassessment.* Hum Mutat, 2014. **35**(6): p. 756-65.
141. Forbes, S.A., et al., *COSMIC: exploring the world's knowledge of somatic mutations in human cancer.* Nucleic Acids Res, 2015. **43**(Database issue): p. D805-11.
142. Edlund, K., et al., *Data-driven unbiased curation of the TP53 tumor suppressor gene mutation database and validation by ultradeep sequencing of human tumors.* Proc Natl Acad Sci U S A, 2012. **109**(24): p. 9551-6.
143. Ramsay, A.G., et al., *HS1-associated protein X-1 regulates carcinoma cell migration and invasion via clathrin-mediated endocytosis of integrin alphavbeta6.* Cancer Res, 2007. **67**(11): p. 5275-84.
144. Shatz, M., et al., *Caveolin-1 mutants P132L and Y14F are dominant negative regulators of invasion, migration and aggregation in H1299 lung cancer cells.* Exp Cell Res, 2010. **316**(10): p. 1748-62.
145. Au, N.H., et al., *Evaluation of immunohistochemical markers in non-small cell lung cancer by unsupervised hierarchical clustering analysis: a tissue microarray study of 284 cases and 18 markers.* J Pathol, 2004. **204**(1): p. 101-9.
146. Bhattacharjee, A., et al., *Classification of human lung carcinomas by mRNA expression profiling reveals distinct adenocarcinoma subclasses.* Proc Natl Acad Sci U S A, 2001. **98**(24): p. 13790-5.
147. Virmani, A.K., et al., *Hierarchical clustering of lung cancer cell lines using DNA methylation markers.* Cancer Epidemiol Biomarkers Prev, 2002. **11**(3): p. 291-7.
148. Byers, L.A., et al., *An epithelial-mesenchymal transition gene signature predicts resistance to EGFR and PI3K inhibitors and identifies Axl as a therapeutic target for overcoming EGFR inhibitor resistance.* Clin Cancer Res, 2013. **19**(1): p. 279-90.
149. Zhao, P., et al., *CD44 promotes Kras-dependent lung adenocarcinoma.* Oncogene, 2013. **32**(43): p. 5186-90.
150. Floyd, S. and P. De Camilli, *Endocytosis proteins and cancer: a potential link?* Trends Cell Biol, 1998. **8**(8): p. 299-301.

151. Sabharanjak, S., et al., *GPI-anchored proteins are delivered to recycling endosomes via a distinct cdc42-regulated, clathrin-independent pinocytic pathway.* Dev Cell, 2002. **2**(4): p. 411-23.
152. Chaudhary, N., et al., *Endocytic crosstalk: cavins, caveolins, and caveolae regulate clathrin-independent endocytosis.* PLoS Biol, 2014. **12**(4): p. e1001832.
153. Rappoport, J.Z. and S.M. Simon, *Endocytic trafficking of activated EGFR is AP-2 dependent and occurs through preformed clathrin spots.* J Cell Sci, 2009. **122**(Pt 9): p. 1301-5.
154. Loerke, D., et al., *Cargo and dynamin regulate clathrin-coated pit maturation.* PLoS Biol, 2009. **7**(3): p. e57.
155. Sever, S., A.B. Muhlberg, and S.L. Schmid, *Impairment of dynamin's GAP domain stimulates receptor-mediated endocytosis.* Nature, 1999. **398**(6727): p. 481-6.
156. Ferguson, S.M., et al., *A selective activity-dependent requirement for dynamin 1 in synaptic vesicle endocytosis.* Science, 2007. **316**(5824): p. 570-4.
157. Raimondi, A., et al., *Overlapping role of dynamin isoforms in synaptic vesicle endocytosis.* Neuron, 2011. **70**(6): p. 1100-14.
158. Liu, Y.W., et al., *Differential curvature sensing and generating activities of dynamin isoforms provide opportunities for tissue-specific regulation.* Proc Natl Acad Sci U S A, 2011. **108**(26): p. E234-42.
159. Wu, C., et al., *BioGPS: an extensible and customizable portal for querying and organizing gene annotation resources.* Genome Biol, 2009. **10**(11): p. R130.
160. Reis, C.R., et al., *Crosstalk between Akt/GSK3beta signaling and dynamin-1 regulates clathrin-mediated endocytosis.* EMBO J, 2015. **34**(16): p. 2132-46.
161. Gyorffy, B., et al., *Online survival analysis software to assess the prognostic value of biomarkers using transcriptomic data in non-small-cell lung cancer.* PLoS One, 2013. **8**(12): p. e82241.
162. Vogel, C. and E.M. Marcotte, *Insights into the regulation of protein abundance from proteomic and transcriptomic analyses.* Nat Rev Genet, 2012. **13**(4): p. 227-32.
163. Reis, C.R., et al., *TRAIL-death receptor endocytosis and apoptosis are selectively regulated by dynamin-1 activation.* Proc Natl Acad Sci U S A, 2017.
164. Zoncu, R., et al., *A phosphoinositide switch controls the maturation and signaling properties of APPL endosomes.* Cell, 2009. **136**(6): p. 1110-21.
165. Schenck, A., et al., *The endosomal protein Appl1 mediates Akt substrate specificity and cell survival in vertebrate development.* Cell, 2008. **133**(3): p. 486-97.
166. Sigismund, S., et al., *Clathrin-mediated internalization is essential for sustained EGFR signaling but dispensable for degradation.* Dev Cell, 2008. **15**(2): p. 209-19.

167. Ishida, N., et al., *Dynamin 2 associates with microtubules at mitosis and regulates cell cycle progression.* Cell Struct Funct, 2011. **36**(2): p. 145-54.
168. Liu, Y.W., et al., *Isoform and splice-variant specific functions of dynamin-2 revealed by analysis of conditional knock-out cells.* Mol Biol Cell, 2008. **19**(12): p. 5347-59.
169. Hennig, J., et al., *APPL proteins modulate DNA repair and radiation survival of pancreatic carcinoma cells by regulating ATM.* Cell Death Dis, 2014. **5**: p. e1199.
170. Rai, S., et al., *Clathrin assembly protein CALM plays a critical role in KIT signaling by regulating its cellular transport from early to late endosomes in hematopoietic cells.* PLoS One, 2014. **9**(10): p. e109441.
171. Sakaguchi, K., Y. Okabayashi, and M. Kasuga, *Shc mediates ligand-induced internalization of epidermal growth factor receptors.* Biochem Biophys Res Commun, 2001. **282**(5): p. 1154-60.
172. Boulbes, D., et al., *Rictor phosphorylation on the Thr-1135 site does not require mammalian target of rapamycin complex 2.* Mol Cancer Res, 2010. **8**(6): p. 896-906.
173. Er, E.E., et al., *AKT facilitates EGFR trafficking and degradation by phosphorylating and activating PIKfyve.* Sci Signal, 2013. **6**(279): p. ra45.
174. Motti, M.L., et al., *Akt-dependent T198 phosphorylation of cyclin-dependent kinase inhibitor p27kip1 in breast cancer.* Cell Cycle, 2004. **3**(8): p. 1074-80.
175. Ahn, S., et al., *Src-mediated tyrosine phosphorylation of dynamin is required for beta2-adrenergic receptor internalization and mitogen-activated protein kinase signaling.* J Biol Chem, 1999. **274**(3): p. 1185-8.
176. Ceresa, B.P., et al., *Inhibition of clathrin-mediated endocytosis selectively attenuates specific insulin receptor signal transduction pathways.* Mol Cell Biol, 1998. **18**(7): p. 3862-70.
177. Paarmann, P., et al., *Dynamin-dependent endocytosis of Bone Morphogenetic Protein2 (BMP2) and its receptors is dispensable for the initiation of Smad signaling.* Int J Biochem Cell Biol, 2016. **76**: p. 51-63.
178. Powell, K.A., et al., *Phosphorylation of dynamin I on Ser-795 by protein kinase C blocks its association with phospholipids.* J Biol Chem, 2000. **275**(16): p. 11610-7.
179. Wang, P., et al., *Dynamin-related protein Drp1 is required for Bax translocation to mitochondria in response to irradiation-induced apoptosis.* Oncotarget, 2015. **6**(26): p. 22598-612.
180. Szklarczyk, D., et al., *STRING v10: protein-protein interaction networks, integrated over the tree of life.* Nucleic Acids Res, 2015. **43**(Database issue): p. D447-52.
181. Anderson, A.C., *Tim-3: an emerging target in the cancer immunotherapy landscape.* Cancer Immunol Res, 2014. **2**(5): p. 393-8.

182. Lim, D.S., et al., *ATM binds to beta-adaptin in cytoplasmic vesicles.* Proc Natl Acad Sci U S A, 1998. **95**(17): p. 10146-51.
183. Andrisse, S., et al., *ATM and GLUT1-S490 phosphorylation regulate GLUT1 mediated transport in skeletal muscle.* PLoS One, 2013. **8**(6): p. e66027.
184. Ames, H.M., et al., *Huntingtin-interacting protein 1: a Merkel cell carcinoma marker that interacts with c-Kit.* J Invest Dermatol, 2011. **131**(10): p. 2113-20.
185. Gommerman, J.L., R. Rottapel, and S.A. Berger, *Phosphatidylinositol 3-kinase and Ca2+ influx dependence for ligand-stimulated internalization of the c-Kit receptor.* J Biol Chem, 1997. **272**(48): p. 30519-25.
186. Baglietto, L., et al., *Risks of Lynch syndrome cancers for MSH6 mutation carriers.* J Natl Cancer Inst, 2010. **102**(3): p. 193-201.
187. Reinecke, J. and S. Caplan, *Endocytosis and the Src family of non-receptor tyrosine kinases.* Biomol Concepts, 2014. **5**(2): p. 143-55.
188. Schiappacassi, M., et al., *Role of T198 modification in the regulation of p27(Kip1) protein stability and function.* PLoS One, 2011. **6**(3): p. e17673.
189. van der Geer, P., et al., *The Shc adaptor protein is highly phosphorylated at conserved, twin tyrosine residues (Y239/240) that mediate protein-protein interactions.* Curr Biol, 1996. **6**(11): p. 1435-44.
190. Baron, V., F.O. Alengrin, and E. Van Obberghen, *Dynamin Associates with Src-Homology Collagen (SHC) and Becomes Tyrosine Phosphorylated in Response to Insulin.* Endocrinology, 1998. **139**(6): p. 3034-3037.
191. Carver, K.C., T.M. Piazza, and L.A. Schuler, *Prolactin enhances insulin-like growth factor I receptor phosphorylation by decreasing its association with the tyrosine phosphatase SHP-2 in MCF-7 breast cancer cells.* J Biol Chem, 2010. **285**(11): p. 8003-12.
192. Christian, F., E.L. Smith, and R.J. Carmody, *The Regulation of NF-kappaB Subunits by Phosphorylation.* Cells, 2016. **5**(1).
193. Wu, P., et al., *Differential regulation of transcription factors by location-specific EGF receptor signaling via a spatio-temporal interplay of ERK activation.* PLoS One, 2012. **7**(9): p. e41354.
194. Anjum, R. and J. Blenis, *The RSK family of kinases: emerging roles in cellular signalling.* Nat Rev Mol Cell Biol, 2008. **9**(10): p. 747-58.
195. Miwa, M. and M. Masutani, *PolyADP-ribosylation and cancer.* Cancer Sci, 2007. **98**(10): p. 1528-35.
196. Marechal, A. and L. Zou, *RPA-coated single-stranded DNA as a platform for post-translational modifications in the DNA damage response.* Cell Res, 2015. **25**(1): p. 9-23.
197. Chen, P.H., et al., *Crosstalk between CLCb/Dyn1-Mediated Adaptive Clathrin-Mediated Endocytosis and Epidermal Growth Factor Receptor Signaling Increases Metastasis.* Dev Cell, 2017. **40**(3): p. 278-288 e5.

198. Sorkin, A. and M. von Zastrow, *Endocytosis and signalling: intertwining molecular networks.* Nat Rev Mol Cell Biol, 2009. **10**(9): p. 609-22.
199. Di Fiore, P.P. and M. von Zastrow, *Endocytosis, signaling, and beyond.* Cold Spring Harb Perspect Biol, 2014. **6**(8).
200. Ran, F.A., et al., *Double nicking by RNA-guided CRISPR Cas9 for enhanced genome editing specificity.* Cell, 2013. **154**(6): p. 1380-9.
201. Lee, Y.C., et al., *Lectin-Magnetic Beads for Plasma Membrane Isolation.* Cold Spring Harb Protoc, 2015. **2015**(7): p. 674-8.
202. Trudgian, D.C. and H. Mirzaei, *Cloud CPFP: a shotgun proteomics data analysis pipeline using cloud and high performance computing.* J Proteome Res, 2012. **11**(12): p. 6282-90.
203. Trudgian, D.C., et al., *CPFP: a central proteomics facilities pipeline.* Bioinformatics, 2010. **26**(8): p. 1131-2.
204. Craig, R. and R.C. Beavis, *TANDEM: matching proteins with tandem mass spectra.* Bioinformatics, 2004. **20**(9): p. 1466-7.
205. Geer, L.Y., et al., *Open mass spectrometry search algorithm.* J Proteome Res, 2004. **3**(5): p. 958-64.
206. Elias, J.E. and S.P. Gygi, *Target-decoy search strategy for increased confidence in large-scale protein identifications by mass spectrometry.* Nat Methods, 2007. **4**(3): p. 207-14.